A PORTABLE COMPTON GAMMA-RAY CAMERA DESIGN

THESIS

Brian L. Evans, Captain, USAF

AFIT/GAP/ENP/95D-05

DEPARTMENT OF THE AIR FORCE
AIR UNIVERSITY
AIR FORCE INSTITUTE OF TECHNOLOGY

Wright-Patterson Air Force Base, Ohio

A PORTABLE COMPTON GAMMA-RAY CAMERA DESIGN

THESIS

Brian L. Evans, Captain, USAF

AFIT/GAP/ENP/95D-05

AFIT/GAP/ENP/95D-05

DISCLAIMER STATEMENT

The views expressed in this thesis are those of the author and do not reflect the official policy or position of the Department of Defense or the U.S. Government.

AFIT/GAP/ENP/95D-05

A PORTABLE COMPTON GAMMA-RAY CAMERA DESIGN

THESIS

Presented to the Faculty of the School of Engineering

of the Air Force Institute of Technology

Air University

In Partial Fulfillment of the Requirements for the Degree of

Master of Science in Nuclear Engineering

Brian L. Evans, B.S.

Captain, USAF

November 1995

AFIT/GAP/ENP/95D-05

A PORTABLE COMPTON GAMMA-RAY CAMERA DESIGN

Brian L. Evans, B.S.

Captain, USAF

Approved: Date:

Jeffrey B. Martin — 27 Nov 95

Dr. Jeffrey B. Martin
Chairman, Advisory Committee

George John — 27 Nov 95

Dr. George John
Member, Advisory Committee

Larry W. Burggraf — 27 Nov 1995

Dr. Larry W. Burggraf
Member, Advisory Committee

Acknowledgments

I am grateful to my thesis advisor Dr. Jeffrey Martin for his outstanding help and guidance in this project. I am also grateful to the members of my advisory committee, Dr. George John and Dr. Larry Burggraf for their additional input and advice. Dr. Timothy DeVol of Clemson University provided help with the optical modeling program DETECT. Mr. Leroy Cannon, AFIT's nuclear lab technician, also provided valuable support on many occasions.

Table of Contents

List Of Figures

List Of Tables

Abstract

The purpose of this research is to investigate the angular resolution, efficiency, and energy resolution possible from a portable Compton camera gamma-ray imaging system for possible use in the field of nuclear nonproliferation. The proposed device uses room-temperature semiconductor and position-sensitive scintillation detectors. The position and energy resolution (and their energy dependence) of a room-temperature lithium-drifted silicon (Si(Li)) detector and a position-sensitive thallium-doped sodium iodide (NaI(Tl)) scintillation detector are investigated. The position and energy resolution of the position-sensitive scintillation detector is also modeled computationally, and the results compared to measured data. An efficiency model is also presented. The angular resolution, efficiency, and energy resolution of the proposed system are calculated. The same computational methods are then applied to a hypothetical position-sensitive thallium-doped cesium iodide (CsI(Tl)) scintillator. Based on the results, the angular resolution and energy resolution of a system employing this type of position-sensitive detector coupled to the same room-temperature Si(Li) detector is predicted.

A PORTABLE COMPTON GAMMA-RAY CAMERA DESIGN

I. Introduction

Motivation

Recent emphasis on the counterproliferation of nuclear weapons has resulted in a need for a portable radiation detection system with both spectroscopic and imaging capabilities. Such a system would permit both identification of radioisotope species as well as their location and spatial distribution. The radiation most likely to be useful in the counterproliferation mission are medium-energy gamma rays arising from the isotopes of interest due to their ability to penetrate a large thickness of material. Furthermore, gamma-ray energies are unique to each isotope enabling their use in isotope identification. A means of identifying isotopes in the environment is important in classifying the nature of nuclear activities at a certain site and distinguishing them from naturally occurring radioactivity. For counterproliferation activities where the location and identity of radioisotopes is unknown, a gamma-ray imaging camera with spectroscopy capabilities would be a useful tool. Portability is also an important characteristic, since the needs of the counterproliferation mission demand a device which can be deployed in the field and conveniently transported to different locations.

Gamma-ray imaging has been used in nuclear medicine and gamma-ray astronomy for years. Many of these devices rely on the collimation of incident radiation to form an image. Direct conversion of medical-imaging devices to a counterproliferation imaging device is not possible due to the lower energy gamma rays used in this discipline, and the lack of device portability. Furthermore, these devices do not exhibit adequate resolution for the more demanding spectroscopy requirements needed in counterproliferation. Gamma-ray sources of interest in counterproliferation are more spatially extended than those of gamma-ray astronomy. As a result, there is a special need for a portable medium energy (.15 to 3.0 MeV) gamma-ray imaging system for the counterproliferation mission. Such a system demands a position-sensitive gamma-ray detector with good energy and position resolution for medium energy gamma rays.

Background

A device which shows promise as a portable gamma-ray imaging system is the Compton camera. Several operating Compton cameras have been built and demonstrated [Martin 1994][McKisson 1994]. Their adequate position and energy resolution and lack of collimation may be well-suited for a portable gamma-ray imaging system. The Compton camera relies on the physics of Compton scattering to determine both the direction and energy of incident radiation, thereby obtaining the information needed to form an image.

Compton Scatter Cameras. High energy x-rays and gamma rays defy traditional methods of photon imaging like lenses and other optics because they have very short wavelengths and as a result cannot be refracted. Traditional techniques to form images with gamma rays employ mechanical absorbers like lead to collimate the photons striking an imaging detector. The collimators take many forms, but their general purpose is to reduce the radiation incident on a detector to a narrow range of incident angles. The act of collimating greatly reduces the efficiency of gamma-ray cameras employing them. The heavy lead collimators also add significant mass to the system, thereby reducing portability.

A more elegant alternative method to mechanically collimated imaging is the Compton scatter camera. One possible configuration of the Compton scatter camera consists of two position-sensitive detectors. When an incident gamma ray is Compton scattered from the first position sensitive detector to the second position sensitive detector, and if the scattered photon deposits its full energy in the second detector, the direction of the incident gamma ray can be localized to the surface of a cone. An image can be compiled by the accumulation of many interaction cones. The direction of the scattered gamma ray projected back through the scattering point forms the axis of this "interaction cone". Figure 1-1 illustrates a photon incident on the first detector which scatters into the second detector and the resulting interaction cone.

Spectroscopy can be performed with the Compton camera by summing the energies deposited in both detectors. Spectroscopy is important in the counterproliferation role because identifying the isotopes present at a site helps identify the nature of the activity there.

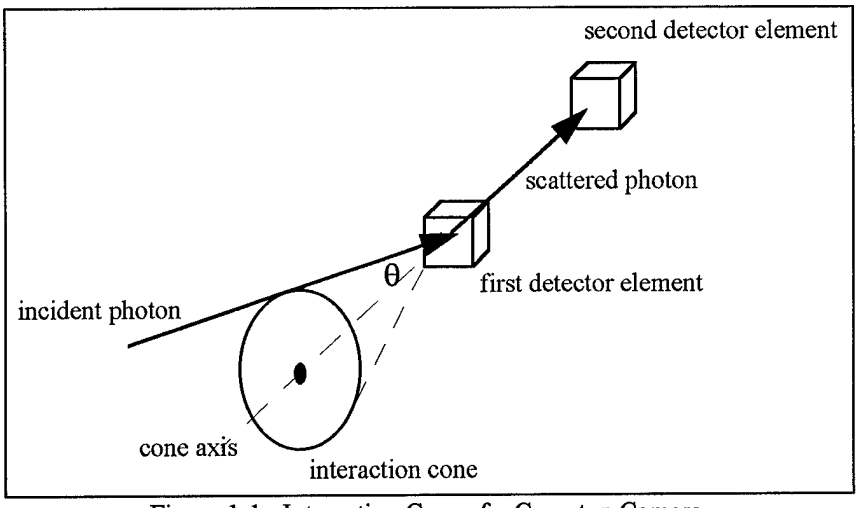

Figure 1-1. Interaction Cone of a Compton Camera.

When the incident gamma-ray energy E_γ is known (E_γ can also be determined from the sum of the energies deposited in both detectors), the cone angle θ is found from the Compton relation and the electron recoil energy (E_{re}), deposited in the first detector [Knoll 1989]

$$\cos(\theta) = 1 - \left[\frac{E_{re}}{\alpha(E_\gamma - E_{re})} \right] \qquad \alpha = \frac{E_\gamma}{m_o \cdot c^2} \qquad \text{(Equation 1-1)}$$

where m_0 is the rest mass energy of the electron and c is the speed of light.

If the incident gamma-ray energy is known, the angular resolution of the Compton camera described above depends on the energy resolution in one detector, the uncertainty in the position where the scatter occurred in the first detector, and the uncertainty in the position where the scattered photon was deposited in the second detector. If the incident gamma-ray energy is unknown, then the energy resolution in both detectors is a factor. The uncertainty in the scattering angle θ is a function of the uncertainty in the energy deposited in the first detector or both detectors. The uncertainty in the cone axis is a function of the uncertainty in the interaction site locations [McKisson 1994]. Thus the total angular resolution of the camera can be separated into two individual components: an energy component related

to the energy resolution, and a geometric component determined by the position resolution [Martin 1994:20].

$$\tan^2(\Delta\theta_{energy}) + \tan^2(\Delta\theta_{geometric}) = \tan^2(\Delta\theta_{total}) \qquad \text{(Equation 1-2)}$$

A ring Compton camera is a particular Compton camera configuration which employs a circular ring of detectors as the second detector. The first detector, located on the central axis of the ring, scatters the incident radiation to detectors positioned on the ring. Figure 1-2 illustrates a ring Compton camera in which a single first detector scatters incident gamma rays into a second detector consisting of four discrete detector elements positioned around the ring.

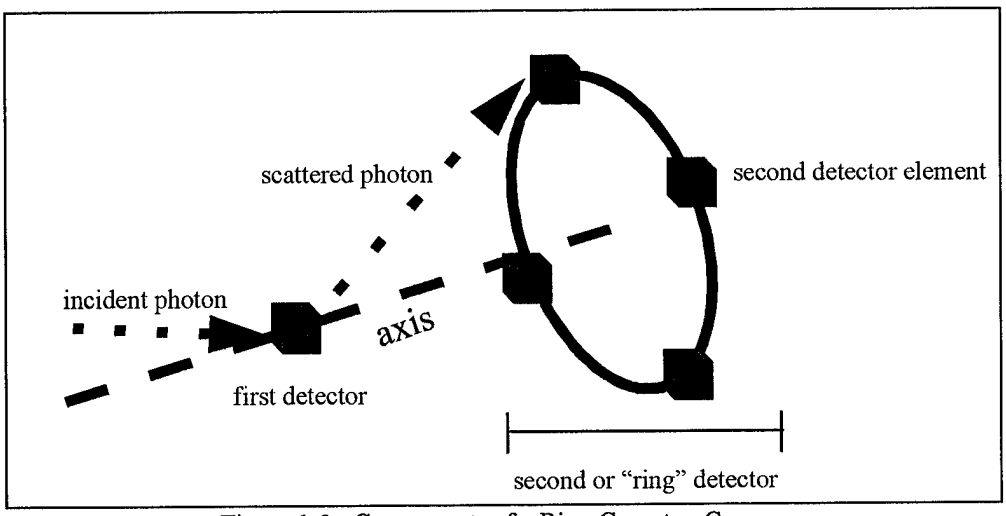

Figure 1-2. Components of a Ring Compton Camera

Successful imaging has been demonstrated with a ring Compton camera which uses a high-purity germanium (HPGe) detector as a first detector element and multiple sodium iodide scintillation crystals evenly spaced along the circumference of the ring as the elements of the second, position-sensitive ring detector [Martin 1994]. Another demonstrated system uses eight high-purity germanium (HPGe) detectors configured in two planes of four detectors each [McKisson 1994]. The two detector planes constitute two position-sensitive detectors in which the individual HPGe detectors are the detector elements. In both cases, efficiency is limited by the inactive space between the multiple detector elements in the ring or the plane. This project will investigate the possibility constructing a ring Compton camera

using position-sensitive scintillators as elements of a second position-sensitive ring detector and room-temperature semiconductors as elements of a first position-sensitive detector. Portability will be improved with room-temperature components, which eliminate the need for cryogenic cooling systems.

Position Sensitive Scintillators. A scintillator measures the energy of incident radiation through fluorescence, the prompt emission of visible light, following its excitation by the radiation. The intensity of the light emitted is directly related to the energy of the radiation which cased the scintillation. Due to self absorption and surface absorption, some light is lost in all scintillators before it reaches the photodetector. This attenuation can be put to use in a long, thin scintillator like thallium-doped sodium iodide (NaI(Tl)) with a photodetector (photomultiplier tubes or photodiodes, for example) placed on each end. If the response of the photodetector is assumed linear with the amount of light collected by it, then the position of an event, x, is determined from the signal produced at either end , E_1 and E_2, by the natural log of their ratio. The energy deposited is proportional to the square root of their product [Carter 1982]. These relations are described in Chapter II.

Thallium doped sodium iodide is the most widely used scintillation material for gamma-ray spectroscopy due to its good light yield, nearly linear response, and good spectral match to the sensitivity of widely used photomultiplier tubes. It has been used successfully as a position-sensitive detector [Carter 1982]. The combination of thallium doped cesium iodide (CsI(Tl)) scintillator material and mercuric iodide (HgI_2) photodiodes has been demonstrated to have advantages in gamma-ray spectroscopy [Markakis 1988][Wang 1994]. These advantages include the lower power consumption of mercuric iodide (HgI_2) photodiodes compared to photomultiplier tubes, and enhanced energy resolution. The suitability of CsI(Tl) for use as a position-sensitive detector with position and energy resolution superior to that of comparable NaI(Tl) devices has also been demonstrated [Dean 1987]. All of these are qualities from which a portable Compton scatter camera such as the device proposed in this project will benefit.

Proposed Device. A configuration of the ring Compton camera proposed here uses an octagonal ring of position-sensitive scintillator bars as the second "ring" detector and an array of room-temperature

lithium-drifted silicon (Si(Li)) detectors as the first position-sensitive detector. Such a configuration is shown in Figure 1-3.

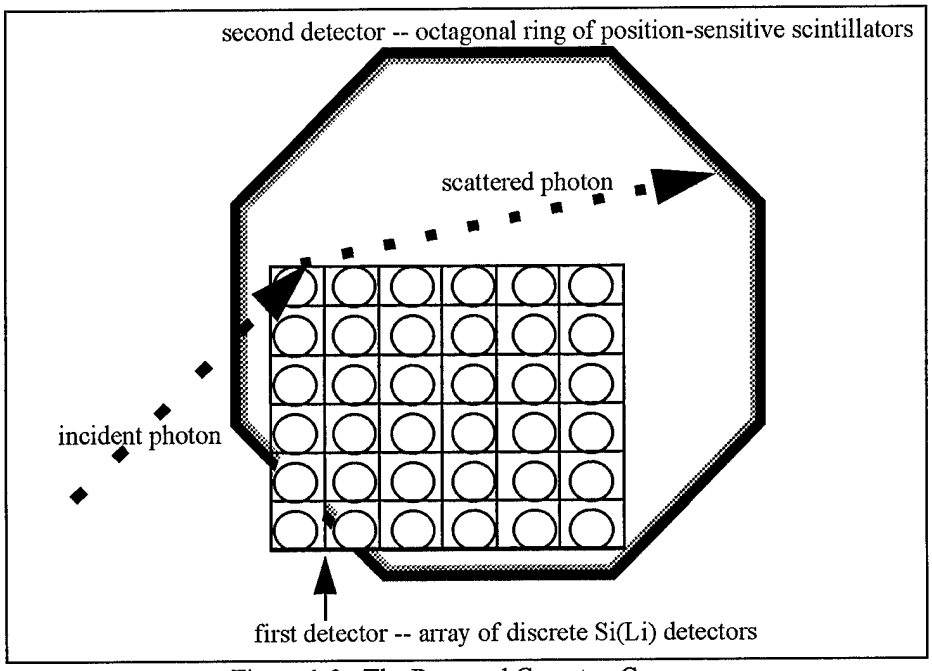

Figure 1-3. The Proposed Compton Camera

It is hoped that using this arrangement will improve upon the efficiency of existing systems by increasing the active area of the second detector -- increasing the solid angle through which a photon can scatter from the first detector and into the second. Also, the position-sensitive scintillation bars could improve upon the angular resolution of some existing systems by more precisely localizing the position of interaction in the second detector. Room-temperature components should increase portability by obviating the need for cryogenic cooling.

Objective

The primary objective of this project is to characterize the efficiency, energy resolution, and angular resolution of the proposed device. The position resolution, energy resolution, and efficiency of the detector elements will be measured. Relationships developed by Martin [Martin 1994:20-25] will describe how the uncertainties in position and energy propagate into total angular resolution of the system. A technique will be demonstrated to model, using computational methods, the response of the

position-sensitive scintillator to incident gamma rays in the energy region of interest. The results of this model will be compared to the position and energy resolution of the actual detector. The model will be adapted to predict the response of similar devices, specifically a thallium-doped cesium iodide (CsI(Tl)) position-sensitive scintillator, and thus the angular and energy resolution of a similar system which uses CsI(Tl) in place of NaI(Tl).

Scope

The purpose of this project is to evaluate the feasibility of the system configuration discussed above for eventual use in an operational system. If the performance of the system is adequate for the counterproliferation role, then a full-scale system could be constructed using similar components. The computational model is presented as a possible tool to aid in the development of similar systems.

General Approach

To establish the angular and energy resolution of a Compton gamma-ray camera, the position and energy resolution of the two detector elements must be ascertained.

The determination of the first detector's position resolution is trivial because the event position cannot be localized to a volume smaller than that of a detector element. The energy resolution of this detector is determined conventionally by calibration with radioisotopes emitting known energies.

The position and energy resolution of the second detector element, the position-sensitive NaI(Tl) scintillator, is measured using a CAMAC (Computer Automated Measurement and Control) data acquisition system to record the response of the detector on an event-by-event basis. The data acquisition system is described in more detail in the Chapter III. Collimated gamma radiation in the energy region of interest is introduced at positions along the length of the scintillator to establish how position and energy resolution vary as a function of the incident energy and of the position of the event. The uncertainties in both the position of interaction and the energy deposited in the detectors will govern the overall angular and energy resolution of the system. In order to predict the angular resolution of similar systems, a

technique to model the position and energy resolution of the position-sensitive scintillator would be useful. Such a technique is presented here.

The behavior of the NaI(Tl) scintillator will be modeled computationally with the use of public domain software called DETECT which was developed at the University of Michigan. DETECT uses a Monte Carlo photon transport algorithm to model the fates of photons in the scintillator [DETECT]. Since the number of photons collected at either end of the bar is assumed linear with the signal generated by the photodetector at that end, the results of the DETECT model can be used to forecast the response of the scintillator/photodetector system to radiation at different incident positions. When the results of the model are used in relations developed by Carter [Carter 1982], they should predict the position and energy resolution of the detector as a function of energy and position on the detector. The validity of the model is established by comparison of the results to the measured data. The same computational technique is then used to estimate the resolution of a hypothetical position-sensitive CsI(Tl) scintillator, and it is shown how these results forecast the angular and energy resolution of the proposed device based on CsI(Tl) as the scintillation material.

Sequence of Presentation

Chapter II gives the reader a brief introduction to the physics of Compton scatter, the principles of Compton cameras, and the principles of position-sensitive scintillators. It also describes the factors which affect the choice of system geometry and introduces the model used to predict the system efficiency. Chapter III describes the detectors, electronics and software used in the experiment. Chapter IV details the experimental and computational procedures. Chapter V reports the results, and Chapter VI gives conclusions and recommendations for further work.

II. THEORY

The principles of position-sensitive scintillators and Compton scattering are introduced in this chapter to lay the foundation for the models developed later. The principles and angular resolution of the Compton camera were discussed in Chapter I, but three other features are discussed here: the choice of system geometry, the efficiency and the field of view.

Principles of Position-Sensitive Scintillators

Carter first described the relationships between the light collected at both ends of a long, thin bar of scintillation material and the position and energy of the interactions which produced the scintillation light [Carter 1982]. The light is attenuated, primarily through surface absorption, as it travels the length of the crystal so that the number of photons which reach one end of the crystal is

$$N_A = \frac{E_\gamma}{E_0} e^{-\alpha\left(\frac{L}{2}+x\right)} \qquad \text{(Equation 2-1)}$$

and the number of scintillation photons which reach the other end is

$$N_B = \frac{E_\gamma}{E_0} e^{-\alpha\left(\frac{L}{2}-x\right)} \qquad \text{(Equation 2-2)}$$

where x is the distance from the center of the crystal at which the photons are produced, E_γ is the incident gamma-ray energy, E_0 is the energy deposited per scintillation photon produced in the crystal, L is the length of the crystal, and α is the light attenuation coefficient per unit length. The relationships are based on the assumption that the light attenuation through the length of the position-sensitive detector is exponential. The exponential attenuation is based on Beer's law which assumes that as a photon travels through a differential distance dx in the x-direction, it has a finite probability of being lost through absorption. This probability remains constant along the length L. If the number of photons is large, then the exponential light attenuation is obtained.

The photons which reach the end of the crystal are collected by some type of photodetector, a photomultiplier tube or photodiode for example. If P is defined as the total probability that a light quanta produced at one end of the crystal will produce a photoelectron in the adjacent photodetector, then the signal amplitudes from the two photodetectors can be written as

$$E_1 = P\frac{E_\gamma}{E_0}e^{-\alpha\left(\frac{L}{2}+x\right)} \qquad \text{(Equation 2-3)}$$

$$E_2 = P\frac{E_\gamma}{E_0}e^{-\alpha\left(\frac{L}{2}-x\right)} \qquad \text{(Equation 2-4)}$$

in arbitrary units since no electron multiplication in the photodetectors is accounted for.

If x is redefined as the distance of the scintillation event from one end of the crystal, then the position of interaction can be determined by solving Equations 2-3 and 2-4 for x. The position is related to the ratio of E_2 to E_1 [Carter 1982].

$$x = \frac{1}{2\alpha}\ln\left[\frac{E_2}{E_1}\right] + \frac{L}{2} \qquad \text{(Equation 2-5)}$$

The energy deposited in the detector is found by multiplying Equation 2-3 and Equation 2-4 and solving for $E\gamma$. The energy deposited is proportional to the square root of the product of E_1 and E_2.

$$E_\gamma = \frac{E_0 e^{\alpha L/2}}{P}\sqrt{E_1 E_2} \qquad \text{(Equation 2-6)}$$

According to Poisson statistics, the standard deviations in the signals are equal to the square roots of E_1 and E_2. The standard deviation in position is then found from error propagation of Equation 2-5.

$$\sigma_x = \frac{e^{\alpha L/4}}{2\alpha}\sqrt{\frac{e^{\alpha\left(x-\frac{L}{2}\right)} + e^{-\alpha\left(x-\frac{L}{2}\right)}}{E_\gamma P / E_o}} \qquad \text{(Equation 2-7)}$$

Similarly, error propagation in Equation 2-6 gives the energy resolution in relative FWHM as

$$\sigma_E = \frac{2.35 \cdot e^{\alpha L/4}}{2} \sqrt{\frac{e^{\alpha\left(x-\frac{L}{2}\right)} + e^{-\alpha\left(x-\frac{L}{2}\right)}}{E_\gamma P / E_o}} \qquad \text{(Equation 2-8)}$$

Dean points out that if the value of α is small enough for the light attenuation to be approximated by a linear function, then an estimate of the energy is obtained by the sum of the two photodetector signals, so that [Dean 1987]

$$E_\gamma \propto E_1 + E_2 \qquad \text{(Equation 2-9)}$$

and that an estimate of position is given by the difference between them so that

$$x \propto E_2 - E_1 \qquad \text{(Equation 2-10)}$$

However Equation 2-10 cannot work when the detector is exposed to polychromatic radiation or to radiation which Compton scatters in the detector and escapes, depositing a different fraction of the full gamma-ray energy each time. To correct for this, the difference can be normalized by the recorded energy to correct for the different number of scintillation photons which will be produced, as follows:

$$x \propto \frac{E_2 - E_1}{E_2 + E_1} \qquad \text{(Equation 2-11)}$$

Monoenergetic gamma rays at the energies of concern in this study can be expected to deposit a wide range of energies by Compton scatters within the detector in which the scattered photon escapes.

One physical phenomena which is present in both the detector and the DETECT computer simulation which is unaccounted for in the Beer's law attenuation model is the possibility of a photon traveling in the positive x-direction scattering into the negative x-direction, then scattering again into the positive x-direction. This photon could reappear in the differential distance dx from which it originally scattered, although the Beer's law attenuation considered it lost to absorption. A model which accounts for both absorption and scatter might more realistically model the light attenuation through the detector.

Kubelka-Munk theory provides a solution for the light attenuation through substances which are capable of both scattering and absorption [Kortum 1969:106]. If a layer of thickness d capable of both

scattering and absorption is irradiated by diffuse, monochromatic radiation flux, the transmittance of such a layer is given by T in Equation 2-12.

$$T = \frac{(1 - R_\infty)^2 e^{-bSd}}{1 - R_\infty{}^2 e^{-2bSd}} \qquad \text{(Equation 2-12)}$$

where R_∞, b, and S are parameters which describe the scattering and reflectance properties of the substance from which the layer is composed. Equation 2-12 was derived for a solid layer in which scattering and absorption can occur anywhere, whereas in the case of the position-sensitive detector, scattering and absorption occur primarily along the edges of the crystal at the diffuse reflector. The functional form of the Kubelka-Munk expression for T (Equation 2-12) may describe light attenuation through the position-sensitive scintillator, but the values of R_∞, and the product bS depart from the values available for solid substances.

The proposed device uses position-sensitive scintillators as elements of the second detector. The radiation incident on these detector elements will not be the incident gamma-ray energy, but rather the energy of the photon scattered from the first detector. The relationships between the incident gamma-ray energy, the scattered photon energy, the recoil electron energy, and the scattering angle are well-established.

Physics of Compton Scattering

When a photon with incident energy E_γ Compton scatters with an orbital electron, the electron is given a recoil energy and the photon is deflected through an angle θ given by Equation 1-1. E_{re}, the energy imparted to the recoil electron is related to the scattering angle of the photon by

$$E_{re} = \frac{E_\gamma}{1 + \alpha[1 - \cos(\theta)]} \alpha[1 - \cos(\theta)] \qquad \text{(Equation 2-13)}$$

and the energy of the scattered photon is given by

$$E_\gamma{}' = \frac{E_\gamma}{1+\alpha\left[1-\cos(\theta)\right]} \qquad \text{(Equation 2-14)}$$

Compton, or incoherent, scatter is the predominant interaction in detector material for medium energy gamma rays. The likelihood that a photon undergoes a particular type of reaction per unit path length is specified by that reaction's partial interaction coefficient.

The probability of a scattered gamma ray being emitted at a particular angle is given by the Klein Nishina relation, Equation 2-15. It expresses this probability as a differential cross section, σ, with solid angle Ω. Z is the atomic number of the target element and r_0 is the classical electron radius.

$$\frac{d\sigma}{d\Omega} = Z{r_o}^2\left\{\frac{1}{1+\alpha\left[1-\cos(\theta)\right]}\right\}^2\left\{\frac{1+\cos^2(\theta)}{2}\right\}\left\{1+\frac{\alpha^2\left[1-\cos(\theta)\right]^2}{\left[1+\cos^2(\theta)\right]\left[1+\alpha\left[1-\cos(\theta)\right]\right]}\right\}$$

(Equation 2-15)

Figure 2-1 illustrates how $d\sigma/d\Omega$ varies as a function of the scattering angle θ for three different incident gamma-ray energies.

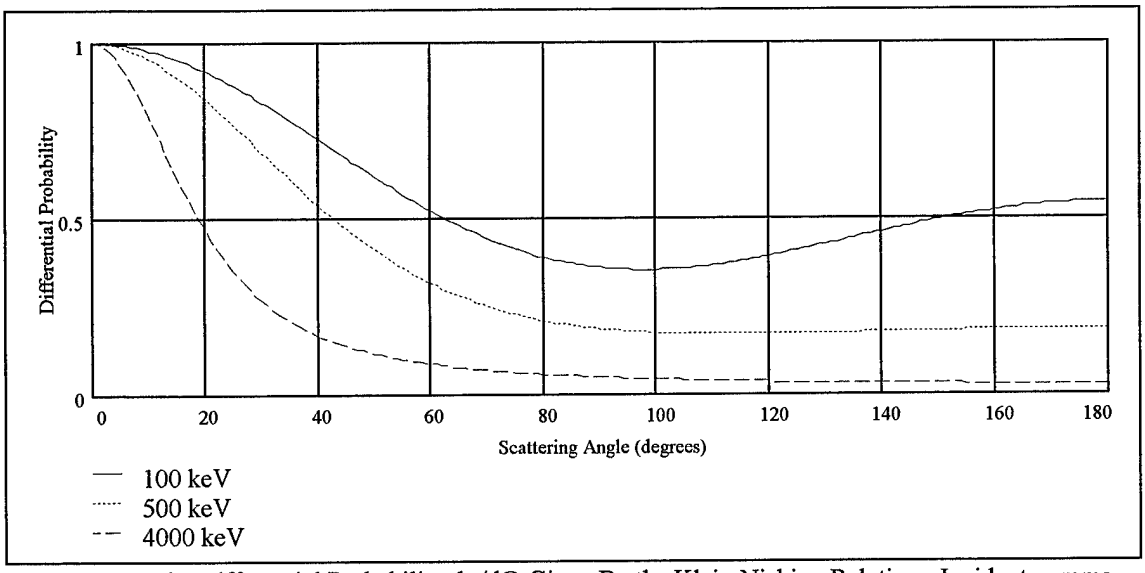

Figure 2-1. The Differential Probability $d\sigma/d\Omega$ Given By the Klein Nishina Relation. Incident gamma-ray energies of 100, 500, and 4000 keV are shown.

Choice of System Geometry

The positions at which the detector elements in the Compton camera are placed relative to each other will be called the system geometry. Several factors affect the choice of the optimum system geometry. The two main parameters to be considered are the geometry of the octagonal second detector and the central scattering angle.

The choice of the geometry of the octagonal second detector is made on the basis of the position resolution of the second detector elements as a function of the position of interaction. Separating the constants from Equation 2-7 and defining x to be the position of the interaction relative to the center of the bar gives

$$\sigma_x = \frac{e^{\alpha L/4}}{2\alpha\sqrt{E_\gamma P / E_o}}\sqrt{e^{\alpha x} + e^{-\alpha x}}$$

Setting

$$k = \frac{e^{\alpha L/4}}{2\alpha\sqrt{E_\gamma P / E_o}}$$

and plotting σ_x/k as a function of x as in Figure 2-2 reveals that the position resolution is degraded at the ends, and is best in the center. The sodium iodide crystal in the position sensitive scintillator used in this study is 30 cm in length. The proposed system will avoid using the poorly resolved ends of the bars by shielding 5 cm on each end or by rejecting events which interact in the ends. The resulting octagonal ring detector will be 20 cm on each side. Figure 2-3 illustrates such an octagonal ring.

Another important aspect of the system geometry is the central scattering angle, the angle at which a photon incident along the detector axis would scatter from the center of the first detector into the center of the second detector. Several factors must be considered in the selection of a central scattering angle. The first of these is the range of recoil electrons in the first detector element.

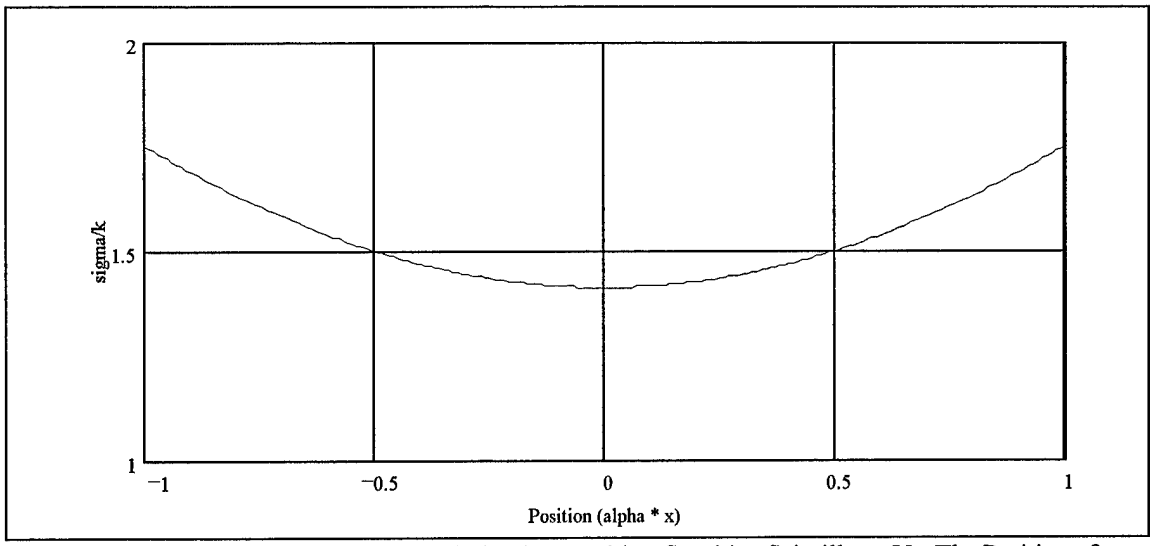

Figure 2-2. Theoretical Position Resolution in a Position-Sensitive Scintillator Vs. The Position of Interaction. The resolution is expressed as the standard deviation in x divided by the constant k (σ_x/k). The position is expressed as the product of the distance from the center of the crystal and the light attenuation coefficient (αx).

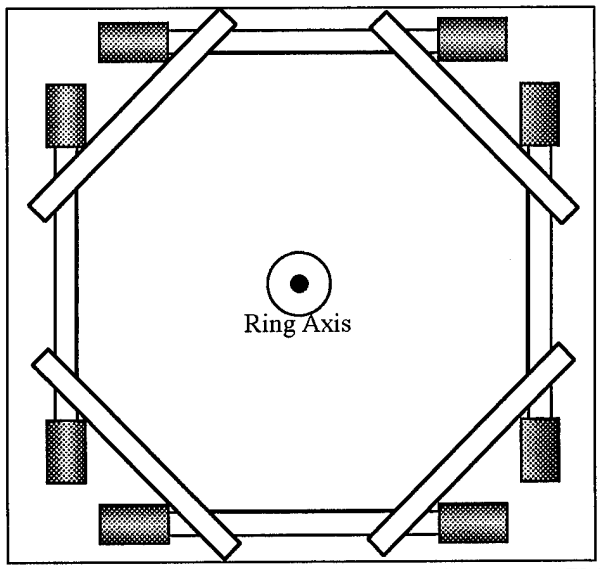

Figure 2-3. Proposed Configuration of the Octagonal Ring Second Detector. PMT tubes are shown at the ends of some of the detector elements.

The first detector (a room temperature Si(Li)) used in this study has an active area in the shape of a right circular cylinder. The cylinder is 5.64 mm in diameter and 5.00 mm in height. The maximum dimensions of the active volume of this first detector element are limited by the poor position resolution which would result from a large detector volume. The minimum dimensions are limited by the range of

the recoil electron from the Compton scatter which occurs in the silicon crystal. Electron-hole pairs whose charge is the basis of the detector signal are formed by the recoil electron along its path. If the dimensions of the silicon crystal are not comparable to the recoil electron path length, too many recoil electrons will escape the detector without depositing their full energy, and therefore give erroneous energy data. Figure 2-4 shows that at energies greater than 2.2 MeV, the recoil electron path length is greater than the dimensions (0.5 cm) of the detector crystal.

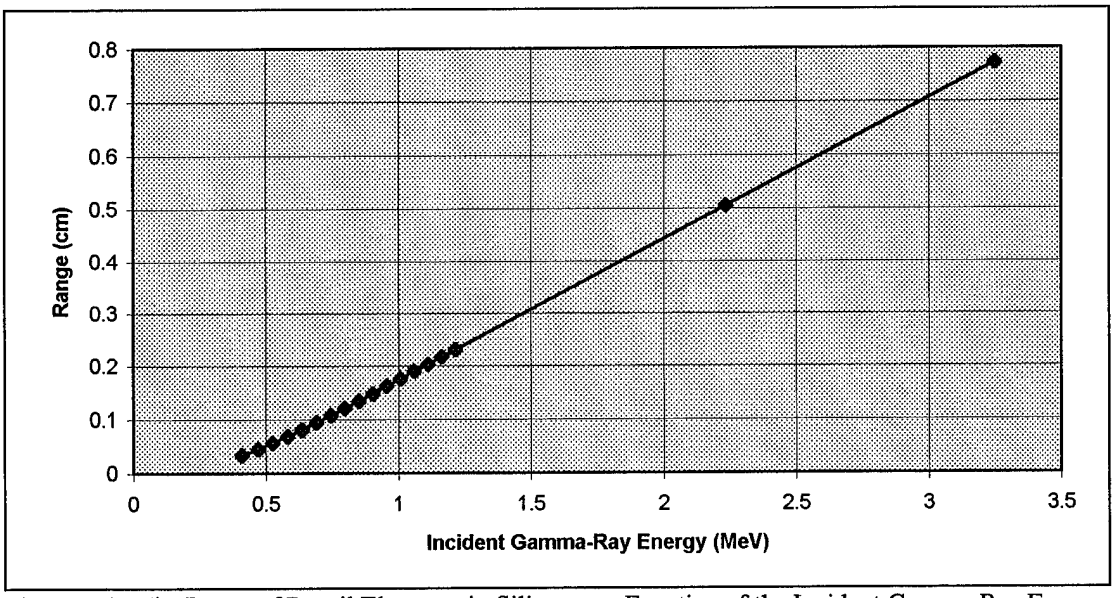

Figure 2-4. The Range of Recoil Electrons in Silicon as a Function of the Incident Gamma-Ray Energy. A central scattering angle of 60 degrees is assumed. Electron range data was taken from [Pages 1972].

To image these higher energies, a smaller central scattering angle would need to be selected, or a larger first detector element would need to be used. Some results from this project will be reported out to 3 MeV with the understanding that larger first detector elements are needed to image above 2.2 MeV. A larger first detector element might adversely affect angular resolution by increasing the position uncertainty of the Compton scatter, so this possibility will be investigated. Three factors also discourage the use of a narrower central scattering angle; they are the increased energy of the scattered photon, the increased probability of incoherent scatter, and the large deviation of scattering angle θ with the recoil electron energy ($\partial\theta/\partial E_{re}$) which occurs at smaller scattering angles.

First, as the scattering angle is decreased, the energy of the scattered photon increases. The higher energy scattered photons have a lower probability of photoelectric absorption and higher probability of Compton scatter in the second detector. This results in a lower peak-to-total ratio (fewer full-energy events) in the second detector which translates into degraded efficiency.

Secondly, at smaller scattering angles and lower gamma-ray energies, the probability for coherent scatter increases. In this interaction, a gamma ray scatters off an orbital electron, but maintains its previous energy while changing its direction. If a gamma ray coherent scatters in the first detector and into the second, no energy would be deposited in the first detector, but some or all the incident energy may be deposited in the second detector. These two factors combined result in a lower signal-to-noise ratio at smaller angles.

The third reason for avoiding small central scattering angles is revealed by differentiating Equation 1-1 with respect to E_{re}:

$$\frac{\partial\theta}{\partial E_{re}} = \frac{m_o c^2}{\sin(\theta)}\left[\frac{1}{\left(E_\gamma - E_{re}\right)^2}\right] \qquad \text{(Equation 2-16)}$$

Figure 2-5 shows $\partial\theta/\partial E_{re}$ as a function of scattering angle θ. As θ approaches 0 and 180 degrees, the $\sin(\theta)$ term in the denominator causes the derivative to become infinite. As this derivative becomes infinite, so too will the angular resolution.

The combination of these factors makes the selection of a central scattering angle non-trivial. Based on previous work [Martin 1994:168-175], an angle of 60 degrees was selected for this project. Unlike a truly ring-shaped second detector, the central scattering angle will vary slightly in the octagonal second detector. The geometry of the detector is chosen so that a central scattering angle of 60 degrees causes a photon incident along the ring axis to scatter into the center of one of the position-sensitive scintillators at a position 5 cm from the midpoint of the detector length. The choice of this central scattering angle will affect virtually all aspects of the Compton camera, including the angular resolution and the efficiency.

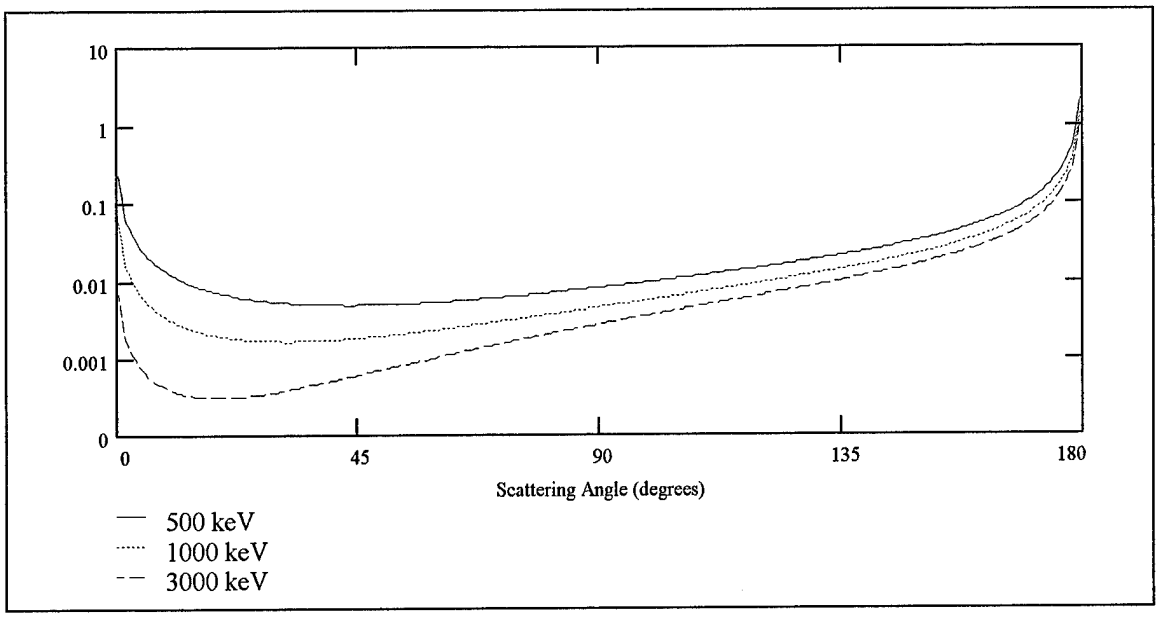

Figure 2-5. $\partial\theta/\partial E_{re}$ vs. Scattering Angle for Various Incident Gamma-Ray Energies.

Efficiency Model

Martin developed a model of the efficiency of the Ring Compton Camera in response to a point source located on the ring axis [Martin 1994:14-19]. A single element is modeled as the first detector. The absolute efficiency, ε_{acc}, is the product of four terms, each representing an independent random process. The product is the probability that an incident gamma ray Compton scatters once in the first detector and the scattered photon escapes and deposits its full energy in the second detector.

$$\varepsilon_{acc} = \left(\frac{\Omega_1}{4\pi}\right) P_c f_2 \varepsilon_{ip2} \qquad \text{(Equation 2-17)}$$

The first term in Equation 2-17 is simply the fraction of solid angle subtended by the first detector. It represents the probability that a gamma ray emitted by the source will fall on the first detector assuming isotropic emission. The equation without this term gives the intrinsic efficiency.

The second term P_c represents the probability that an incident gamma ray Compton scatters in the first detector, escapes the detector, and is emitted into an angle θ in which the second detector lies. This term is given as:

$$P_c(E_\gamma) = \frac{\frac{\sigma}{\mu}\left(1 - e^{-\mu 2 L_1}\right) \int_{\theta\min}^{\theta\max} P(\theta, E_\gamma) e^{-\mu'(\theta) S(\theta)/2} d\theta}{\int_0^{\pi} P(\theta, E_\gamma) d\theta} \qquad \text{(Equation 2-18)}$$

where

$$P(\theta, E_\gamma) = \frac{\sin(\theta)\left(\frac{d\sigma}{d\Omega}(E_\gamma)\right)}{Z r_o^2} \qquad \text{(Equation 2-19)}$$

and $d\sigma/d\Omega$ is given by the Klein-Nishina relation (Equation 2-15). Other symbols are defined as follows:

L_1 = half the length of the first detector

μ = the total interaction coefficient in the first detector at the incident gamma ray energy E_γ

σ = the Compton scatter partial interaction coefficient in the first detector at the E_γ

$\mu'(\theta)$ = the total interaction coefficient in the first detector at the scattered photon energy

$S(\theta)$ = the path length traversed by the scattered gamma ray to escape the detector

θ_{min} to θ_{max} = the range of angles at which a photon can scatter from the first into the second detector

f_2 = the ratio of the area of the detector to the area of the angular scattering range. For a full ring this factor is 1.

ε_{ip2} = the intrinsic peak efficiency representing the fraction of gamma rays incident on the second detector which deposit their full energy.

If the mean free path of an incident particle in a detector is long compared to the detector's dimensions, the interactions will be approximately evenly distributed throughout the length. Since this is the case in the first detector, the interactions in this efficiency model are assumed to occur in the center.

The efficiency model presented here is for a point source located on the ring axis. However imaging will be performed on spatially extended sources. For this reason it is important to characterize the field of view of the Compton camera.

Field of View

Sources can be imaged which lie within a circular region of radius r_{df} around the detector axis [Martin 1994:109-112]. Outside of this region, gamma rays will not be recorded in all parts of the second detector. This unbalanced response will distort recorded images. This region is determined by the

Compton central scattering angle θ_c, the scattering angle lower bound θ_l, and the distance from the source to detector, z_s.

$$r_{df}=z_s \tan(\theta_c-\theta_l) \qquad \text{(Equation 2-20)}$$

θ_l is governed by a lower energy threshold set in the first detector. Setting this threshold in the first detector is tantamount to using scattering events in which at least some minimum energy is imparted to the recoil electron. If the minimum electron recoil energy is labeled E_{lmin}, Equation 1-1 gives θ_l as:

$$\cos(\theta_l) = 1 - \left[\frac{E_{l\,\min}}{\alpha(E_\gamma - E_{l\,\min})} \right] \qquad \text{(Equation 2-21)}$$

For sources which lie outside the field of view, a recoil electron energy less than E_{lmin} will be deposited in the first detector when the photon scatters into some regions of the second detector. Figure 2-6 illustrates the field of view. If the scattered photon follows the path marked a, the event will not be recorded because the energy of the recoil electron is below the threshold E_{lmin}; if it follows the path marked b, the event will be recorded because the recoil electron energy is above the threshold E_{lmin}. Recoil electrons from sufficiently energetic sources within the field of view will always have energy above E_{lmin}, thus creating an even response.

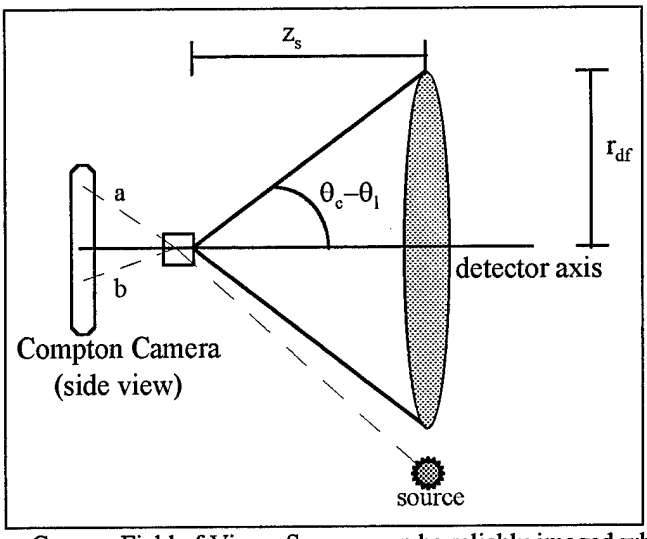

Figure 2-6. Compton Camera Field of View. Sources can be reliably imaged which lie in a circular region indicated by the gray shaded area of radius r_{df}.

III. EQUIPMENT

The primary equipment components used in this project are the first detector element, the second detector element, the data acquisition system, and the scintillator modeling program DETECT.

First Detector Element

The first detector element used in this project is an EG&G ORTEC Model L-035-025-5. The detector is a lithium-drifted silicon semiconductor detector (Si(Li)) which operates at room temperature. The active volume of the silicon crystal is in the shape of a right circular cylinder. The base of the cylinder is 25 mm^2 in area and the active depth is 5 mm as illustrated in Figure 3-1. It operates at a bias of +1000 volts. A thin gold evaporation entrance window is located at one base of the cylinder. The detector is oriented such that this entrance window "looks at" the incident radiation. In the proposed system, an array of such detectors will be used to create a position-sensitive first detector.

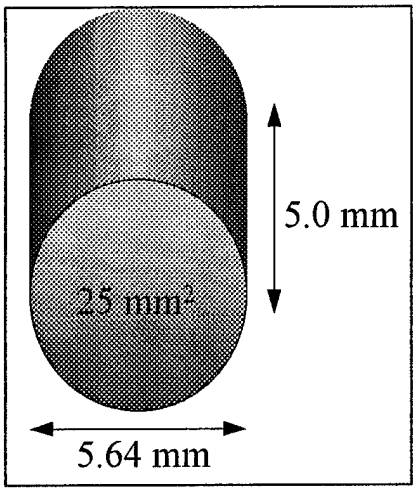

Figure 3-1. Dimensions of the Active Volume of the First Detector Element.

The manufacturer reports a resolution of 35 keV FWHM for alpha particles and a resolution of 30 keV FWHM for beta particles. These resolutions are given independent of energy and no resolution for photons is reported. However since the energy of an incident photon is imparted to an electron whose energy is then measured, the process for photon spectroscopy is similar to that of beta spectroscopy, and a similar 30 keV resolution can be expected. Because the resolution in room temperature semiconductor

detectors is dominated by thermal noise, this resolution is expected to remain fairly constant over the energy range of interest.

Second Detector Element

The second detector element is a position-sensitive scintillator custom manufactured by Bicron, Inc. for this experiment. Some properties of this detector are illustrated in Figure 3-2. It consists of a 5.08 cm x 30.00 cm x 1.90 cm thallium-doped sodium iodide (NaI(Tl)) crystal surrounded by a diffuse reflector with a reflectivity 85% that of magnesium oxide. The crystal and reflector are encased in a thin aluminum housing. At either end of the crystal are Pyrex optical windows which interface the crystal to the photomultiplier (PMT) tubes. The PMT tubes are 8-stage Hamamatsu R1306 types. ORTEC Model 266 PMT bases were used which were modified from 10-stage bases to work with the 8-stage PMTs.

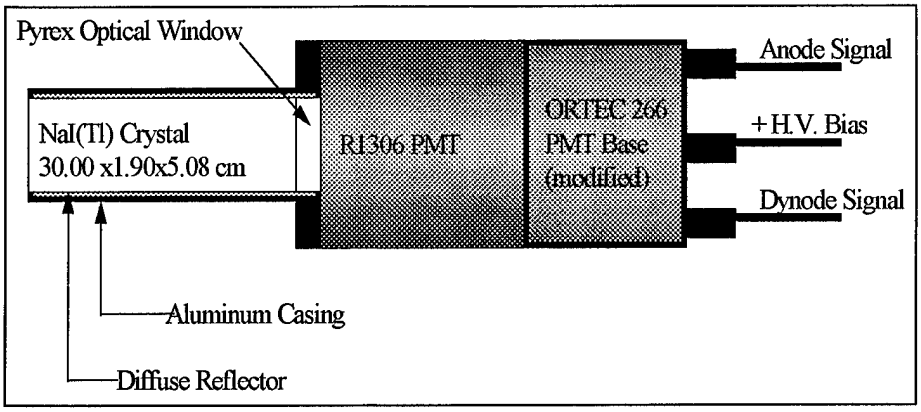

Figure 3-2. One End of the Position Sensitive Scintillation Detector Element

The data in Figure 3-3 were provided by the manufacturer. The figure shows the PMT signal amplitudes from both ends as a function of the position of incident radiation. Both linear and exponential least-squares fits have been applied to both sets of data.

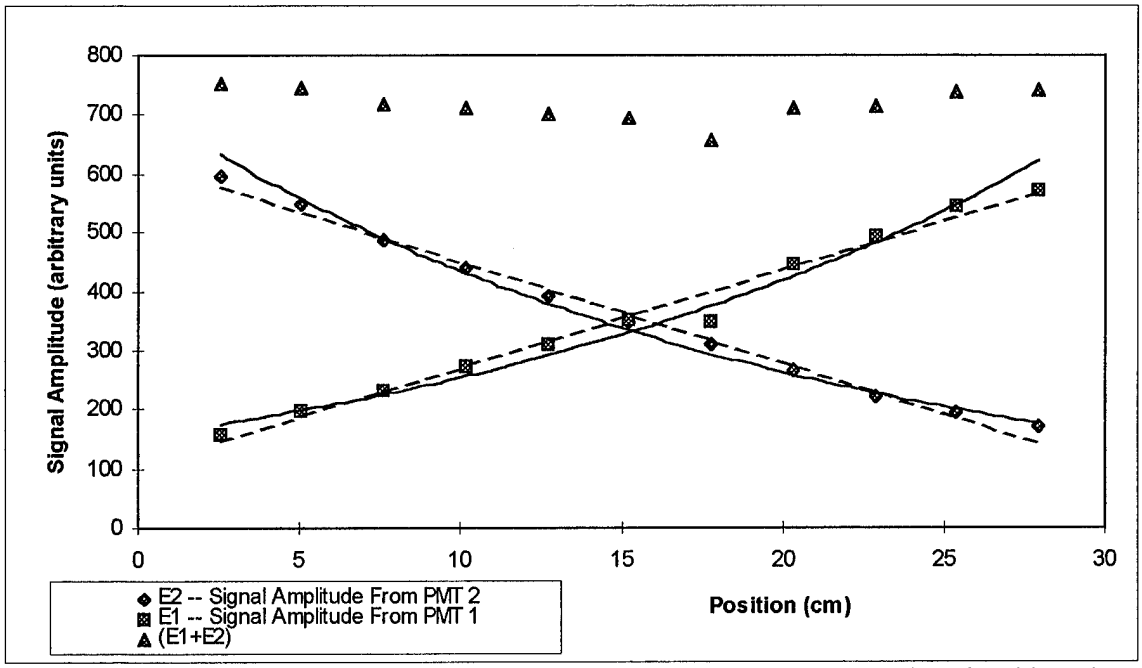

Figure 3-3. The Signal Amplitude in Arbitrary Units From Both PMTs as a Function of Position. A linear and exponential fit to both sets of data is also shown.

Since neither fit accurately predicts the location of the data points, it is evident that the light attenuation in the detector is neither perfectly linear nor perfectly exponential. Therefore methods were investigated for finding position of interaction and energy deposited in this detector which are founded on both linear (Equation 2-9, Equation 2-10, Equation 2-11) and exponential (Equation 2-5, Equation 2-6) attenuation. Because the attenuation was neither linear nor exponential, it was expected that either a linear or exponential method would yield better results for position determination, and that either a linear or exponential method would yield better results for spectroscopy.

To investigate the properties of the position-sensitive scintillator and the room-temperature semiconductor detector, a system for processing and recording the signals from the detectors was required.

Data Acquisition System

The entire system by means of which the necessary data was acquired in this experiment will be referred to as the data acquisition system. The data acquisition system can be resolved into two major components which will be called the signal processing system and the data recording and analysis system. The configurations of the signal processing system and the data recording system which were used to

investigate the position and energy properties of the position-sensitive scintillator are introduced first, then the modifications to this system which were necessary to record the properties of both detectors in coincidence are discussed.

Signal Processing System. The purpose of the signal processing system is to transform the raw signal from the photomultiplier tubes into useful energy signals (i.e. shaped pulses of the appropriate amplitude) that the data recording and analysis system can use. The modular electronics which make up the signal processing system are based upon the NIM (Nuclear Instrumentation Module) instrumentation standard and are shown in Figure 3-4. Two distinct signal paths are delineated in the signal processing system: the energy signal path and the timing signal path. The electronic components which make up the energy signal path are shaded gray in Figure 3-4; the electronic components which make up the timing signal path are white.

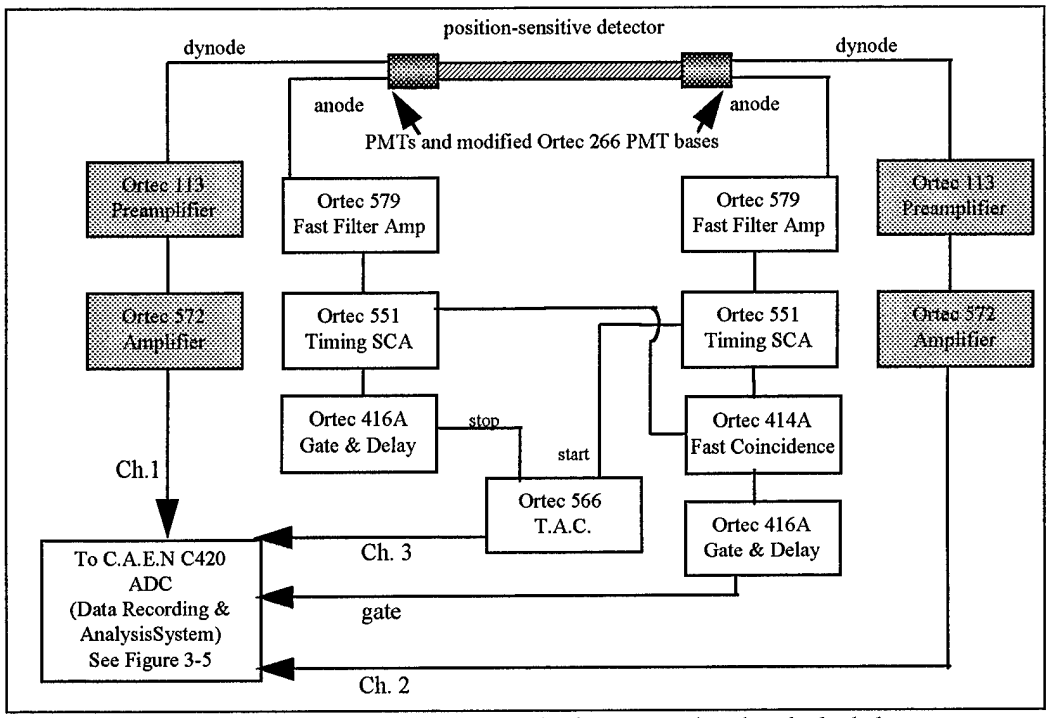

Figure 3-4. Signal Processing System. Components in the energy signal path shaded gray; components in the timing signal path are white.

The energy signal path begins with the signal from the PMT dynode. The preamplifier and amplifier shapes and amplifies these signals into semi-gaussian unipolar pulses which are then digitized

by the ADC (which acts as the interface between the signal processing system and the data recording and analysis system) in channels 1 and 2. A 2-microsecond delay is introduced in the amplifier so that the energy signals arrive in coincidence with the timing signal.

The timing signal path begins with the PMT anode at each end. A timing signal is extracted from the anode signal. The fast filter amplifiers shape and amplify the noisy anode signals. The timing single channel analyzers (TSCAs) produce a logic pulse whenever their respective fast filter amplifier output exceeds a lower voltage threshold. If the two logic pulses from the TSCAs arrive at the fast coincidence unit within the 70 nanosecond coincidence window, then a coincident event has been detected and the gate signal is triggered in the gate and delay generator. This gate signal notifies the ADC to record the energy signals arriving from the PMT dynodes. The timing resolution is obtained by introducing a fixed delay in one TSCA output by means of another gate and delay generator. The Time-to-Amplitude Converter (TAC) measures the time between the undelayed and delayed TAC outputs and produces a pulse whose amplitude is proportional to this time. These pulse heights are digitized in channel 3 of the ADC, which is the first component in the data recording and analysis system.

Data Recording and Analysis System. The data recording and analysis system is based on CAMAC standard electronics. All CAMAC instruments must be installed in a CAMAC crate, which provides connections for each CAMAC module. These connections provide access to the dataway, which carries control signals, digital data, and power. Digital communication between various modules in the CAMAC crate takes place over this dataway, which obviates the need for many coaxial external connections required in the older NIM system. The crate controller is a required module in any crate. It manages the communications between modules within the crate, and between the crate and the external equipment. Usually this external equipment includes a computer.

In this study, a Weiner (Weiner is a line of products produced by the German company Plein & Baus, GmbH) CC16 Crate Controller [Plein 1994] was used to control a C.A.E.N. C420 eight-channel peak-sensing [CAEN 1993] ADC. The CC16 was equipped with a personal computer interface card which was installed in one of the computer I/O ports. Through the use of this interface card and the CC16 the user can, via the personal computer, monitor and issue commands to the installed CAMAC modules.

The software used in this study to do so was the multiparameter data acquisition software "Multi", another product in the Weiner line [Plein 1993]. Each coincident event was stored a "listmode" data file for possible reevaluation. A significant feature of the multiparameter software is that it allows the user to perform simple (addition, subtraction, multiplication, and division) mathematical operations on any data collected in coincidence. This feature allowed the event-by-event extraction of position and energy information as described in the next chapter. Components of the data recording and analysis system are illustrated in Figure 3-5.

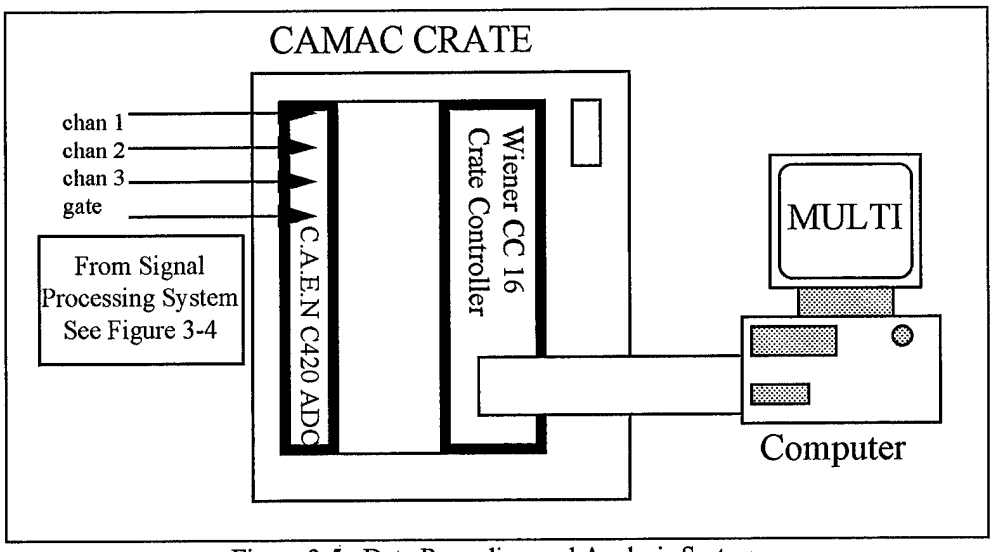

Figure 3-5. Data Recording and Analysis System.

Recording Both Detectors in Coincidence

For an unknown incident gamma-ray energy, the angular resolution of the Compton camera depends on the energy resolution obtained by summing the energies in both detectors. The energy of the incident gamma ray can be determined by summing the energy deposited in each detector event-by-event or from the summed energy of many interactions. In order to collect summed energy spectra, energy signals from both detectors need to be collected in coincidence. The data acquisition system is modified so that it selects events which deposit energy in both detectors and records those energies.

The signal processing system is configured as shown in Figure 3-6. Timing signals are picked off from one end of the position-sensitive detector and from the first detector. Fast filter amplifiers coupled to timing single-channel analyzers produce timing signals. If these timing signals are within the

resolving time set on the fast coincidence unit, then a gate is generated and the ADC records the energy signal from both ends of the second detector (channels 1 and 2) and the first detector (channel 3). The delay between timing signals is again measured by a time-to-amplitude converter to produce a timing spectrum. An ORTEC Model 142 preamplifier and ORTEC Model 572 Amplifier shape and amplify the energy signal from the first detector. The energy signal path from the second detector remains unchanged. An additional energy signal meant that an additional channel was used in the ADC; otherwise the data recording and analysis system remains unchanged.

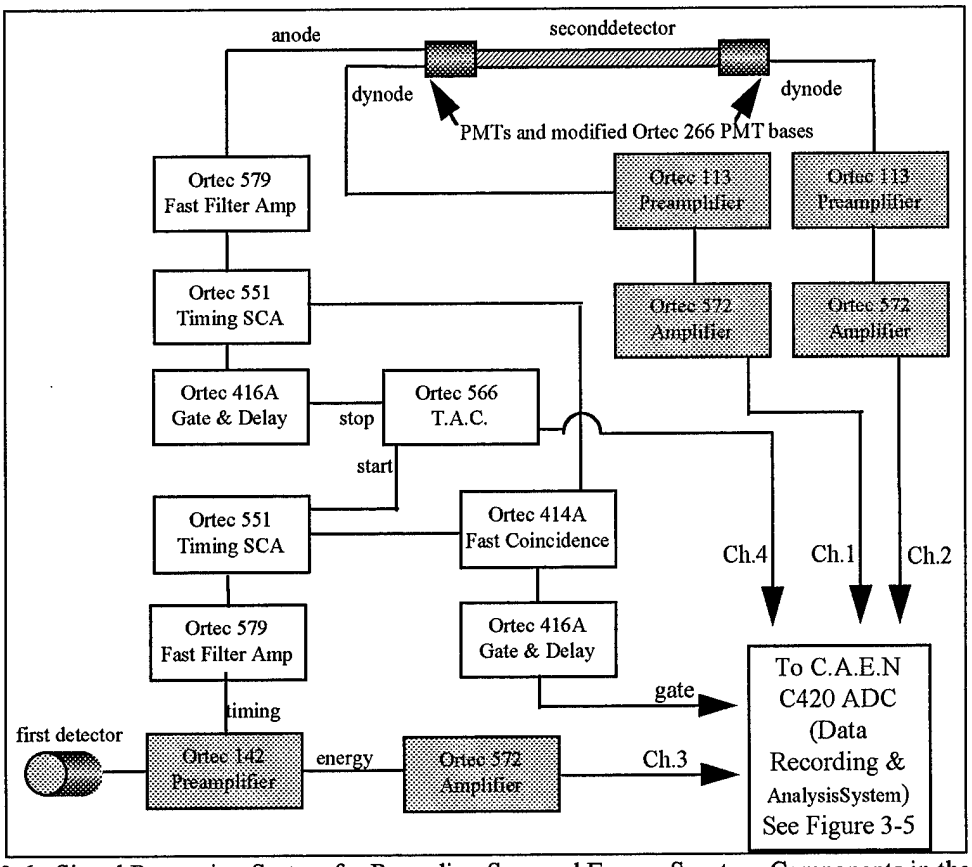

Figure 3-6. Signal Processing System for Recording Summed Energy Spectra. Components in the energy signal path shaded gray; components in the timing signal path are white.

DETECT Software

The program DETECT is written in the Pascal language and is a Monte Carlo model of the optical behavior of scintillation detectors [DETECT].

DETECT provides a syntax through which the user can specify a geometry composed of planes, cylinders, cones, etc. Components are specified within the boundaries of the surfaces of these geometric objects. The optical properties of these components are specified by their index of refraction, their mean free path to absorption, and their waveshifting properties. Several treatments are available for the surfaces of components including diffuse and spectral reflecting surfaces with a specified reflectivity, optically smooth surfaces, ground optical surfaces, and a photodetecting surface. Surfaces in optical contact are treated using Snell's law of refraction.

The user specifies the number of individual scintillation photons to be simulated and defines the particular volume of the scintillator in which the photons will be isotropically generated. DETECT then follows each photon in its passage through the various components and interactions with surfaces, allows for the possible absorption and re-emission by a waveshifting component, and records the fate of each. The probabilities of these processes are derived from the results of multiple histories involving the simulation of many scintillation photons. Data are also recorded on the number of reflecting surfaces encountered and the photon flight time to detection. Each photon is followed until it is absorbed, escapes the detector, is detected, or exceeds a user-defined maximum lifetime.

The DETECT code used in this project was compiled to run in MS DOS. A copy of the input file is available in Appendix A.

IV. PROCEDURE

To forecast the angular and energy resolution of the proposed gamma-ray imaging system, it was first necessary to measure the energy resolution of the first detector element, and to model the position and energy resolution of the second detector element. To model these resolutions, certain parameters were drawn from the results of the DETECT simulation. To verify the validity of the model, however, it was also necessary to measure the position and energy resolution of the second detector element. It was also necessary to characterize the positional uncertainty which results from the width of the collimated radiation beam illuminating the second detector element.

Measuring Energy Resolution of First Detector

The energy resolution of the room-temperature Si(Li) detector was calibrated using the photopeaks and Compton edge energies of the isotopes ^{57}Co and ^{133}Ba (122 keV, 136 keV, 207 keV and 356 keV). The energy resolution in FWHM was then determined from the spectra collected from these isotopes. The probability that a gamma ray will deposit its full energy in the small detector volume decreases rapidly as the photon energy increases. Consequently, energy resolution from photopeak or full-energy events is more difficult to determine at higher energies.

Measuring Position and Energy Resolution of the Position-Sensitive Detector

The CAMAC multiparameter data acquisition system made it possible to simultaneously measure the position, energy, and timing signals of the position-sensitive scintillator. Two additional parameters were defined which calibrate the signal received at either end. With a source placed in the middle of the detector length, these parameters (P4 and P5) returned the channel number which corresponded to the energy of the incident radiation (i.e. channel 835=835 keV). These calibrations were established from various energies of gamma radiation incident on the center of the detector. The following gamma ray energies were used in the calibration:

Table 4-1
Isotopes and Energies used For Energy Calibration of Position-Sensitive Detector

ENERGY	ISOTOPE
511.0 keV	^{22}Na
661.6 keV	^{137}Cs
834.8 keV	^{54}Mn
898.0 keV	^{88}Y
1173.2 keV	^{60}Co
1274.6 keV	^{22}Na
1332.5 keV	^{60}Co
1836.1 keV	^{88}Y

From Equation 2-5, the natural logarithm of the ratio P4/P5 is proportional to the position of interaction in the detector. From Equation 2-6, the square root of the product P4*P5 should return the incident gamma ray energy in keV. The effect of the P4 and P5 calibrations is to set the constants in Equation 2-6 to unity. i.e.

$$\sqrt{E_A E_B} = E_\gamma \frac{\sqrt{PE_o}}{e^{\alpha L/2}} \text{ where } \frac{\sqrt{PE_o}}{e^{\alpha L/2}} = 1$$

and to calibrate the energy signals such that the natural log of their ratios is unity at the center of the detector, thus returning a position of (L/2) according to Equation 2-5.

An additional parameter P6 was defined within the software which divided the two coincident PMT signals to obtain position information. Another parameter P8 was defined which multiplied the two PMT signals to obtain energy information. These additional parameters were digitized and binned to produce 4096-channel spectra. Scaling integers were introduced to ensure that the resultant spectra filled up an adequate number of channels (multiplying by 1000) and remained in the range of 0-4095 (dividing by 2000) constrained by the 12-bit ADC. A summary of the parameters is in Table 4-2.

Table 4-2
Parameters Defined Within the Data Acquisition System to Give Timing, Position, and Energy Information.

PARAMETER	DEFINITION	DESCRIPTION
P1	P1	Energy signal from PMT 1
P2	P2	Energy signal from PMT 2
P3	P3	Timing signal From TAC
P4	((P1*948)/1000)-19	E_1, energy calibration from PMT 1, channel # = keV (in center)
P5	((P2*945)/1000)-13	E_2, energy calibration from PMT 2, channel # = keV (in center)
P6	(P5*1000)/P4	E_2/E_1, used for position
P7	(P4*1000)/P5	E_1/E_2, used for position
P8	(P4*P5)/2000	E_1*E_2, used to find E_γ

With the data acquisition system configured as above, the position-sensitive detector was illuminated with gamma rays of selected energies at selected positions.

The detector was irradiated with 834.5 MeV gamma rays from ^{54}Mn at 5.0, 7.5, 10.0, 12.5, 15.0, 17.5, 20.0, 22.5, and 25.0 cm along its 30 cm length. The detector was also irradiated at 5.0 cm and 15.0 cm with 511.0 keV, 661.6 keV, 898.0 keV, 1274.6 keV, and 1836.1 keV.

The resulting spectra were loaded into a spreadsheet, rescaled, and given the appropriate transformation. In the case of the position spectra, this involved dividing the channel number by 1000 then taking the natural log. In the case of the energy spectra, this involved multiplying the channel number by 2000 and taking the square root. Figure 4-1 shows examples of position and energy spectra obtained in this manner. No transformation was needed for the timing spectra since the channel number is directly proportional to the time between events. The FWHM of the timing peak represents the variation in the time recorded between coincident events. To calibrate the timing spectra, additional known delays were added to the TAC stop signal. By noting the resulting shift in channels of the timing peak centroid, a calibration of 0.477 ns/channel was calculated.

The resulting spectra were then analyzed to determine the following parameters as a function of both position and energy: the position signal, the position resolution, the energy signal, the energy resolution, and the timing resolution.

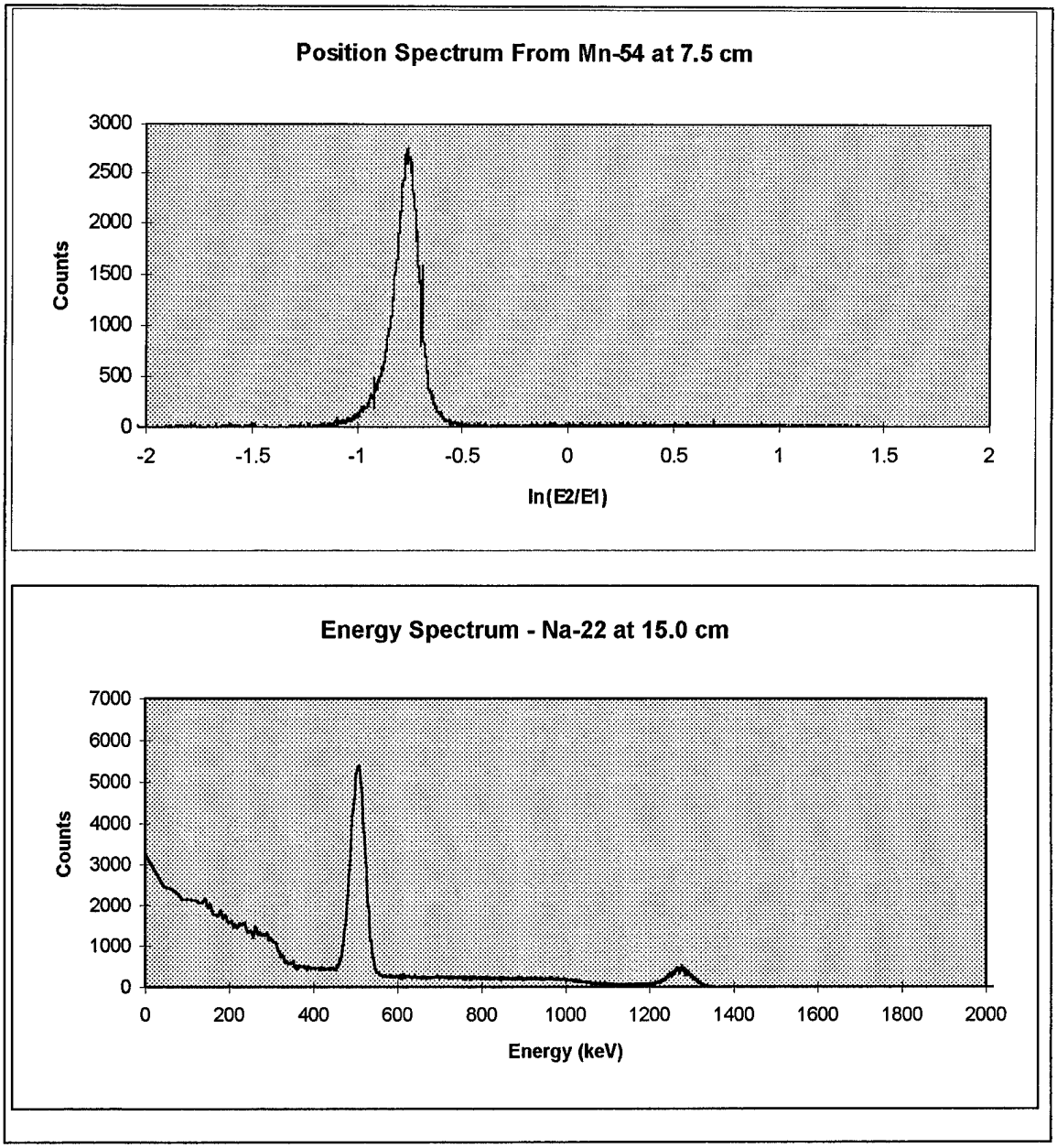

Figure 4-1. Example Position and Energy Spectra From The Position-Sensitive Scintillator. The position spectrum was produced based on Equation 2-5 by illuminating the position-sensitive detector with ^{54}Mn for 20 minutes at 7.5 cm along the 30 cm length of the detector. The energy spectrum was produced based on Equation 2-6 by illuminating the position-sensitive detector with ^{22}Na for 20 minutes at 15.0 cm.

Because every event was stored in a binary data file, the parameters could be redefined and the experiment repeated by reading the same set of data. This allowed an alternative determination of the energy response of the position-sensitive detector based on summing the energy signal from both ends of the

detector as in Equation 2-9. The data from all isotopes at the positions described above were reloaded into the Muti software [Plein 1993]. The necessary change was a redefinition of parameters as shown in Table 4-3.

Table 4-3
Secondary Parameters for Investigation of the Energy Response Based on Summing the Signal From Both Photodetectors.

PARAMETER	DEFINITION	DESCRIPTION
P4	((P1*948)/1000)-19	E_1, energy calibration from PMT 1, channel # = keV (in center)
P5	((P2*945)/1000)-13	E_2, energy calibration from PMT 2, channel # = keV (in center)
P6	(P4+P5)/2	E_1+E_2, used to find E_γ

Reading the binary data files also allowed for the investigation of the position resolution based on Equation 2-11. A redefinition of parameters was necessary as shown in Table 4-4. Again a scaling factor in P8 (multiplying by 500) and an offset in P7 (adding 2050) were necessary to ensure that the parameter remained positive and filled an adequate number of channels.

Table 4-4
Secondary Parameters for Investigation of the Position Response Based on Equation 2-11.

PARAMETER	DEFINITION	DESCRIPTION
P4	((P1*948)/1000)-19	E_1, energy calibration from PMT 1, channel # = keV (in center)
P5	((P2*945)/1000)-13	E_2, energy calibration from PMT 2, channel # = keV (in center)
P6	(P5+2050)-P4	E_2-E_1
P7	(P4+P5)/2	E_2+E_1; Energy in keV
P8	(P6*500)/P7	$(E_2-E_1)/(E_2+E_1)$; used to determine position

The mutiparameter data acquisition software, Multi, also allows the user to filter out data if any parameter falls outside a specified range of values [Plein 1993:15-16]. This feature allowed the selection of full-energy (photopeak) events by defining a "window" around the photopeak. Only coincident events which produced an energy signal within the boundaries of this window -- i.e. the photon deposited its full energy in the detector -- were included in the data. By discriminating these events, this procedure allowed the determination of position resolution as a function of energy while using polychromatic sources. It also allowed the determination of position and position resolution based on full-energy events. This type of

full-energy event selection is possible on an event-by-event basis in a Compton camera which is imaging one or more known isotopes emitting gamma rays of known energy. If the incident gamma-ray energy is unknown, it can be determined after the data is taken by locating a peak on the energy spectrum which results from summing the energy deposited in both detectors. The data can then be re-analyzed using only events which fall in that summed energy peak. The position resolution using the two techniques to determine position (Equation 2-5 and Equation 2-10) was reinvestigated using full-energy event discrimination to determine if an improvement in resolution resulted.

When directly measuring the position resolution of the second detector, a factor must be considered which makes the response differ from that of the same detector employed in a Compton camera system. During the measurement, the detector was exposed to a collimated beam of radiation which had a characteristic width. Because the position of interaction within the confines of this beam width was unknown, the width of the beam made the measured position resolution worse than the resolution which would have been obtained for interactions at a well-defined point. The width of the collimated radiation beam needed to be large enough to produce a high count rate, otherwise background events would have been significant and the signal-to-noise ratio unacceptable. Ideally, a very narrow collimated radiation beam could have produced an adequate count rate with little influence on position resolution if very active sources or long time periods were available. This was not the case for this project, so a wider beam was required. A description of the radiation collimation is needed, since the width of the collimated radiation beam degraded the measured position resolution.

Collimated Radiation Beam

The incident radiation was collimated by lead bricks with cylindrical holes. Figure 4-2 shows how the lead collimation was configured. The center of the collimation holes was positioned at the center of the crystal in the y-direction of and at the desired x-position. The coordinate axes are illustrated in Figure 4-2.

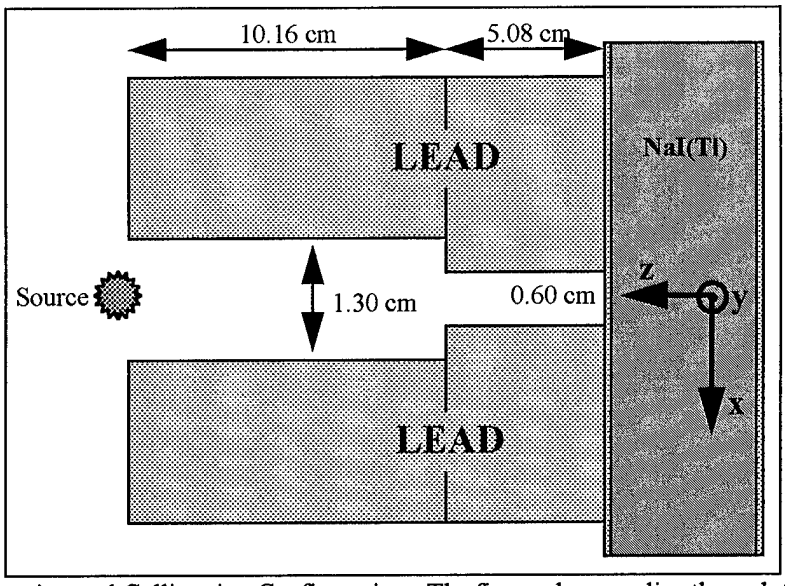

Figure 4-2. Experimental Collimation Configuration. The figure shows a slice through the x-z plane at y=0.

A "Mathematica" notebook was written [Appendix B] which calculates the intensity of the incident radiation as a function of the gamma-ray energy and distance from the center of the radiation beam. Two examples of output are in Figure 4-3 and Figure 4-4 which show the collimation intensity with position for two energies in the range of interest, 3000 keV and 662 keV. The intensity of the collimated beam when it had passed through half of the detector depth is shown. As illustrated in Figure 4-2, the x axis represents distance along the lengthwise dimension of the crystal, the y axis represents distance along the smallest dimension (height) of the crystal. The origin represents the center of the collimated beam and the z axis is the intensity at position (x,y) normalized to the full, unattenuated intensity. Comparison of Figure 4-3 and Figure 4-4 reveals that the intensity at higher energies falls off less rapidly with distance from the beam center. This is occurs because the small amount of lead through which gammas pass near the edges of the beam does a more effective job of stopping the low energy gammas.

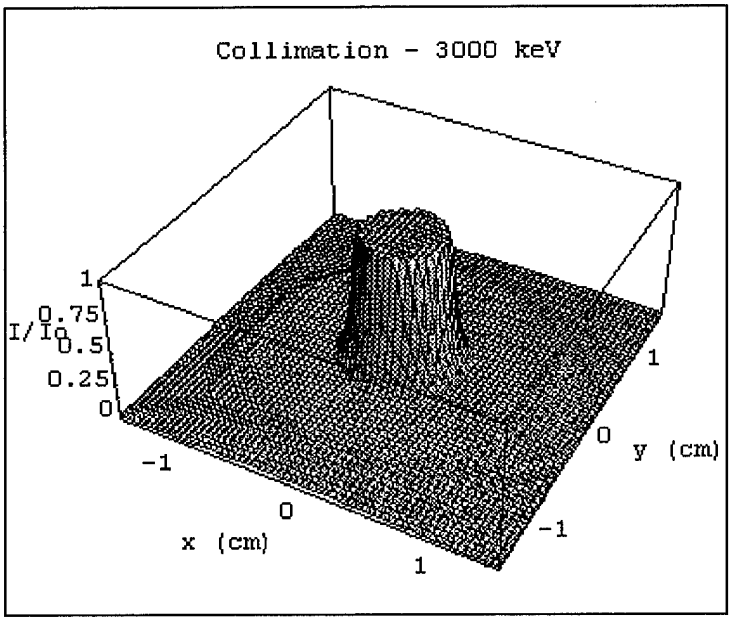

Figure 4-3. Radiation Intensity (relative to full intensity) as a Function of Distance (in cm) From the Center of Collimation Beam a Gamma-Ray Energy of 3000keV.

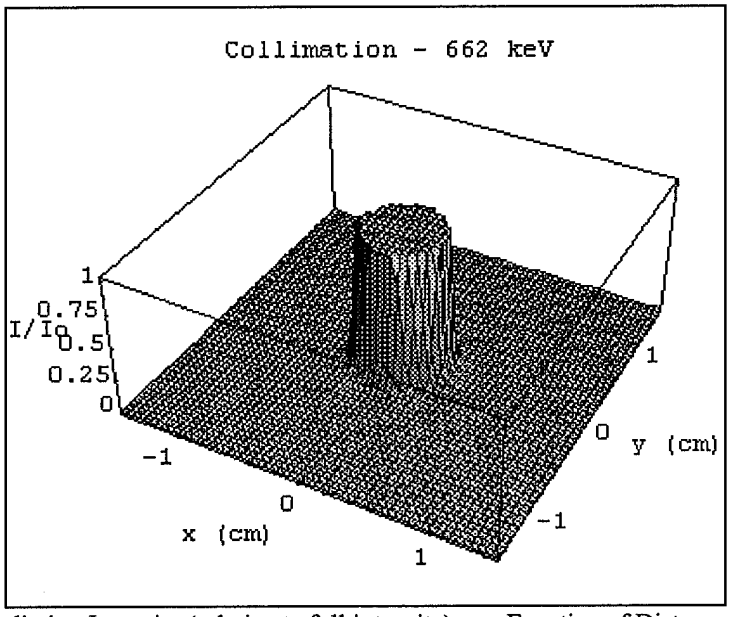

Figure 4-4. Radiation Intensity (relative to full intensity) as a Function of Distance (in cm) From the Center of Collimation Beam at a Gamma-Ray Energy of 662 keV

Because the detector measures the position of interaction in the x-direction, the total intensity illuminating the crystal as a function of x was determined. This was accomplished by integrating the intensity over y for all positions in x. The dimensions of the crystal in the y-direction provided the limits of integration on y. In other words, if the total intensity at position x is defined as $I_{tot}(x)$, then

$$I_{tot}(x) = \int_{y\,\min}^{y\,\max} I(x,y)dy \qquad \text{(Equation 4-1)}$$

With the symmetric collimation used here, $I_{tot}(x)$ had maximum value at x=0, the center of the collimation beam, and equal values at the same distance on either side so $I_{tot}(x)=I_{tot}(-x)$. Figure 4-5 shows how $I_{tot}(x)$ varied with x at an energy of 835 keV. Here the values of $I_{tot}(x)$ have been normalized so that $I_{tot}(0)=1$.

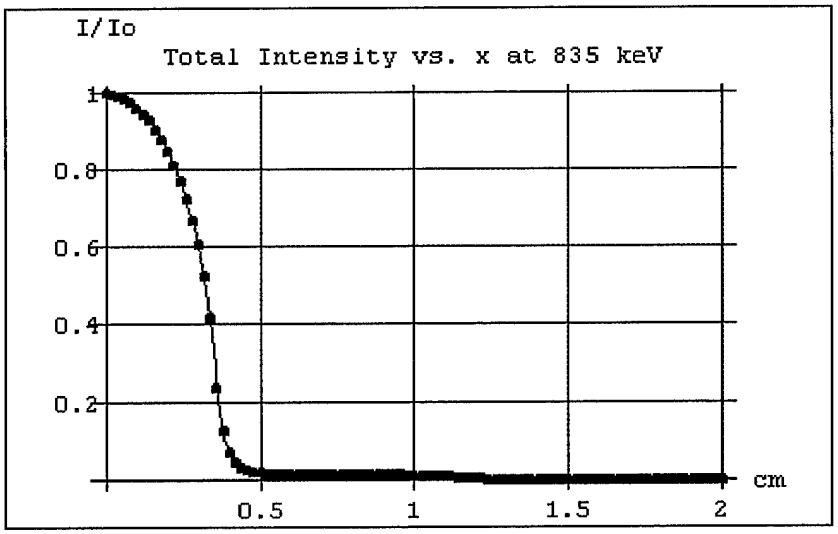

Figure 4-5. $I_{tot}(x)$ as a Function of x (in cm) For a Gamma-Ray Energy of 835 keV. The data points represent calculated data, the solid line is an interpolating function.

To characterize the width of the collimated radiation beam, the value of x at which the normalized $I_{tot}(x)$ function fell to 1/2 was taken to be the HWHM of the radiation beam. Figure 4-6 shows how the FWHM of the radiation beam varied with energy. The width was calculated at a point half way through the depth of the crystal. A piecewise polynomial function has been fitted to the data points computed with the Mathematica notebook and is also shown in Figure 4-6. This fitted function was used later to interpolate values at intermediate energies.

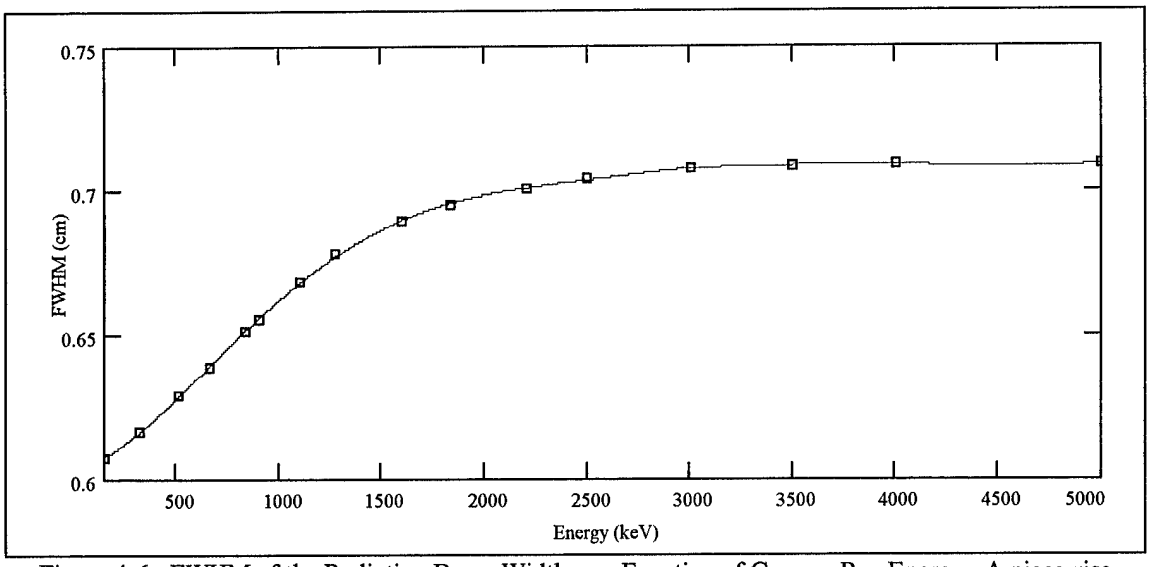

Figure 4-6. FWHM of the Radiation Beam Width as a Function of Gamma Ray Energy. A piecewise polynomial fit to the data points is shown.

For comparison with the measured data, the FWHM of the beam width was added in quadrature to the FWHM position resolution which would be obtained from interactions at a well-defined point. The position and energy resolution obtained from interactions at a well-defined point was derived from the analytical model using parameters calculated from the DETECT simulation.

Modeling of Position-Sensitive Detector with DETECT

The primary purpose of the DETECT simulation was to provide modeled values of the light attenuation coefficient α and the photoelectron probability component P_{pmt}. These values were then used in Carter's relations (Equation 2-7 and Equation 2-8) to predict the detector's energy and position resolution for comparison to the measured values.

The geometry of the components, their optical properties, and surface characteristics were all defined in the DETECT input file. The surface of the NaI(Tl) crystal was sanded by the manufacturer, so the surface of the modeled NaI(Tl) crystal is defined as a roughened optical surface. An external diffuse reflector was modeled surrounding the crystal which had a reflectivity of 85 percent the reflectivity of magnesium oxide (this figure was provided by the manufacturer). The use of a single reflection coefficient is justified because the reflectivity of MgO remains fairly constant over the wavelengths of the

scintillation photons [Kortum 1969:146]. A small air gap was modeled between the surface of the crystal and the external diffuse reflector. This addition was necessary because the mismatch in the indices of refraction between the crystal and the small amount of air trapped between the crystal and the reflector is responsible for a significant amount of internal reflection. The two Pyrex optical windows between the end of the crystal and the PMT were included in the model because the index of refraction mismatch also contributes to some internal reflection. An optical coupling fluid between the Pyrex optical windows and the PMTs reduces internal reflection at that interface. One photodetector was modeled at one end of the apparatus. The number of photons collected by the photodetector at the other end was taken to be the number collected by the modeled photodetector when the interaction took place at the same distance from the modeled photodetector. In other words, if N_1 is the number of photons collected by one photodetector, N_2 is the number of photons collected by the other photodetector, L is the length of the crystal and x is the distance of the interaction from the end of the crystal nearest the photodetector which collects N_1 photons, then

$$N_2(x) = N_1(L - x)$$

DETECT allows the user to define a three-dimensional "box" in which all the scintillation photons are homogeneously distributed in space and isotropically distributed in direction. In the model, the box was a cube whose dimensions were the range of the photoelectron which generated the scintillation photons in the NaI(Tl) crystal. The energy of this photoelectron is simply the energy of the incident gamma less the binding energy of an iodine K-shell electron, 33.17 keV [Lide 1992:10-280]. The iodine atoms from which photoelectrons are dislodged emit x-rays as electrons fill vacancies in the K-shell. If the iodine K-x-ray doesn't escape the detector, then the total energy of the incident photon is deposited. The range of the photoelectrons in sodium iodide was taken from published data [Pages 1972:79]. The box dimensions versus incident gamma ray energy are shown in Figure 4-7. A second-order polynomial fit to the data is also plotted in the figure.

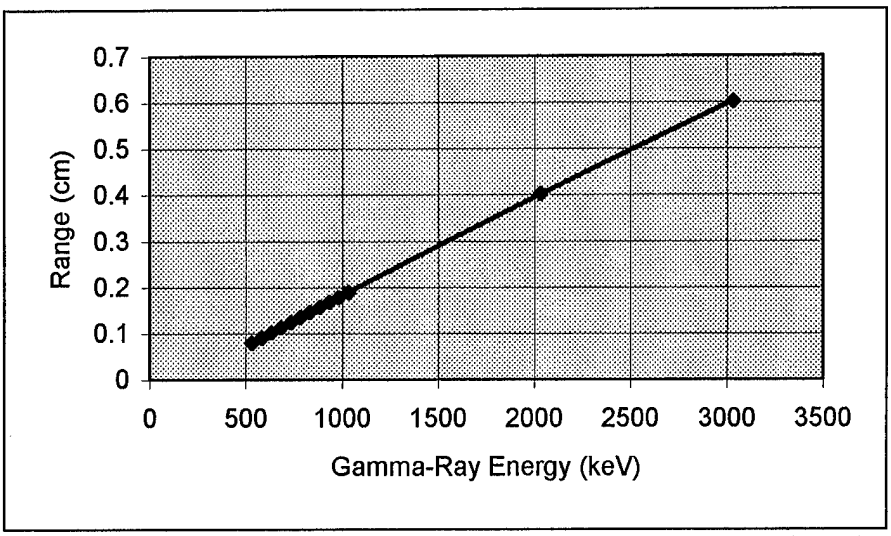

Figure 4-7. Range of Photoelectrons in NaI(Tl) vs. Gamma-Ray Energy. The range is used to determine the dimensions of the volume in which the scintillation photons will be generated during the simulation.

The number of photons produced in the scintillator per keV deposited (light yield) was needed to complete the model. Based on a study of the light yield of NaI(Tl) at gamma-ray energies of 511 keV, 835 keV, 890 keV, 1116 keV, 1274 keV, and 1836 keV [Holl 1988] an average light yield of 37.7 photons per keV deposited in NaI(Tl) was used. The response varies by about 3 percent over the energy range of interest [Knoll 1989:230-231]. The same study found an average of 51.8 photons per keV deposited in CsI(Tl) [Holl 1988]. These figures were used in the model. Any nonlinearity of light output with respect to energy deposited could be accounted for in the input file by generating the appropriate number of scintillation photons. Appendix A shows a sample input file used for the DETECT model.

The response of the PMT tube was assumed to be linear with the number of photons collected, so the ratio of the photons collected at either end was equal to the ratio of the signal at either end (E_2/E_1), and was used to determine the position. From Equation 2-5, if the natural logarithm of the ratio is plotted vs. position, the slope of the line will be 2α. The light attenuation per unit length, α, was determined from the slope of a line fitted through a curve of $\ln(E_2/E_1)$ versus position.

Another parameter P, the probability that a photon generated at one end will produce a photoelectron in the PMT, was needed to determine the position and energy resolution as defined by

Carter's relations, Equations 2-7 and 2-8. P will be referred to as the photoelectron probability. P was taken to be the product of two probabilities.

$$P = P_{pmt}\varepsilon_{quant} \qquad \text{(Equation 4-2)}$$

where P_{pmt} is the probability that a photon generated at one end will be collected by the PMT photocathode, and ε_{quant} is the quantum efficiency of the PMT photocathode. P_{pmt} was determined by generating 500 photons evenly distributed in the modeled crystal adjacent to the PMT tube. The ratio of the number collected to the number generated was taken to be P_{pmt}. The mean value of 10 trials was used to get a value for P_{pmt} of 0.526. The value of ε_{quant} was calculated from data provided by the manufacturer.

The quantum efficiency of a PMT photocathode -- the probability that an incident photon will generate a photoelectron -- is a function of the incident photon wavelength. The PMT manufacturer, Hamamatsu, reports the radiant sensitivity of the bialkali photocathode in the R1306 PMT as a function of incident photon wavelength. The radiant sensitivity has units of mA/W. If $S(\lambda)$ is the radiant sensitivity in mA/W at the wavelength λ in nm, then $\varepsilon_{quant}(\lambda)$ is obtained by Equation 4-3 [Hamamatsu 1990:7].

$$\varepsilon_{quant}(\lambda) = \frac{S(\lambda) \cdot 1.240}{\lambda} \qquad \text{(Equation 4-3)}$$

The NaI(Tl) crystal will produce scintillation photons whose spectral intensity (relative intensity) is a function of photon wavelength. Figure 4-8 shows the spectral intensity $I_{sp}(\lambda)$ of the NaI(Tl) scintillation photons relative to the intensity at the wavelength of maximum emission (415 nm) [Knoll 1989:230]. The figure also shows the quantum efficiency of the PMT photocathode [Hamamatsu 1990:70] as a function of λ in nm.

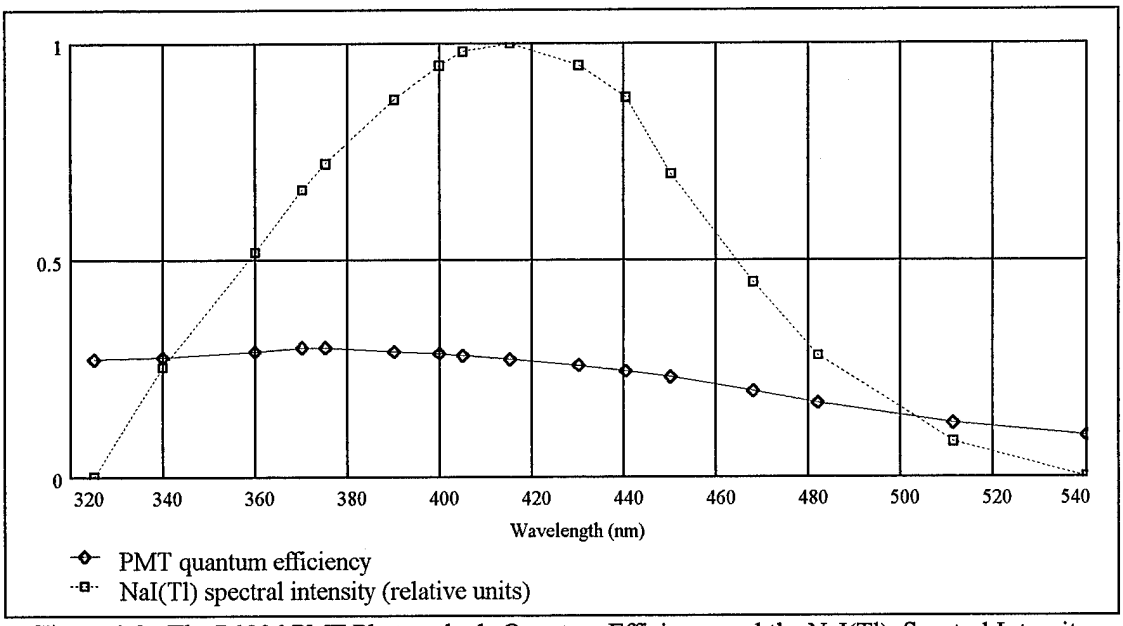

Figure 4-8. The R1306 PMT Photocathode Quantum Efficiency and the NaI(Tl) Spectral Intensity (relative units) as a Function of Photon Wavelength.

The integration shown in Equation 4-4 was performed to calculate a total value of ε_{quant}.

$$\varepsilon_{quant} = \frac{\int_{320nm}^{540nm} \varepsilon_{quant}(\lambda) I_{sp}(\lambda) d\lambda}{\int_{320nm}^{540nm} I_{sp}(\lambda) d\lambda} \qquad \text{(Equation 4-4)}$$

As a result, the quantum efficiency was determined to be $\varepsilon_{quant} = 0.256$. Multiplying P_{pmt} by ε_{quant} gives a total value for the photoelectron probability of P = 0.135.

The values for ε_{quant} and P_{pmt} for a similar sized CsI(Tl) scintillation crystal coupled to HgI_2 photodiodes needed to be determined to predict the response of the hypothetical second detector element with these components. Figure 4-9 shows the relative spectral intensity of CsI [Valentine 1993:44] and the quantum efficiency of a large-area HgI_2 photodiode with salt water entrance windows [Markakis 1985] plotted versus wavelength.

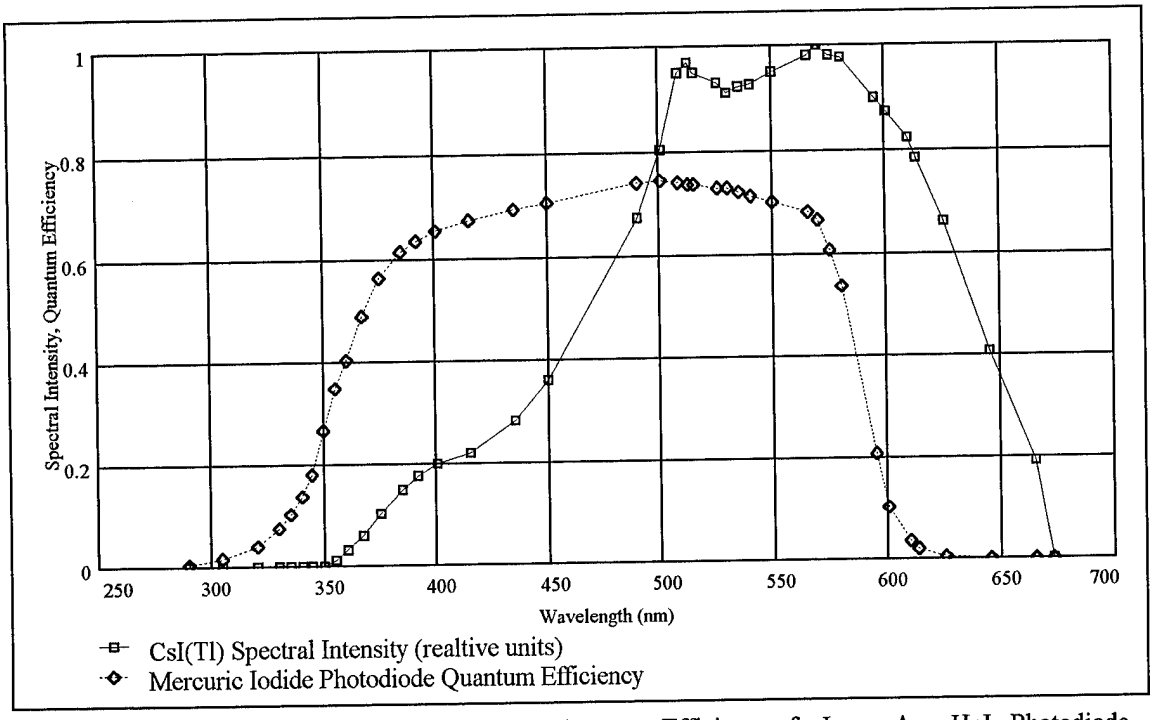

Figure 4-9. The Spectral Intensity of CsI(Tl) and Quantum Efficiency of a Large-Area HgI_2 Photodiode as a Function of Photon Wavelength.

These curves were then integrated from 295 nm to 673 nm as in Equation 4-4 resulting in a calculated quantum efficiency of 0.519. The value of P_{pmt} was calculated from 10 trials to be 0.557 in the hypothetical second detector. Therefore the value of the photoelectron probability for the hypothetical second detector element was modeled as P = 0.289.

The values of α and P which were derived as described above were then used in Carter's equations to predict the position and energy resolution of the actual (NaI(Tl)) and hypothetical (CsI(Tl)) position-sensitive detectors. These resolutions are needed to calculate the angular resolution of the Compton camera system. Also needed is the energy resolution which is obtained by summing the energies deposited in both detectors.

Collecting Summed Energy Spectra

To record summed energy spectra, it was necessary to record the energy deposited in each detector by events which Compton scattered from the first detector and into the second detector. To do so, the signal processing system was configured according to Figure 3-6.

To sum the energies deposited in both detectors, it was first necessary to calibrate the energy signals from both detectors so that like units could be added. The first detector was calibrated as before by first recording the pulse height spectra at each end from various gamma-ray energies incident on the center of the detector and then scaling them so that the channel number corresponded to the recorded energy. The results of this calibration were parameters P5 and P6 which are defined in Table 4-5. The first detector was calibrated using the isotopes of ^{133}Ba (356 keV, 302 keV and 207 keV (Compton edge), and ^{57}Co (122 keV). Again the channel number was made to correspond to the energy deposited in the detector. The result of this calibration was assigned to parameter P7 and is defined in Table 4-5. P8 was then defined as the event-by-event sum of the two energies, P6+P7.

Table 4-5
Parameters for Coincident Spectroscopy.

PARAMETER	DEFINITION	DESCRIPTION
P1	P1	Signal from first detector
P2	P2	Signal from PMT 1
P3	P3	Signal from PMT 2
P4	P4	Timing signal
P5	((P2*979)/1000)+((P3*880)/1000)-182	Sum of energy signals from both PMTs
P6	P5/2	Energy deposited in second detector (E_{γ}') keV
P7	((P1*466)/1000)-65	Energy deposited in first detector (E_{re}) keV
P8	P6+P7	Summed energies (E_{γ}) keV

The two detectors were positioned relative to each other as they would be in the proposed system. The second detector was positioned as one element of the octagonal ring. The first detector was positioned on the octagonal ring axis so that the central scattering angle into the second detector was 60 degrees. This central scattering angle corresponded to the angle of scatter for a gamma ray incident along the ring axis which scattered from the center of the first detector and into the center of the second detector at positions of 10 cm and 20 cm along the detector length. An alternative view is that 60 degrees is the central scattering angle which would result from a truly ring-shaped second detector of radius 24.65 cm. A ring of this radius would intercept the center of the detector elements at positions of 10 cm and 20 cm.

The first detector was illuminated by a ^{54}Mn source (835 keV) and then a ^{22}Na source (511 keV, 1275 keV) which were positioned along the second detector axis at a distance of 1.1 cm. The summed energy spectra were then analyzed to determine the locations of the centroids. The error in locating the centroid of the summed energy peaks was used in the angular resolution calculations. The system efficiency at 835 keV was also determined. Figure 4-9 shows a summed energy spectrum collected from ^{54}Mn. The low-energy tail on the peak was caused by events in which the full recoil electron energy E_{re} was not deposited in the first detector or the full scattered photon energy E_γ was not deposited in the second detector. In either case the sum of the two deposited energies was not the incident energy E_γ, so an erroneous energy was recorded.

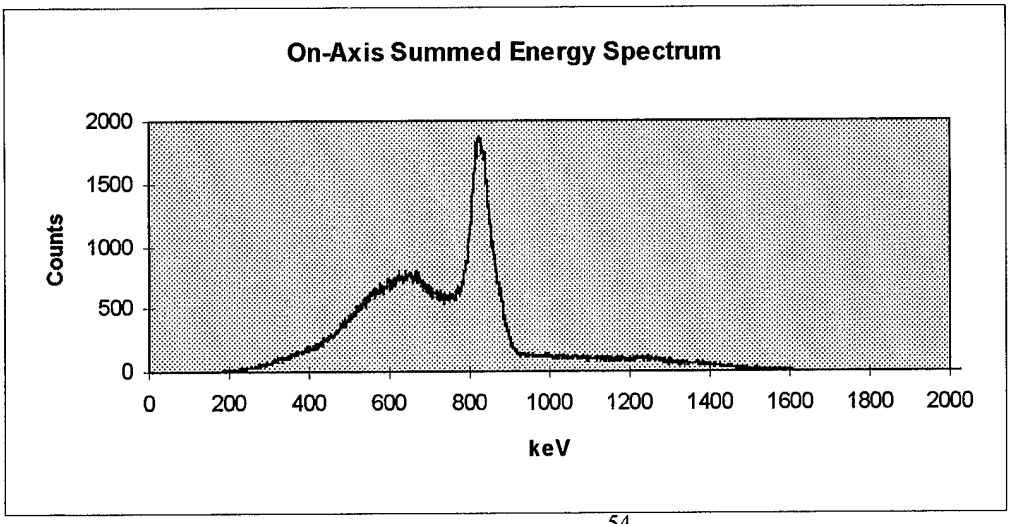

Figure 4-9. Summed Energy Spectrum From ^{54}Mn on the Central Axis.

The ^{54}Mn source was then displaced from the central axis by 44 degrees so that the scattering angle into the second detector was 104 degrees. Another summed energy spectrum from ^{54}Mn was collected in this configuration. A ^{137}Cs source was placed on the central axis to investigate the system efficiency at 662 keV.

V. RESULTS

This chapter presents the results of modeled detector characteristics and compares them with measured data. The angular resolution of the Compton camera is developed using both the existing NaI(Tl)-PMT and hypothetical CsI(Tl)-HgI_2 position-sensitive scintillators. In addition, the efficiency model is evaluted for the proposed system and characteristics of summed energy spectra are discussed.

Energy Resolution of the First Detector Element

It is important to characterize energy resolution in the first detector element because it will affect the angular resolution of the Compton camera system by causing uncertainty in the direction of the Compton scatter and the interaction cone angle. It also affects the energy resolution of the system as a whole.

Figure 5-1 shows energy resolutions measured at three different energies. The figure illustrates that no energy dependence of the resolution is discernible, and that the energy resolution remains generally constant over the energy range studied. This results from the dominance of electronic noise over signal in the energy resolution, which is a property typical of room-temperature semiconductor detectors. One expects the absolute energy resolution to get worse with increasing energy, however the uncertainty introduced by the electronic noise in this detector outweighs the statistical uncertainty at the energies studied. Therefore, no appreciable degradation in absolute energy resolution was observed. An average value of the three resolutions measured is plotted in Figure 5-1. This average value of 34.8 keV FWHM will be used in this project to describe the energy resolution of the first detector element. Once the first detector energy resolution was established, the characteristics of the first detector element which were required to predict the Compton camera performance were known. Modeling the characteristics of the second detector element began with modeling the light attenuation through the scintillator.

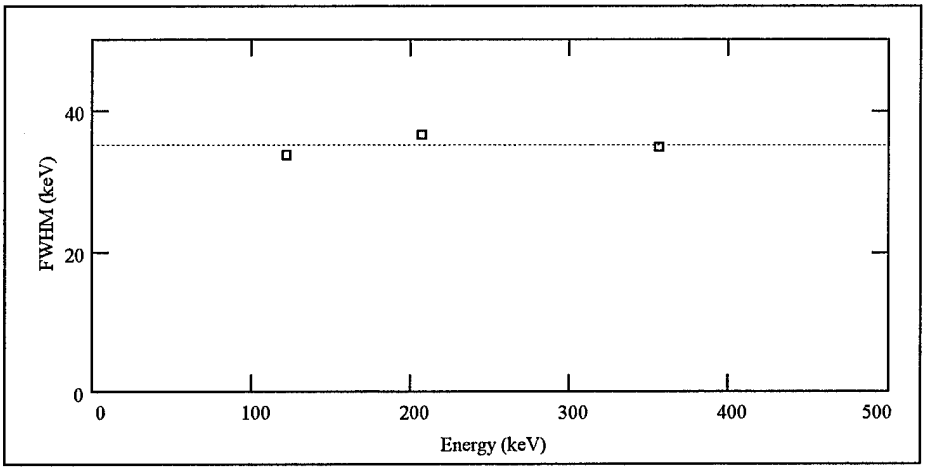

Figure 5-1. Measured Energy Resolutions of the First Detector Element vs. Energy. An average value of 34.8 keV is also plotted.

Light Attenuation in Second Detector Element

The light attenuation through the position-sensitive scintillator can be modeled as a simple exponential function, a linear function, or the Kubelka-Munk function as described in Chapter II.

Figure 5-2 shows how the Kubelka-Munk model describes the attenuation through the detector. The results of a DETECT Monte-Carlo simulation are plotted as data points. The data points are the number of photons collected at one end of the detector versus the distance x from that end of the crystal. The data is normalized by the number of photons collected at x = 3 cm. The best fit of the Kubelka-Munk attenuation model to the data points is plotted as a solid line. The best fit of the exponential attenuation model to the data points is plotted as a dotted line. A linear fit to the data points is also shown. The sum of the squares of the errors in the exponential fit is 1.73 times greater than that of the Kubelka-Munk fit. The Kubelka-Munk model may work better because it is based on more rigorous physical principles or simply because two parameters are fitted, providing an extra degree of freedom.

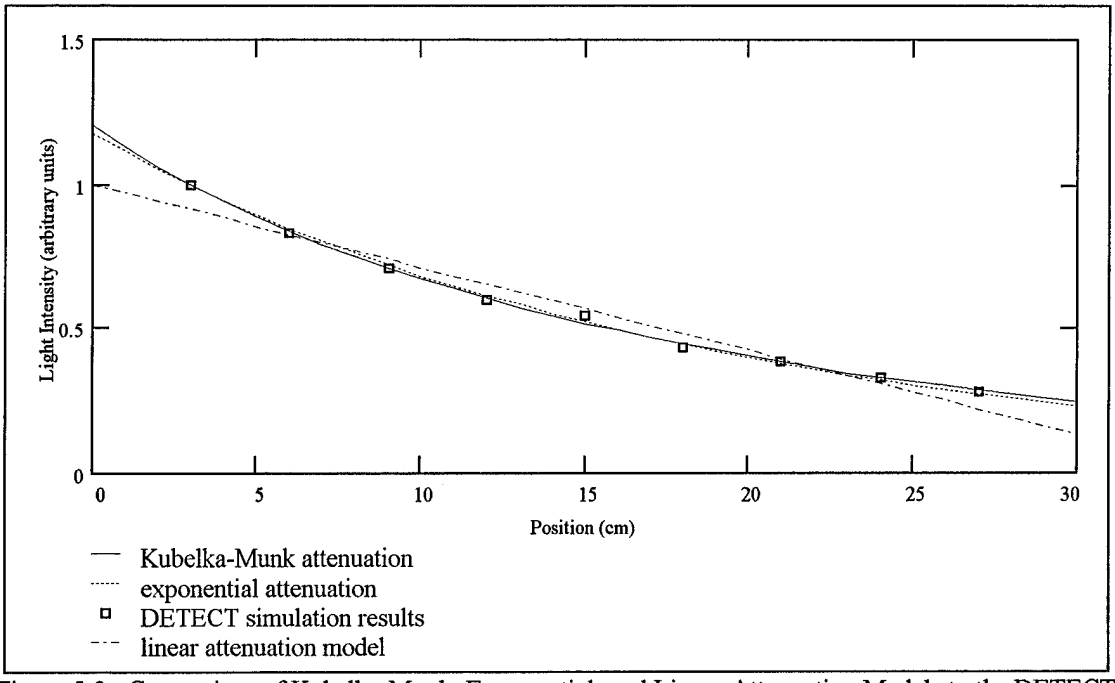

Figure 5-2. Comparison of Kubelka-Munk, Exponential, and Linear Attenuation Models to the DETECT Simulation Data Points.

The purpose of the model was to predict the response of the actual detector, so it was worthwhile to compare the attenuation models to actual detector measurements. Figure 5-3 compares the three attenuation models against the measured attenuation. The measured data are plotted as data points. The data points are the pulse heights from one PMT versus the distance of interaction x from that end of the crystal. The data is normalized by the pulse height recorded at x = 3 cm. The Kubelka-Munk attenuation, exponential attenuation, and linear attenuation as derived from the results of a DETECT simulation are plotted as a lines. Because the eventual goal is to model the light attenuation in a detector based only on DETECT simulations, it is more useful to investigate which attenuation model from the DETECT simulation most closely matches the measred attenuation than to simply investigate which model most closely fits the measured data.

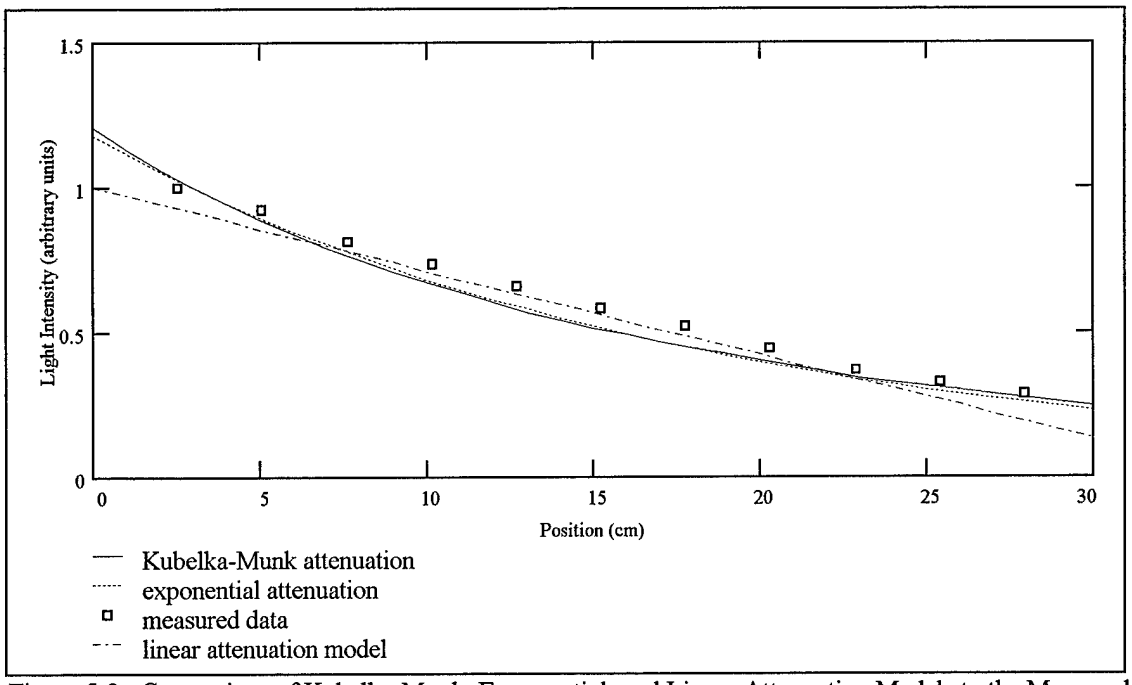

Figure 5-3. Comparison of Kubelka-Munk, Exponential, and Linear Attenuation Models to the Measured Data Points.

In the case of the measured data, the smallest error is obtained from the exponential model, although the error for the linear model is nearly identical. Table 5-1 lists the sum of the squares of the errors between the model and data points for the three attenuation models applied to both the DETECT data and measured data.

Table 5-1
Sum of the Squares of The Errors Between Three Attenuation Models and DETECT and Measured Data.

Attenuation Model	Error From DETECT Data	Error From Measured Data
Kubelka-Munk	0.000734	0.0301
Exponential	0.00127	0.0269
Linear	0.0198	0.0287

Although Kubelka-Munk theory better parameterizes the results of the DETECT simulation, the exponential and linear attenuation models do a better job of mapping the results of the DETECT simulation to the response of the actual detector. This result is fortunate because extracting position and energy information from Equation 2-12 leads to a transcentendal system of equations. The exponential model was applied to parameterize the results of the DETECT simulation for a value of α.

Position Calibration of Second Detector Element

The position calibration of the second detector element was accomplished to establish that the modeled response of the detector, as predicted by the DETECT program, agreed with the measured response. It was also necessary to calculate a value for the light attenuation coefficient α which will be an important parameter in the model of position and energy resolution.

The position of interaction in a position-sensitive scintillator can be determined by Equation 2-5, which can be arranged to give $\ln(E_2/E_1)$ as a function of x.

$$\ln\left[\frac{E_2}{E_1}\right] = 2\alpha x - \alpha L$$

plotting $\ln(E_2/E_1)$ versus x should yield a straight line with a slope of 2α.

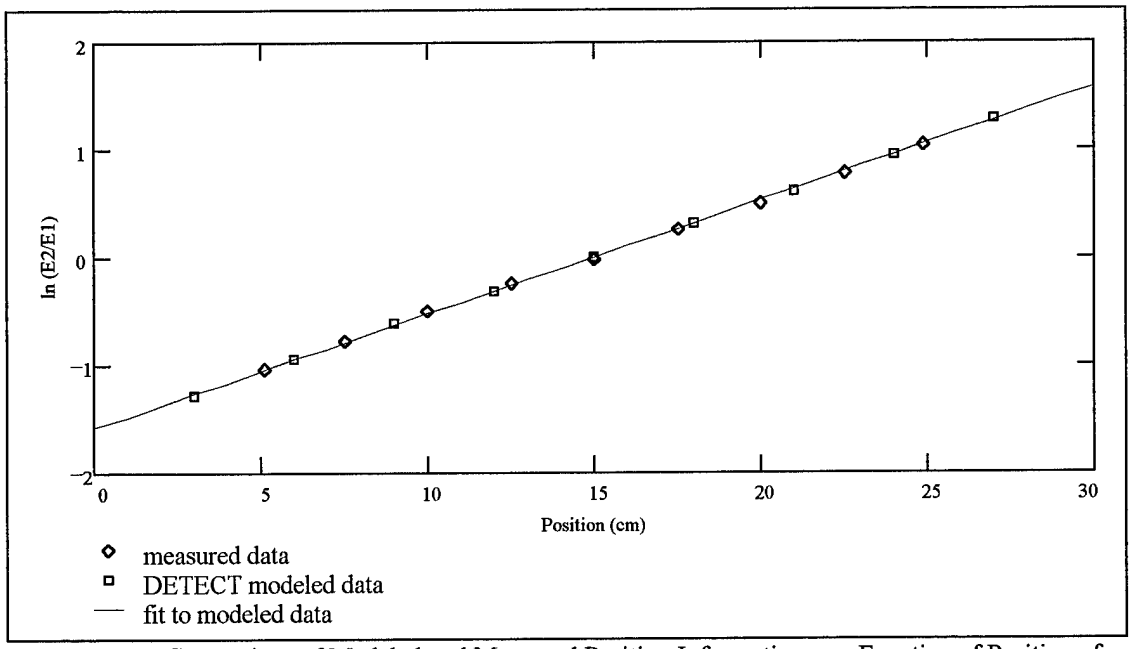

Figure 5-4. Comparison of Modeled and Measured Position Information as a Function of Position of Incident Radiation. A linear least-squares fit to the modeled data is also shown.

Figure 5-4 shows both the results of the DETECT computer simulation and the measured response of the detector. In the case of the DETECT results, the natural log of the ratio of the simulated photons collected at each end is plotted on the y-axis. In the case of the measured response of the detector, the natural log of the ratio of PMT signal amplitudes is plotted on the y-axis. A linear least-

squares fit was applied to the modeled data and is also shown in Figure 5-4. The modeled and measured data are in reasonable agreement along the length of the detector, which suggests that DETECT was satisfactorily modeling the light attenuation in the detector. The slope of the linear fit to the modeled data is 0.1055 so $\alpha = 0.05275$. This is the value of the light attenuation coefficient per unit length α which was used to model the position and energy resolution of the position-sensitive detector.

Energy Resolution of Second Detector Element

Two techniques for determining the energy deposited in the second detector element were described in Chapters II and IV:

1) $E_{dep} \propto \sqrt{E_1 \cdot E_2}$ (Equation 5-1)

2) $E_{dep} \propto (E_1 + E_2)$ (Equation 5-2)

Figure 5-5 shows the energy resolutions in relative FWHM as a function of position along the detector which were obtained using both techniques. The values shown were derived from energy spectra taken when the detector was illuminated with collimated radiation from ^{54}Mn which has a single gamma-ray line at 834.8 keV. Also shown is the modeled energy resolution based on Equation 2-8 with a value of α obtained above, an E_γ of 834.8 KeV, an E_0 of 37.7 photons per keV deposited [Holl 1988] and the photoelectron probability described in Chapter IV. The model correctly predicts the variation of the energy resolution with x, but incorrectly predicts the magnitude. Energy specta obtained by taking the sum of the signals from both ends of the PMT tubes as in Equation 5-2 exhibited a better resolution and more closely matched the modeled resolution as a function of position than did the spectra obtained by taking the square root of the product of the signals as in Equation 5-1.

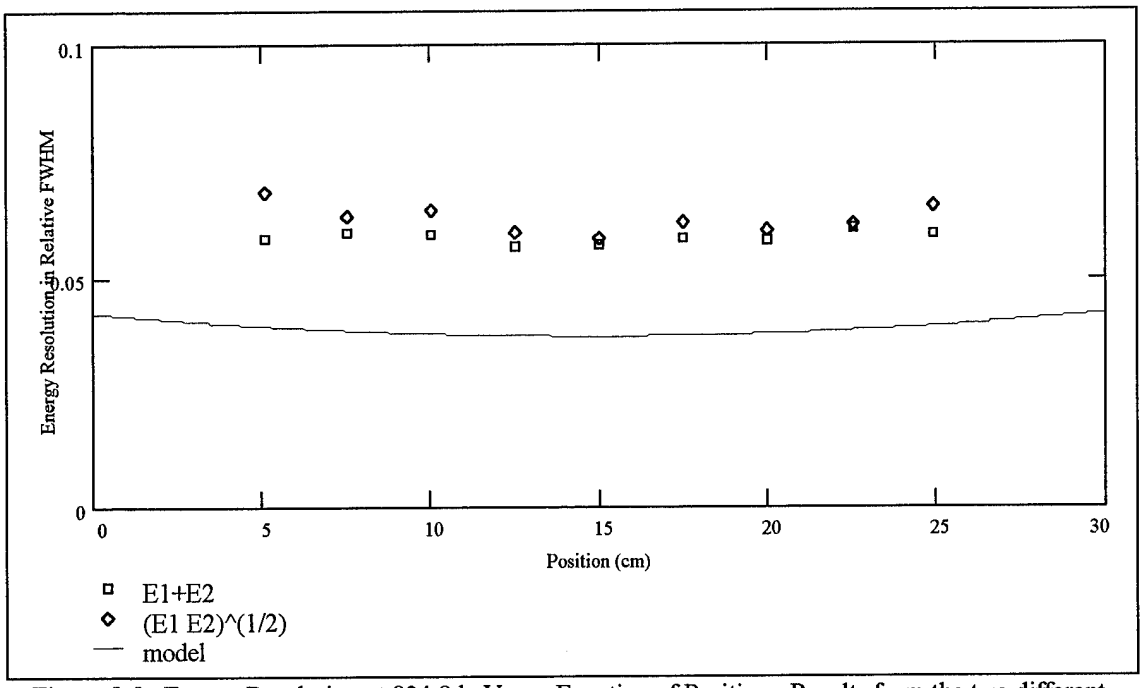

Figure 5-5. Energy Resolution at 834.8 keV as a Function of Position. Results from the two different spectroscopy techniques are shown as is the energy resolution predicted by the model.

Another positive characteristic of using the sum of the two PMT signals for spectroscopy (Equation 5-2) is that the recorded photopeak energy varied less with position than it did when the square root of the product (Equation 5-1) was used. Less variation in the recorded energy will improve the energy resolution of the Compton camera where events will be measured over the length of the detector. Figure 5-6 shows the percent difference between the recorded energy of the 834.8 keV photopeak at position x and the recorded energy of the 834.8 keV photopeak at the center of the detector (15 cm) for both techniques.

In order to characterize the difference between the modeled and measured position resolutions, the modeled energy resolution was averaged over the values of x to remove the x dependence according to Equation 5-3. This made the average modeled energy resolution ΔE_{mod} a function of energy only. Likewise an average measured energy resolution ΔE_{mes} was determined according to Equation 5-4.

$$\Delta E_{\mathrm{mod}}\left(E_\gamma\right) = \frac{\int_{5cm}^{25cm} \frac{2.35 \cdot e^{\alpha L/4}}{2} \sqrt{\frac{e^{\alpha\left(x-\frac{L}{2}\right)} + e^{-\alpha\left(x-\frac{L}{2}\right)}}{E_\gamma P / E_o}}\, dx}{\int_{5cm}^{25cm} dx} \qquad \text{(Equation 5-3)}$$

$$\Delta E_{mes}\left(E_\gamma\right) = \frac{\sum_{i=1}^{9} \delta E\left(E_\gamma\right)_i}{9} \qquad \text{(Equation 5-4)}$$

where the $\delta E(E_\gamma)_i$ represent the relative FWHM energy resolutions at energy E_γ measured at the nine positions studied along the length of the detector. If the ratio of $\Delta E_{mes}/\ \Delta E_{mod}$ is then designated as K_E, it can be applied as a correction to the modeled energy resolution to bring it into closer agreement with the measured data.

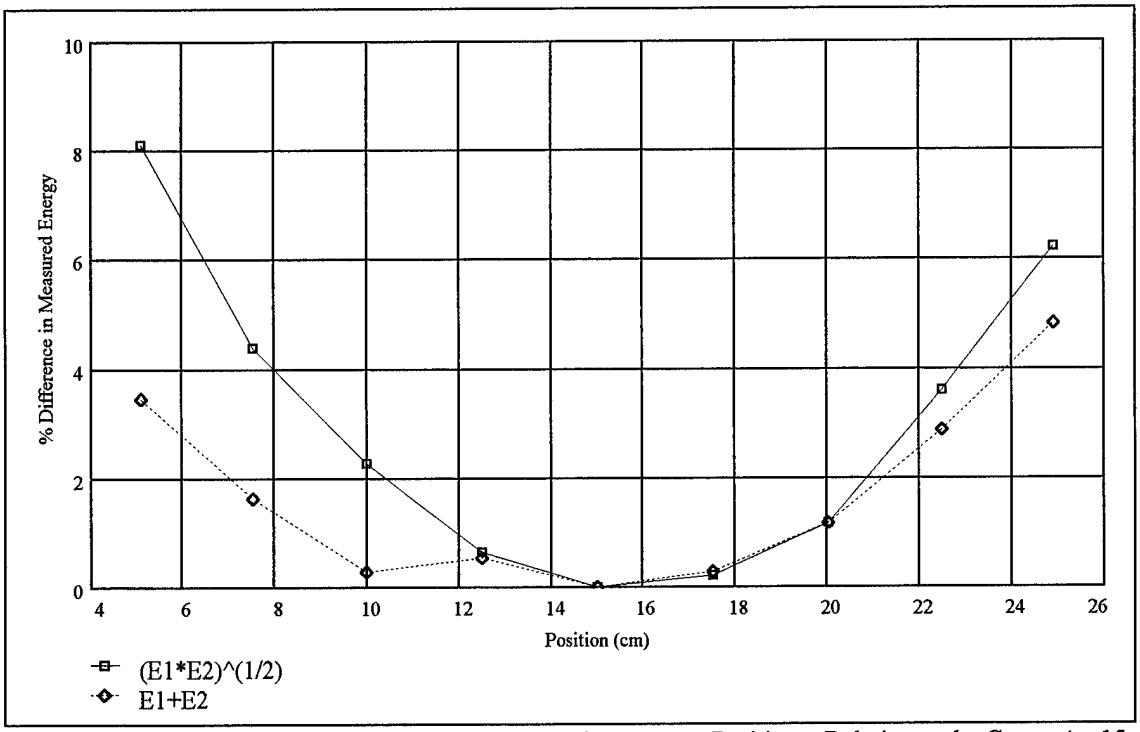

Figure 5-6. Percent Difference in Measured Photopeak Energy at Position x Relative to the Center (x=15 cm) for Both Spectroscopy Techniques.

$$\sigma_E\left(x, E_\gamma\right) = K_E \frac{2.35 \cdot e^{\alpha L/4}}{2} \sqrt{\frac{e^{\alpha\left(x-\frac{L}{2}\right)} + e^{-\alpha\left(x-\frac{L}{2}\right)}}{E_\gamma P / E_o}} \qquad \text{(Equation 5-5)}$$

The value of K_E which was found to minimize the error between the average modeled energy resolution ΔE_{mod} and the average measured energy resolution ΔE_{mes} was $K_E = 1.605$. Figure 5-7 shows how multiplying the modeled energy resolution by K_E (corrected model) brings it into closer agreement with the measured data at an incident energy of 834.8 keV.

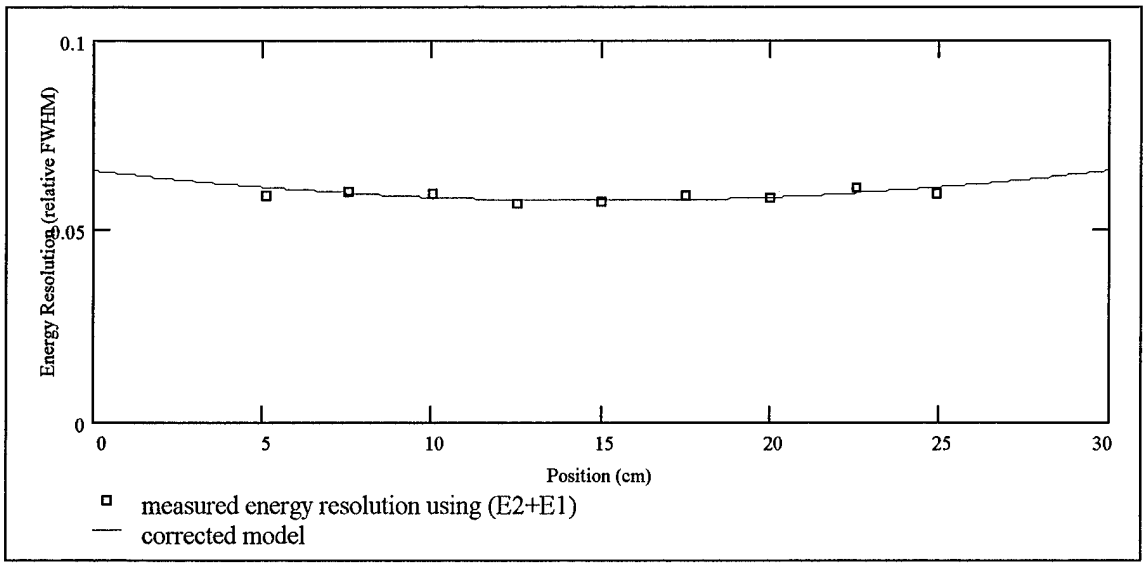

Figure 5-7. Measured Energy Resolution at 834.8 keV and Corrected Model Energy Resolution as a Function of x.

The energy resolution should improve as the gamma-ray energy increases. Figure 5-8 shows the measured average energy resolution ΔE_{mes} a function of energy. Also shown in Figure 5-8 is the modeled energy resolution corrected by the factor K_E. The corrected model is in general agreement with the measured energy resolutions across the energy range studied.

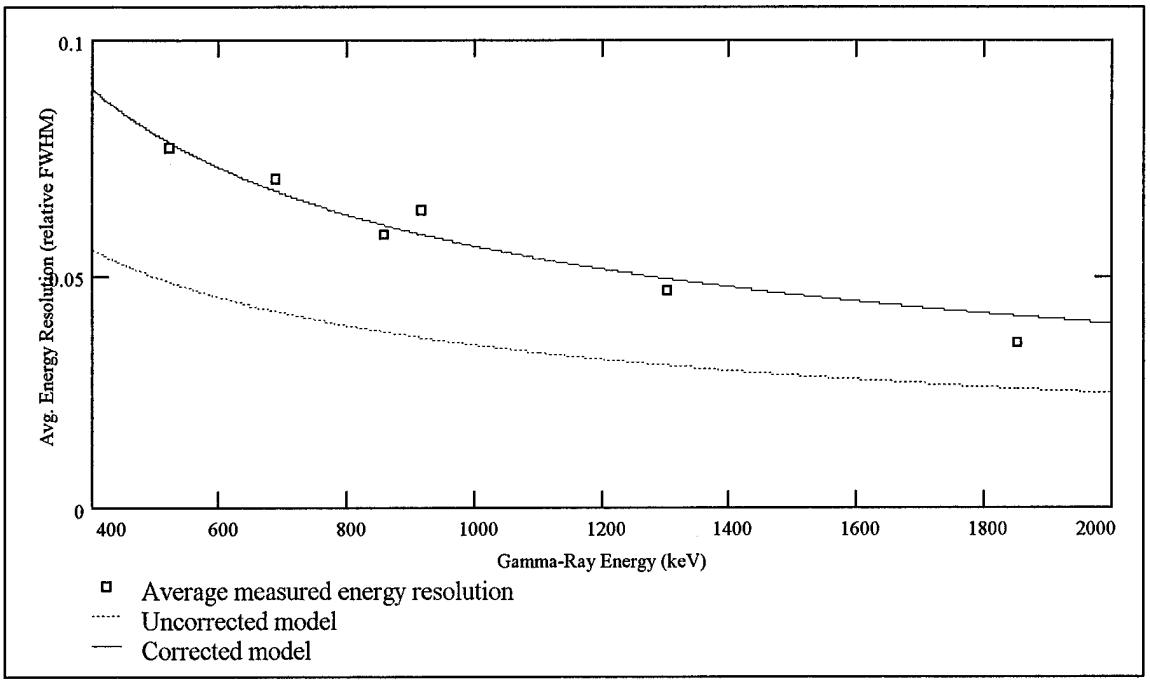

Figure 5-8. Average Measured Energy Resolution and Average Corrected Modeled Energy Resolution. $K_E = 1.605$

Position Resolution of the Second Detector Element

The following four techniques for determining the position of interaction in the detector were investigated.

$$x \propto \ln\left(\frac{E_2}{E_1}\right) \text{ without full-energy photopeak event selection} \qquad \text{(Equation 5-6)}$$

$$x \propto \ln\left(\frac{E_2}{E_1}\right) \text{ with full-energy photopeak event selection} \qquad \text{(Equation 5-7)}$$

$$x \propto \frac{(E_2 - E_1)}{E_\gamma} \text{ without full-energy photopeak event selection} \qquad \text{(Equation 5-8)}$$

$$x \propto (E_2 - E_1) \text{ with full-energy photopeak event selection} \qquad \text{(Equation 5-9)}$$

Figure 5-9 shows the position resolutions in centimeters FWHM as a function of position along the detector which were obtained using three of the four techniques. The values shown were derived from position spectra taken when the detector was illuminated with collimated radiation from ^{54}Mn which

emits a single gamma-ray line at 834.8 keV. Also shown is the modeled position resolution based on Equation 2-7 with a value of α obtained above, an E_γ of 834.8 KeV, an E_0 of 37.7 photons per keV deposited [Holl 1988] and the value of P which was calculated as described in Chapter IV.

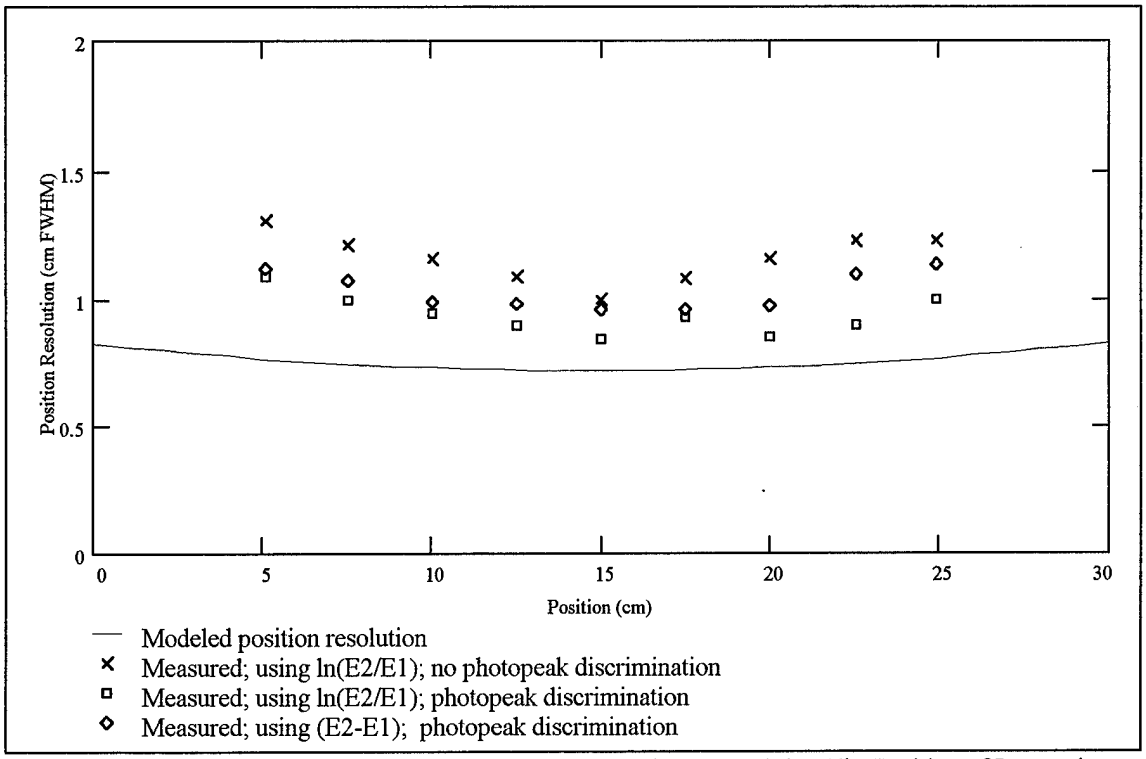

Figure 5-9. Resolutions Obtained From Three Techniques for Determining The Position of Interaction. Also shown is the modeled position resolution as a function of position.

The best position resolution was obtained by taking the natural log of the ratio of signal amplitudes produced by the PMTs as in Equation 5-7. These resolutions were taken from position spectra which were collected by counting full-energy photopeak events only. In the case where the radionuclide and therefore the incident gamma-ray energy is unknown, this luxury is not available and position information must be extracted from events which deposit a wide range of energies in the detector. In this case the two possibilities are to determine position according to Equations 5-6 and 5-8.

No useful position spectra based on Equation 5-8 were collected. This equation is based on the assumption that the light attenuation through the length of the detector can be approximated by a linear function. Apparently the light attenuation is too far from linear for this approximation to remain valid

over a wide range of deposited energies. Figure 5-10 shows how two position peaks were obtained when the detector was illuminated at 5.0 cm with ^{22}Na which produces polychromatic gamma-rays at 511 keV and 1275 keV. The non-peak events were produced by events which Compton scattered in the detector and deposited a continuum of energies. In contrast, Figure 5-11 shows a useful position spectrum collected under the same conditions. In this case position was determined from $\ln(E_2/E_1)$ as in Equation 5-6 whereby a single position peak was obtained.

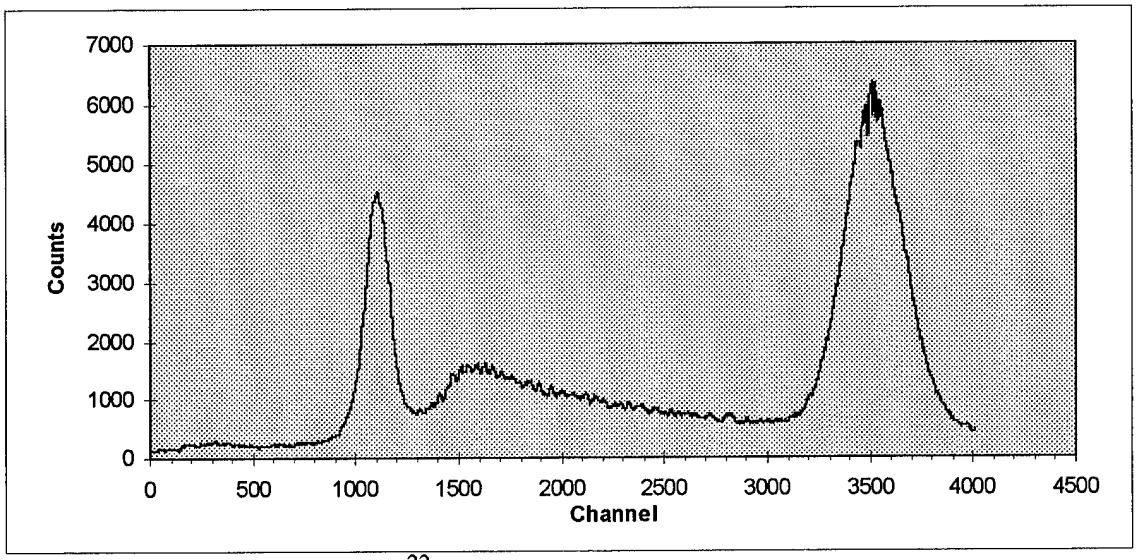

Figure 5-10. Position Spectra From ^{22}Na at 5.0 cm Where x α $(E_2-E_1)/(E_2+E_1)$. Two distinct position peaks are visible from the 511 keV and 1275 keV gamma rays.

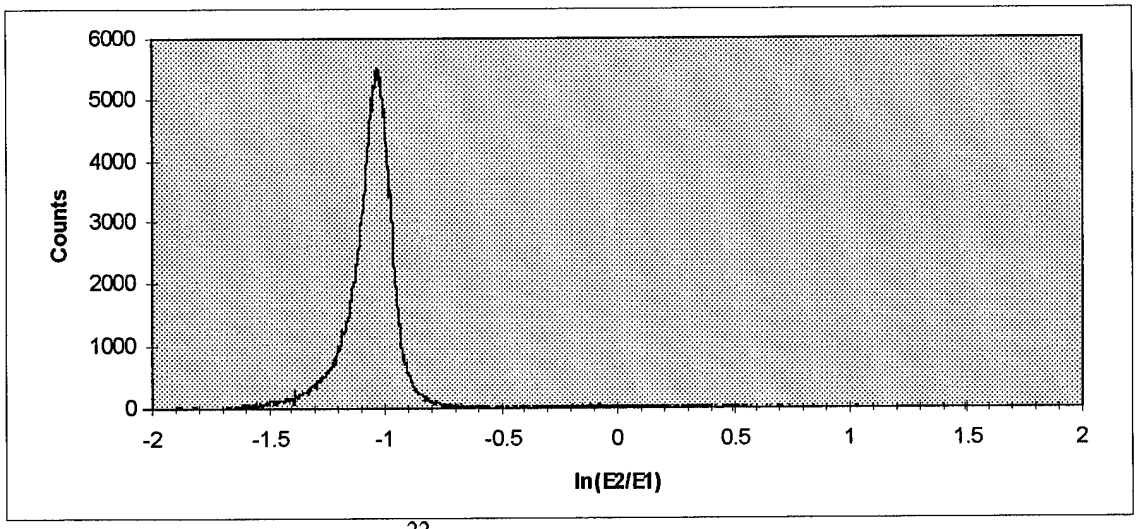

Figure 5-11. Position Spectra From ^{22}Na at 5.0 cm Where x α $\ln(E_2/E_1)$. One distinct position peak is visible despite the presence of both 511 keV and 1275 keV gamma rays.

The position spectra based on Equation 5-6 in which events of all energies are used to determine the position based on the natural log of the signal ratio gave the best position resolution in the case where the incident gamma-ray energy is unknown. The best position resolution was therefore given by the natural log of the signal ratio for both cases: incident gamma-rays of known or unknown energies.

The modeled position resolution shown in Figure 5-9 does not, however, take into account the uncertainty in the position of interaction due to the width of the collimated radiation beam. Rather, it is the position uncertainty expected from single interactions at various positions along the detector length. Therefore, this is the position uncertainty which will affect the angular resolution of the Compton camera. However, to establish the validity of the model, the position uncertainty due to the collimated beam width must be added to the modeled position uncertainty to ascertain whether the model is in agreement with the measured data. Recall that the uncertainty in the x-direction of the position of interaction is indicated by the total intensity function $I_{tot}(x)$ which describes the intensity of the collimated radiation beam as a function of x. Figure 4-6 shows the FWHM of the total intensity function $I_{tot}(x)$ described in Chapter IV as a function of the gamma-ray energy.

If the uncertainty due to the collimated beam width is represented as $FWHM_{coll}$ and the modeled position FWHM as described by Equation 2-7 is represented by $FWHM_{mod}$, then we can assume that $FWHM_{coll}$ can be added to $FWHM_{mod}$ in quadrature to model a total position uncertainty $FWHM_{tot}$ which accounts for the width of the collimated radiation beam. The value of $FWHM_{mod}$ is a function of both position and gamma-ray energy. The value of $FWHM_{coll}$ is a function of the gamma-ray energy only.

$$fwhm_{tot}\left(x, E_\gamma\right) = \sqrt{\left(fwhm_{\mathrm{mod}}\left(x, E_\gamma\right)\right)^2 + \left(fwhm_{coll}\left(E_\gamma\right)\right)^2} \quad \text{(Equation 5-10)}$$

Figure 5-12 shows that adding the value of $FWHM_{coll}$ at 834.8 keV to the model according to Equation 5-10 brings the modeled position uncertainty $FWHM_{tot}$ into good agreement with the measured position uncertainties.

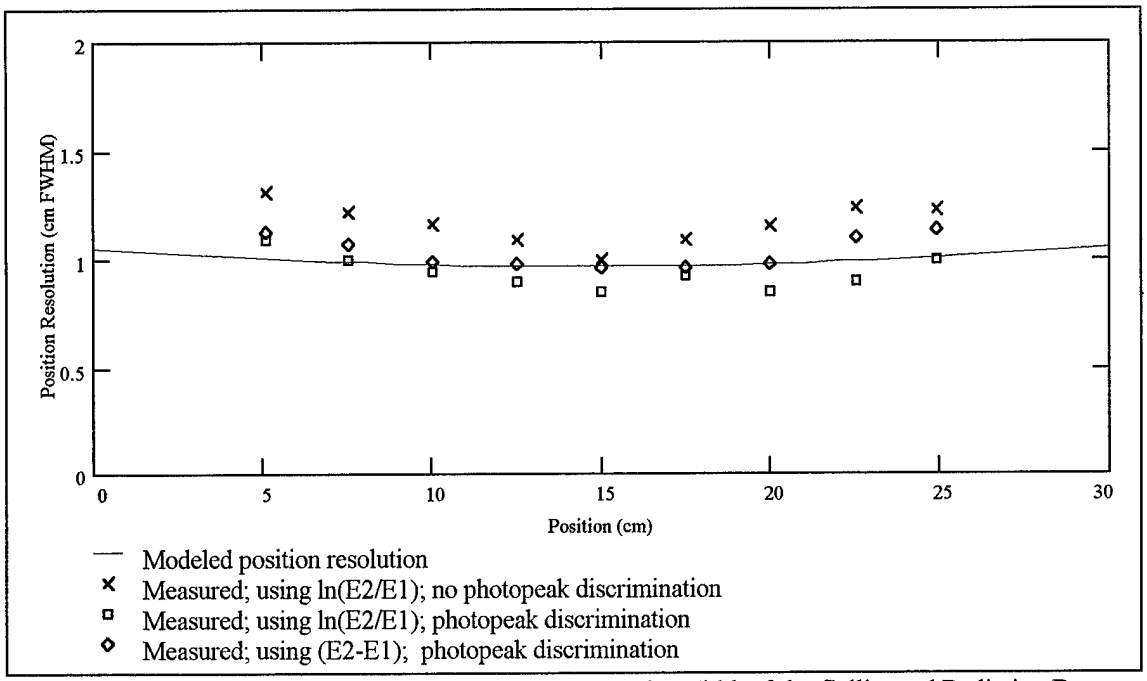

Figure 5-12. Modeled Position Resolution Corrected For the Width of the Collimated Radiation Beam and Measured Position Resolutions as a Function of Position. Modeled and measured results are for 834.8 keV gamma rays.

In some cases the measured uncertainties are better than predicted by theory. This observation suggests that an error exists in one or more model parameters. A likely possibility is that the value of the photoelectron probability P is too low. Another possibility is that the collimation beam width has a smaller effect on the measured position resolution than Equation 5-10 dictates. Because the value of α is well-established and in good agreement from both the measured and computer modeled data and the value of E_0 is well-established in the literature, they are unlikely sources of error. Nevertheless, the model predicts the measured position resolution well enough that it can be applied with confidence to hypothetical position-sensitive detectors.

If the x-dependence of $FWHM_{mod}$ is removed by using the value of $FWHM_{mod}$ $(x,E\gamma)$ averaged over the range of positions studied (5.0 cm to 25.0 cm) and that average is given the symbol ΔX_{mod},

$$\Delta X_{\mathrm{mod}}\left(E_\gamma\right)=\frac{\int_{5cm}^{25cm}\frac{2.35\cdot e^{\alpha L/4}}{2\alpha}\sqrt{\frac{e^{\alpha\left(x-\frac{L}{2}\right)}+e^{-\alpha\left(x-\frac{L}{2}\right)}}{E_\gamma P/E_o}}dx}{\int_{5cm}^{25cm}dx} \qquad \text{(Equation 5-11)}$$

then $FWHM_{tot}$ becomes a function of energy only and can be given the symbol ΔX_{tot}.

$$\Delta X_{tot}\left(E_\gamma\right)=\sqrt{\left(\Delta X_{\mathrm{mod}}\left(E_\gamma\right)\right)^2+\left(fwhm_{coll}\left(E_\gamma\right)\right)^2} \qquad \text{(Equation 5-12)}$$

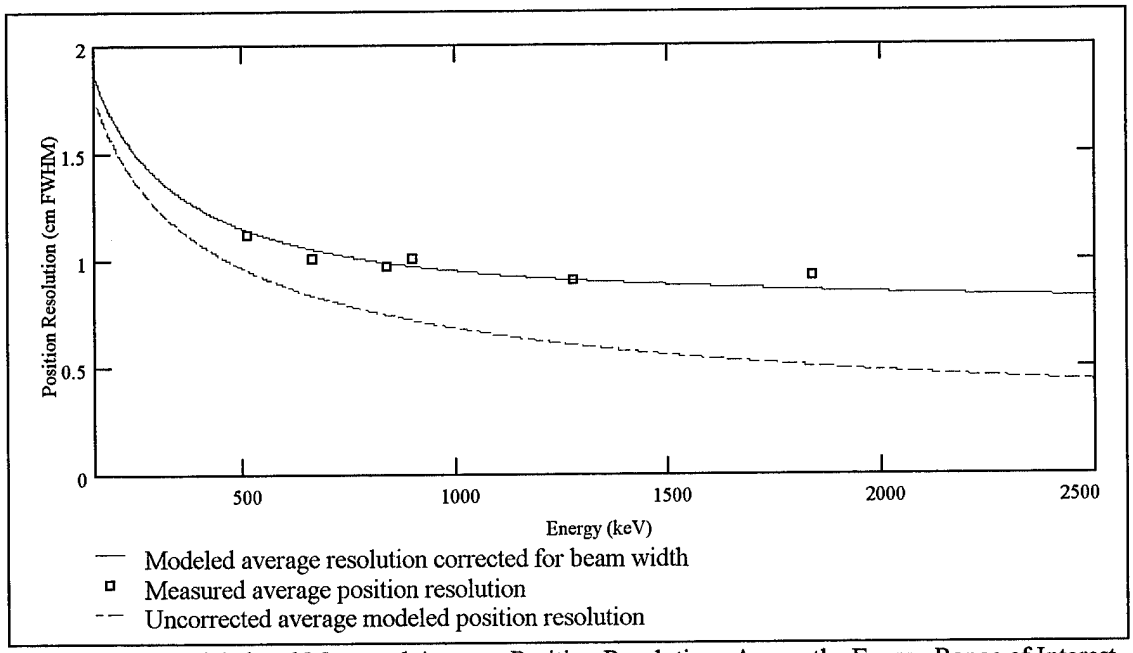

Figure 5-13. Modeled and Measured Average Position Resolutions Across the Energy Range of Interest. The solid line represents the model corrected for the width of the radiation beam. The dashed line represents the uncorrected model. The data points are the average measured position resolution at that energy.

Figure 5-13 shows how the average measured position uncertainty in centimeters FWHM agrees with the modeled $\Delta X_{tot}(E_\gamma)$ across the energy range of interest. Also shown in Figure 5-13 is the value of ΔX_{mod}

(E_γ). This is the true positional uncertainty expected from the detector when used in the proposed system, since the added uncertainty due to the width of the collimated radiation beam will not be present. Figure 5-13 shows that the modeled positional uncertainty agrees well with the measured positional uncertainty across the energy range studied.

Timing Resolution of the Second Detector Element

The timing resolution did not vary in any discernible pattern over the positions and energies studied. The average value of the FWHM of the timing peak was 68.6 channels. Calibration of the TAC revealed that each channel corresponds to .477 nanoseconds. The timing resolution therefore is 32.7 ns FWHM. The timing resolution represents the precision with which the timing circuitry pinpoint the time of an event. Good timing resolution is important in a Compton camera because it allows a narrow coincidence window to be set. A narrow coincidence window decreases the likelihood that random events will generate timing pulses within the coincidence window thereby recording a spurious event. For this reason the signal-to-noise ratio is improved with better timing resolution. The timing resolution reported here was accomplished with "off-the-shelf" electronics. It is expected that significant improvements could be made with customized electronics specifically designed for the Compton camera.

The Efficiency Model

Figure 5-14 illustrates the system geometry used to calculate the intrinsic peak efficiency of the proposed system. Cross-sectional views of both detector elements are shown. A ring of radius 24.65 cm was chosen to simulate an octagon which is 20 cm on each side.

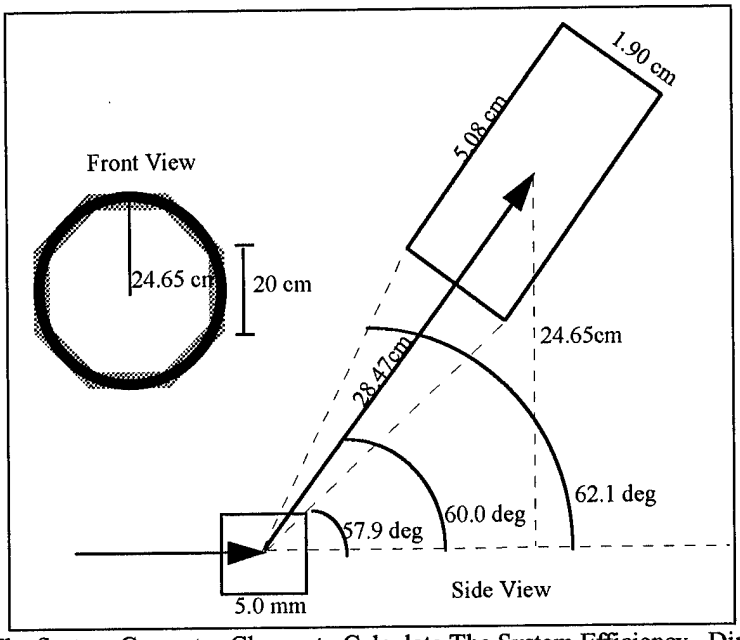

Figure 5-14. The System Geometry Chosen to Calculate The System Efficiency. Dimensions of the components are exaggerated so that the angles are more visible.

Before the system efficiency could be calculated according to the equations developed in Chapter II, the intrinsic peak efficiency of the second detector element ε_{ip2} as a function of energy had to be established. Data on the detector intrinsic peak efficiency was developed by first calculating the number of photons emitted into the detector by the gamma-ray source during the measurement period T. This calculation was based on the certificate value of the initial activity A_0, the fraction I of decays which lead to a gamma ray of interest being emitted, the age of the source t, the decay constant λ of the radioisotope in question and the solid angle subtended by the detector.

In calculating the solid angle subtended by the detector, the collimated radiation beam was again considered. The radius into which radiation was emitted was not well-defined due to the gradual falloff in intensity with distance from the center of the radiation beam as shown in Figure 4-3. The solid angle was calculated from the source-to-detector distance d and a value r_{mean} which characterizes the radius at the distance d into which the gammas were emitted. The value of d was taken to be the distance to the point halfway through the depth of the detector. The value of r_{mean} was calculated with the Mathematica

notebook [Appendix B] according to Equation 5-13 where I(r) is the intensity at a radius r from the center of the collimted radiation beam and r_0 is the radius at which the beam begins to become attenuated (r_0 = .350 cm at the value of d chosen). Because I(r) is energy-dependent, so is r_{mean}.

$$r_{mean} = \frac{\int_{r_o}^{\infty} rI(r)dr}{\int_{r_o}^{\infty} I(r)dr} \qquad \text{(Equation 5-13)}$$

If the number of counts in the corresponding photopeak is N_p, then the intrinsic peak efficiency at that energy is

$$\varepsilon_{ip0} = \frac{N_p}{\frac{\Omega}{4\pi}\left(IA_0e^{-\lambda t}\right)T}$$

where

$$\Omega = 2\pi\left(1 - \frac{d}{\sqrt{d^2 + r_{mean}{}^2}}\right)$$

Figure 5-15 depicts the measured intrinsic peak efficiencies which were calculated in the second detector for the energies studied. An exponential fit to the data is also shown which was used later to interpolate intrinsic peak efficiencies for a variety of energies.

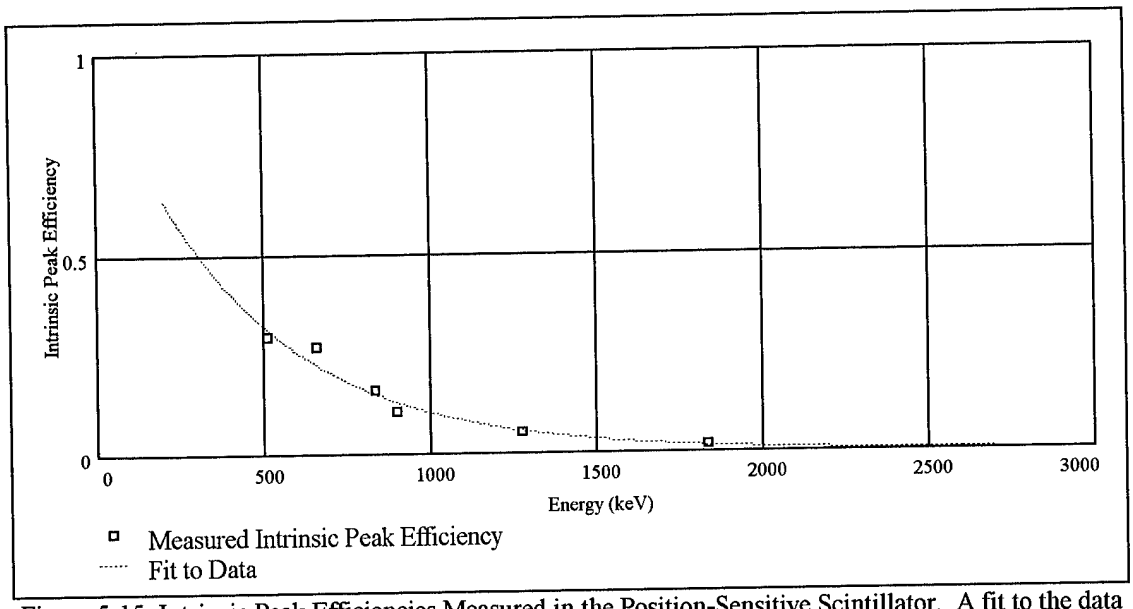

Figure 5-15. Intrinsic Peak Efficiencies Measured in the Position-Sensitive Scintillator. A fit to the data is also shown.

When these intrinsic peak efficiencies were measured, the incident gamma rays from the collimated beam could travel the full 5.08 cm depth of the scintillation crystal. For gamma rays scattered at various angles from the first detector into the second detector, this will not be the case. The possible path length through the NaI(Tl) crystal will vary as a function of the scattering angle. For instance, a photon incident along the detector axis which is scattered at an angle of exactly 60 degrees will have the opportunity to travel through 5.08 cm of NaI(Tl) crystal in which it may deposit its energy. A photon incident along the detector axis which is scattered at 62 degrees will have only a very short path through the NaI(Tl) crystal in which it may deposit its energy. The probability that a photon scattered at 60 degrees will cause a photopeak event is therefore greater than the probability that a photon scattered at 62 degrees will do so. This effect makes the intrinsic peak efficiencies of the second detector dependent on the angle of scatter. Based on the geometry of the model, the possible path length through the NaI(Tl) crystal is labeled $C(\theta)$ and is shown in Figure 5-16 as a function of scattering angle θ.

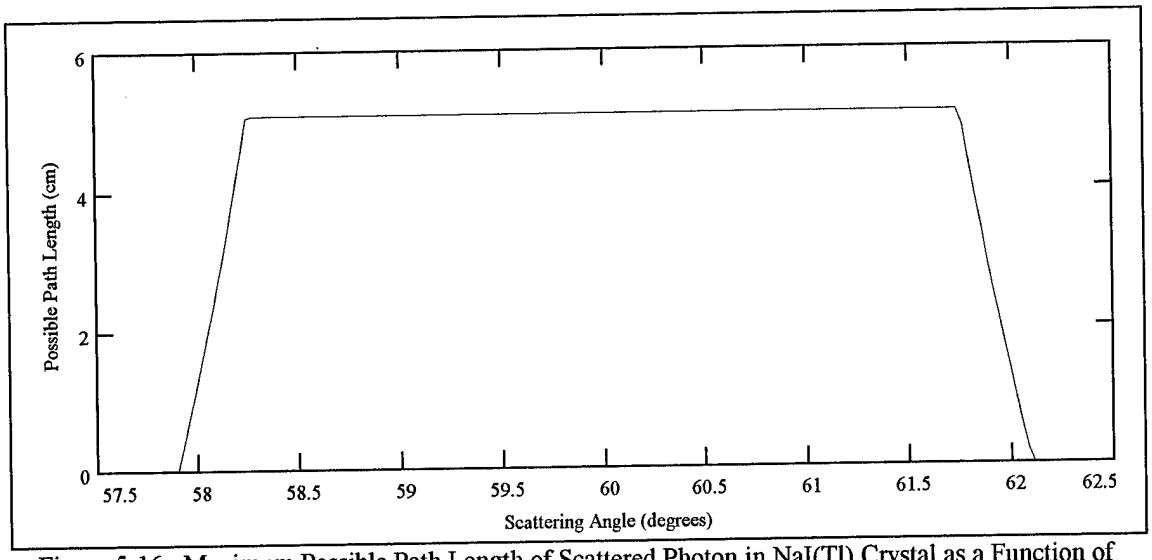

Figure 5-16. Maximum Possible Path Length of Scattered Photon in NaI(Tl) Crystal as a Function of Scattering Angle. Although not evident in the figure, the middle region surrounding 60 degrees is not linear, but slightly curved.

To correct the intrinsic peak efficiency for the variation in possible path length, it was given a θ-dependence according to Equation 5-14 where $\varepsilon_{ip0}(E_\gamma')$ is the intrinsic peak efficiency at the scattered photon energy which is interpolated from the fit to the data shown in Figure 5-15 and μ'_{NaI} is the total attenuation coefficient in NaI(Tl) for the scattered photon energy.

$$\varepsilon_{ip2}\left(\theta, E_\gamma{}'\right) = \varepsilon_{ip0}\left(E_\gamma'\right)\frac{1-e^{-\mu'_{NaI}C(\theta)}}{1-e^{-\mu'_{NaI}(5.08)}} \qquad \text{(Equation 5-14)}$$

Combining and modifying Equation 2-17 and Equation 2-18 results in the following expression for the intrinsic peak efficiency of the Compton camera.

$$\varepsilon_{\text{int}}\left(E_\gamma\right) = P_c\left(E_\gamma\right) f_2 \varepsilon_{ip2}\left(E_\gamma'\right) = \frac{\frac{\sigma_{Si}}{\mu_{Si}}\left(1-e^{-\mu_s 2L_1}\right)\int_{57.9^\circ}^{62.1^\circ} P(\theta,E_\gamma)e^{-\mu'_s S}\varepsilon_{ip2}\left(\theta,E_\gamma'\right)d\theta}{\int_0^\pi P(\theta,E_\gamma)d\theta} f_2$$

(Equation 5-15)

where the mean path length of the scattered photon through the cylindrical first detector has been made a constant S, and the theta dependence has been removed from scattered photon attenuation coefficient in

the first detector -- the coefficient for the 60 degree scattered photon μ_{Si}' will be used. Naturally, the attenuation coefficients are energy-dependent, although not explicitly shown above. Based on the system geometry, S=0.326 cm (the path length through the first detector for a photon scattered at 60 degrees from the center of the first detector).

The depth of the first detector L_1 was given an energy dependence to account for recoil electrons which escape the silicon crystal. Although the model assumes that interactions occur in the center of the detector, many will not. For Compton scatters which occur near the surface of the detector, the recoil electron may escape the detector, thereby depositing only a fraction of its energy and lowering the system efficiency. The recoil angle ϕ of the electron can be determined from $E\gamma$ and θ.

$$\tan(\phi) = \frac{1}{\left(1 + \frac{E_\gamma}{m_o c^2}\right)\tan\left(\frac{\theta}{2}\right)}$$

At the energies studied and a central scattering angle of 60 degrees, the recoil electrons will be nearly forward-recoiled (i.e. same direction as the incident photon). Reducing L_1 by the range of the recoil electron in silicon is a simple approximation which was used to account for recoil electron penetration of the first detector [Martin 1994:19]. Equation 5-15 was solved for various values of incident gamma ray energy. Figure 5-17 shows the results -- the predicted system intrinsic efficiency as a function of energy. Also shown is the predicted efficiency if only one second detector element were used. This is estimated by simply setting f_2=(1/8). The data points are the measured efficiency of the two detectors in coincidence at energies of 835 keV and 662 keV. The model predicts the intrinsic efficiency for an on-axis point source to within one-half order of magnitude.

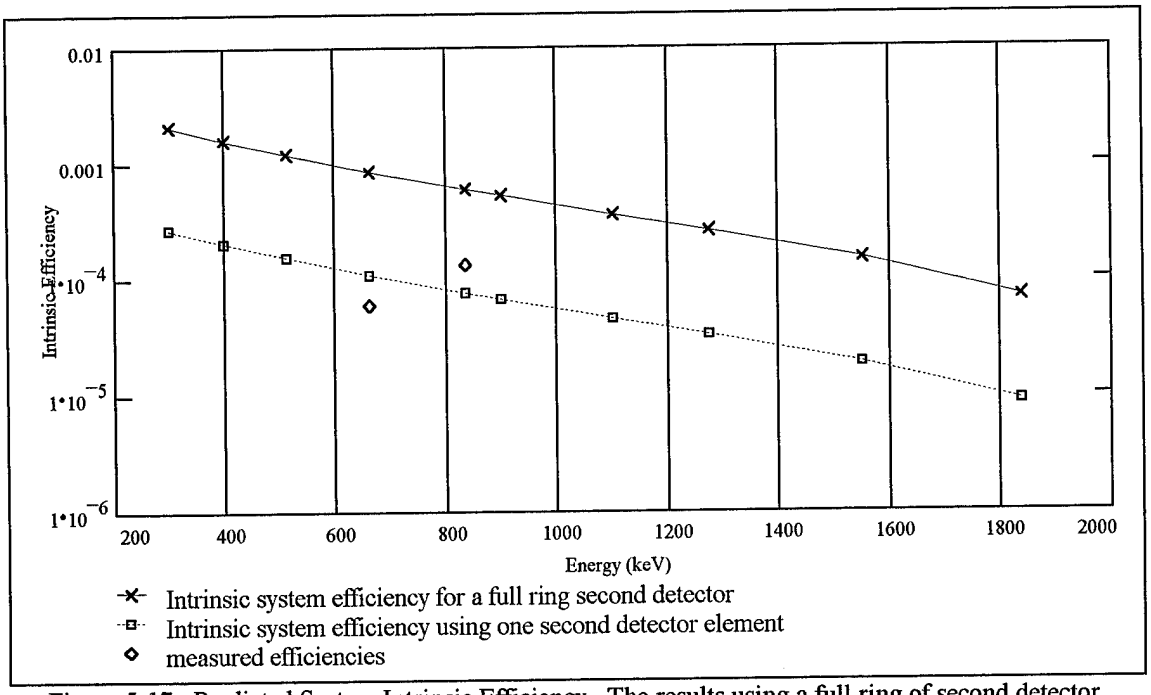

Figure 5-17. Predicted System Intrinsic Efficiency. The results using a full ring of second detector elements and single second detector element are shown.

In a system which uses an array of semiconductor detectors, the efficiency will be multiplied by the number of detector elements in the array.

Angular Resolution of System

As mentioned in Chapter I, the two factors which influence the angular resolution of the Compton camera system are the angular uncertainty in the direction of the cone axis $\Delta\theta_g$ (the geometric component) and the uncertainty in the cone angle $\Delta\theta_e$ (the energy component). These two components contribute to the total angular resolution $\Delta\theta_t$ according to Equation 1-2 [Martin 1994:19].

$$\tan^2(\Delta\theta_e) + \tan^2(\Delta\theta_g) = \tan^2(\Delta\theta_t) \qquad \text{(Equation 1-2)}$$

Because the cone axis is the line which connects the points of interaction in the two detectors, the angular uncertainty in the direction of the cone axis $\Delta\theta_g$ is a result of the uncertainty in the position of interaction in the two detectors. Angular error is associated with the half length of the first detector L_1,

the radius of the first detector R_1, and the dimensions of a resolution element in the second detector R_2. These error components are labeled $\Delta\theta_{L1}$, $\Delta\theta_{R1}$, and $\Delta\theta_{R2}$, respectively.

Figure 5-18 illustrates the error $\Delta\theta_{L1}$ due to the half length L_1 of the first detector element. Paths of photons which scatter in the center and at the face of the first detector are shown. When reconstructing an image with the Compton camera, it must be assumed that interactions in the first detector ocurred in the center since no position information in this detector is available. By the choice of system geometry, $\theta + \Delta\theta_{L1} = 60^o$. $\Delta\theta_{L1}$ can be determined by observing that

$$\theta = \tan^{-1}\left(\frac{24.65cm}{14.49cm}\right) = 59.46^o \qquad \Delta\theta_{L1} = 60^o - \theta = 0.54^o$$

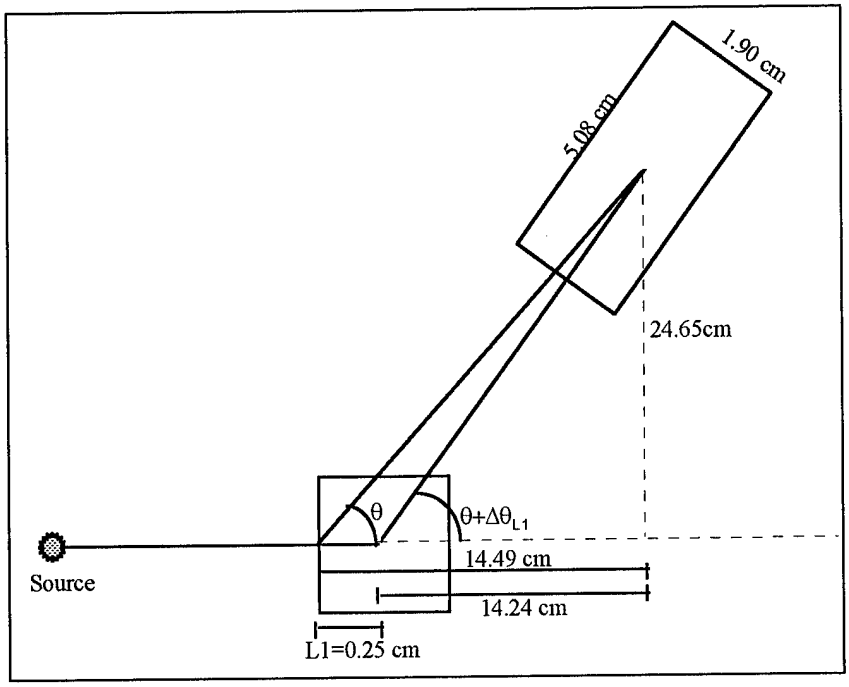

Figure 5-18. The $\Delta\theta_{L1}$ Geometric Error Component. The detector dimensions are exaggerated so that the differences in angles are visible.

Figure 5-19 illustrates the error $\Delta\theta_{R1}$ due to the radius of the first detector element. If the distance between the source and the first detector is much greater than the radius R_1 (0.282 cm) then the angle $\phi << \theta$ so that $\phi + \theta \approx \theta$. By neglecting ϕ in this way we assume that source is sufficiently far away

from the first detector that the two incident rays shown in Figure 5-19 can be considered parallel. In this case the value of $\Delta\theta_{R1}$ can be determined as follows.

$$\theta \approx \tan^{-1}\left(\frac{24.37cm}{14.24cm}\right) = 59.70^o \qquad \Delta\theta_{R1} = 60^o - \theta = 0.30^o$$

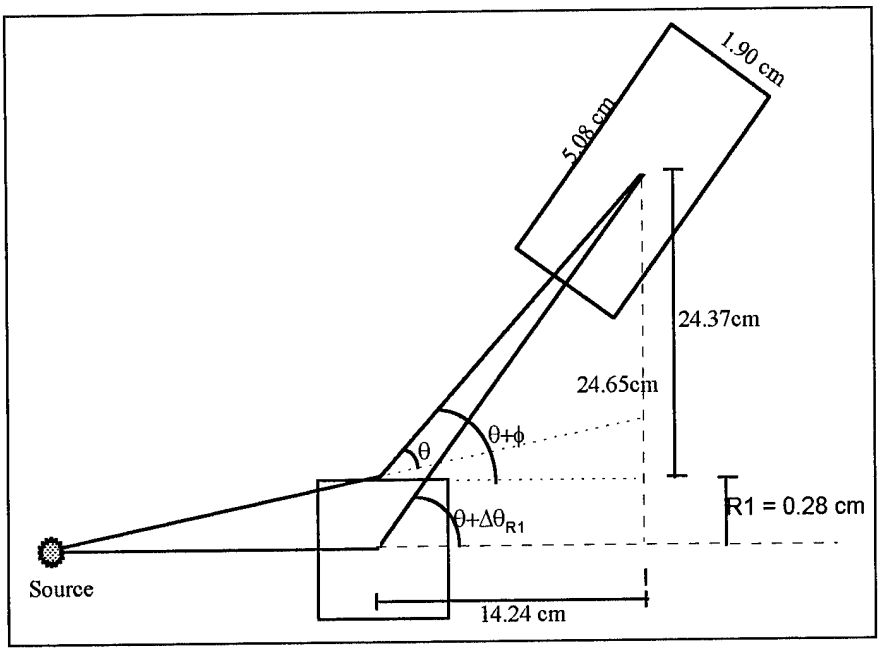

Figure 5-19. The $\Delta\theta_{R1}$ Geometric Error Component. The detector dimensions are exaggerated so that the differences in angles are visible.

Now $\Delta\theta_{R2}$ the geometric error component due to the dimensions of a resolution element in the second position-sensitive scintillator must be determined. The position resolution in the x-direction of the position-sensitive scintillator as a function of energy was characterized earlier. For any given range of x at which the event can be localized, the event may have taken place at any y-value across the 1.9 cm height of the crystal. The uncertainty in the x and y directions will affect $\Delta\theta_g$ and are the dimensions of a resolution element. The total uncertainty R_2 in the position of interaction will be the quadratic sum of the x and y uncertainties as shown in Equation 5-16.

$$R_2(E_\gamma) = \sqrt{\left(\Delta X\left(E_\gamma{}'\right)\right)^2 + \left(\frac{1.90}{2}cm\right)^2} \qquad \text{(Equation 5-16)}$$

Figure 5-20 illustrates the dimensions of a resolution element in the second detector and how the total uncertainty R_2 affects the angular uncertainty $\Delta\theta_{R2}$. $\Delta\theta_{R2}$ is given by

$$\Delta\theta_{R2}\left(E_\gamma\right) = \tan^{-1}\left(\frac{R_2\left(E_\gamma\right)}{28.47cm}\right)$$

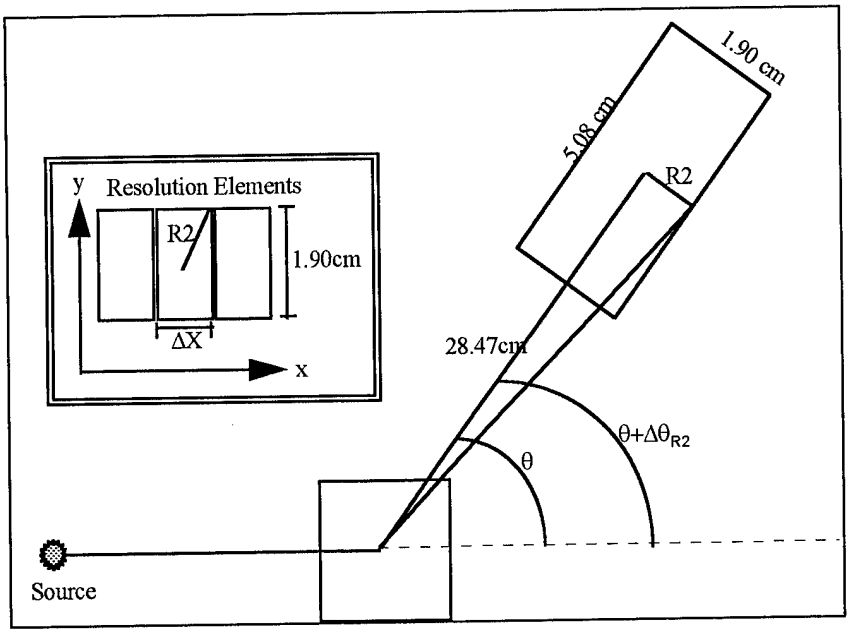

Figure 5-20. The $\Delta\theta_{R2}$ Geometric Error Component. The detector dimensions are exaggerated so that the differences in angles are visible.

Once the geometric error components have been determined, the total geometric error $\Delta\theta_g$ is given in FWHM angular resolution by [Martin 1994:20]

$$\tan^2\left(\Delta\theta_g\left(E_\gamma\right)\right) = 4\left[\tan^2\left(\Delta\theta_{R1}\right) + \tan^2\left(\Delta\theta_{L1}\right) + \tan^2\left(\Delta\theta_{R2}\left(E_\gamma\right)\right)\right] \qquad \text{(Equation 5-17)}$$

The total geometric error is therefore a function of the incident gamma-ray energy because the energy will affect the positional uncertainty in the second detector.

The energy component of the angular resolution $\Delta\theta_e$ represents the uncertainty in the angle θ of the interaction cone. It is related to the precision with which energy is measured in the detector elements. Three cases must be considered which will affect the way in which $\Delta\theta_e$ is determined. These cases are:

1) The energy of the incident gamma ray is known. This case would apply if the Compton camera were imaging a known radionuclide, for example. 2) The energy of the incident gamma ray can be determined after the image data is taken by summing the energies deposited in both detectors for a large number of events. E_γ is then the centroid of a peak in the summed energy spectrum. 3) The energy of the incident gamma ray is unknown and can be taken as the sum of the energy deposited in both detectors on an event-by-event basis.

In the first case, if the energy of the incident gamma ray is known, then only the uncertainty in measuring the scattered photon energy (the energy resolution of the second detector $\Delta E_\gamma'$ in FWHM) will affect $\Delta\theta_e$. The energy deposited in the second detector E_γ' is the only information needed to determine the scattering angle. It is also possible to determine the scattering angle with the energy E_{re} deposited in the first detector and at first glance this seems the better choice because the absolute energy resolution is better in the first detector over much of the energy range. However, $\Delta\theta_e$ will also be influenced by the variation in theta with respect to the variation in the quantity measured. If the recoil electron energy is measured to find E_γ, then

$$(\Delta\theta_e)^2 = \left(\frac{\partial\theta}{\partial E_{re}}\right)^2 (\Delta E_{re})^2 \qquad \text{(Equation 5-18)}$$

where $\partial\theta/\partial E_{re}$ is given by Equation 2-16 and the energy resolution in the first detector is labeled ΔE_{re}. If the scattered photon energy is measured, then

$$(\Delta\theta_e)^2 = \left(\frac{\partial\theta}{\partial E_\gamma'}\right)^2 (\Delta E_\gamma')^2 \qquad \text{(Equation 5-19)}$$

where the energy-dependent energy resolution in the position-sensitive scintillator is labeled $\Delta E_\gamma'$ and $\partial\theta/\partial E_\gamma'$ is obtained by solving Equation 1-1 for $\cos(\theta)$ and differentiating with respect to E_γ'.

$$\frac{\partial\theta}{\partial E'_\gamma} = -\frac{1}{\sin(\theta)}\frac{m_0c^2}{E'^2_\gamma} \qquad \text{(Equation 5-20)}$$

Figure 5-21 illustrates how the energy component $\Delta\theta_e$ changes with energy if θ is determined from the energy deposited in the first detector or second detector.

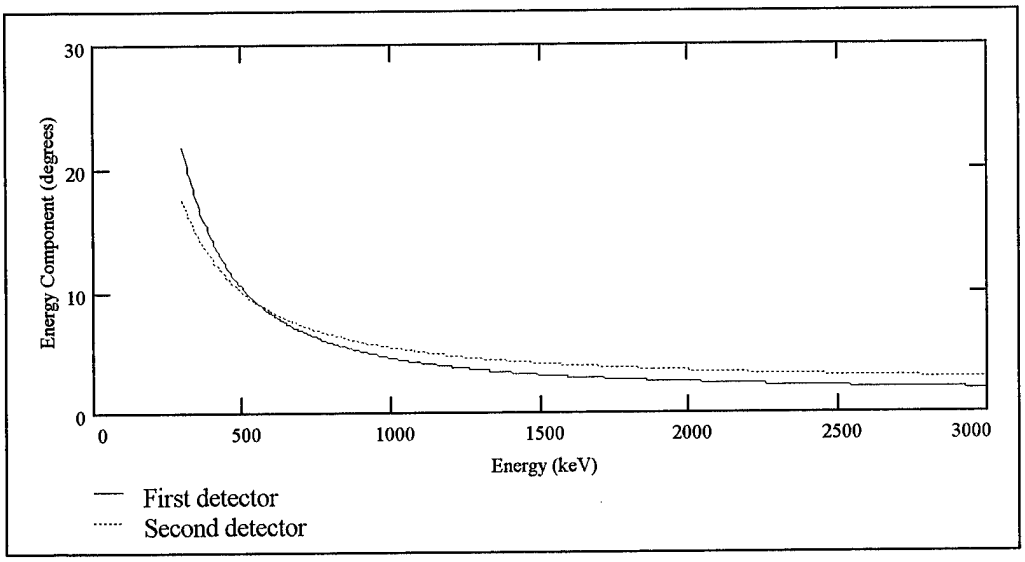

Figure 5-21. Energy Component $\Delta\theta_e$ of the Angular Uncertainty When θ is Determined from the First or Second (NaI(Tl)) Detector.

From Figure 5-21 it is clear that the best choice to minimize $\Delta\theta_e$ is to measure E_γ' at lower energies (less than 547 keV) and take the energy deposited in the first detector to be the difference between E_γ and E_γ' so that $\Delta\theta_e$ will be given by Equation 5-19. If the known gamma-ray energy is greater than 547 keV, then the best choice to minimize $\Delta\theta_e$ is to measure the recoil electron energy in the first detector so that $\Delta\theta_e$ will be given by Equation 5-18.

In case 2, E_γ is the centriod of an energy peak in the summed energy spectrum. $\Delta\theta_e$ will therefore also be influenced by the error in locating the centroid of a peak in the summed energy spectrum. If this error is labeled ΔE_γ then

$$(\Delta\theta_e)^2 = \left(\frac{\partial\theta}{\partial E_{re}}\right)^2 (\Delta E_{re})^2 + \left(\frac{\partial\theta}{\partial E_\gamma}\right)^2 (\Delta E_\gamma)^2 \qquad \text{(Equation 5-21)}$$

where by taking the partial derivative of θ in Equation 1-1 with respect to E_γ,

$$\frac{\partial\theta}{\partial E_\gamma} = -\frac{m_0c^2}{\sin(\theta)}\left(\frac{1}{(E_\gamma - E_{re})^2} - \frac{1}{E_\gamma{}^2}\right)$$

ΔE_γ was taken from summed energy spectra of both detectors in coincidence. An average error of 50.0 keV was used in the calculations.

In case 3, the summed energy on an event-by event basis is taken to be E_γ so that the energy resolutions in the first and second detectors are used to determine $\Delta\theta_e$. Again the uncertainties are added quadratically as in Equation 5-22.

$$(\Delta\theta_e)^2 = \left(\frac{\partial\theta}{\partial E_{re}}\right)^2 (\Delta E_{re})^2 + \left(\frac{\partial\theta}{\partial E_\gamma{}'}\right)^2 (\Delta E_\gamma{}')^2 \qquad \text{(Equation 5-22)}$$

where the partial derivative of θ with respect to E_{re} in terms of E_γ' is

$$\frac{\partial\theta}{\partial E_{re}} = -\frac{m_0c^2}{\sin(\theta)}\left(\frac{1}{(E_\gamma{}' + E_{re})^2}\right) \qquad \text{(Equation 5-23)}$$

and the partial derivative of θ with respect to E_γ' in terms of E_{re} is

$$\frac{\partial\theta}{\partial E_\gamma'} = -\frac{m_0c^2}{\sin(\theta)}\left(\frac{1}{(E_\gamma{}' + E_{re})^2} - \frac{1}{(E_\gamma{}')^2}\right) \qquad \text{(Equation 5-24)}$$

Having thus established $\Delta\theta_g$ and $\Delta\theta_e$, which are both functions of the incident gamma-ray energy, it is possible to predict the angular resolution of the Compton camera as a function of energy for the three cases described above. The modeled average values of the position resolution as a function of energy in the position-sensitive scintillator are used because they were found to generally agree with the measured resolution. The theoretical energy resolution in the position-sensitive scintillator is corrected by the factor K_E which was found to bring the theoretical values into general agreement with those measured. Recall that ΔE_{re} was found to remain essentially constant since the first detector element energy resolution was dominated by noise. Figure 5-22 shows the results.

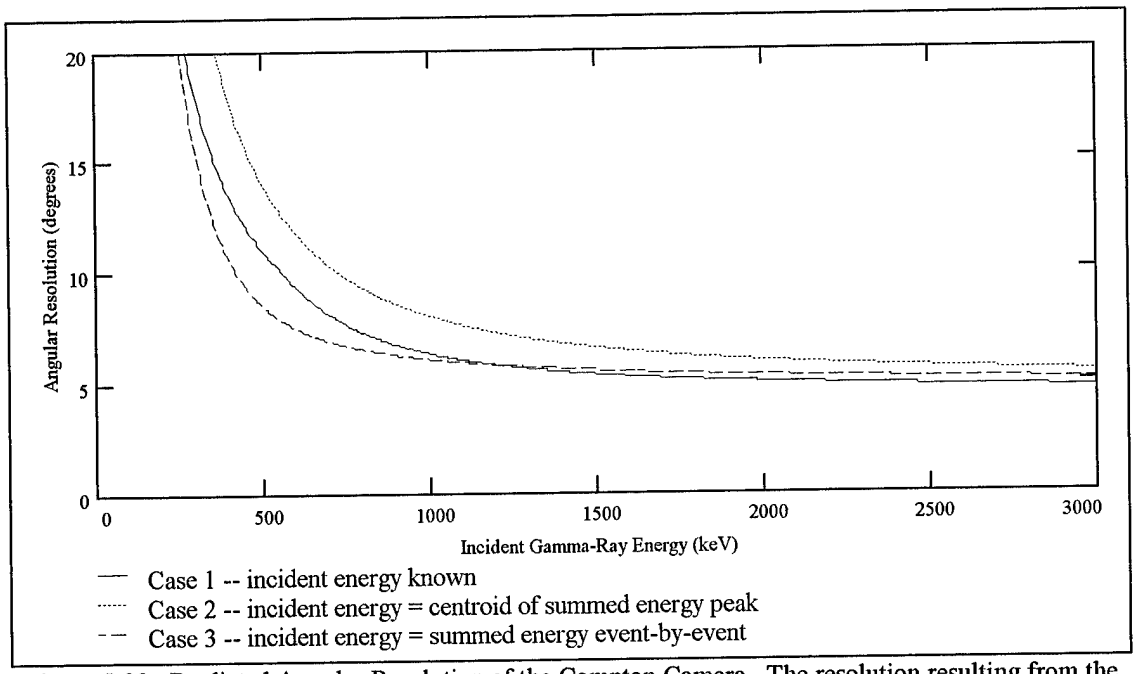

Figure 5-22. Predicted Angular Resolution of the Compton Camera. The resolution resulting from the three methods for determining the incident gamma-ray energy are shown.

An interesting and result is revealed by Figure 5-22. At some energies the angular resolution obtained by summing the energies deposited in both detectors event-by-event (case 3) is better than that obtained by using the energy deposited in one detector only (case 1). Insight into the cause of this phenomena is gained by inspection of Equations 2-16, 5-20, 5-23, and 5-24. Due to the limited energy resolution of both detectors, there will always be some uncertainty in measured energy; whether it is the

recoil electron energy, the scattered photon energy, or both. The partial derivative of θ with respect to the measured energy reveals how the uncertainty in the measured energies influence the uncertainty in θ.

In case 1, the incident energy is presumed known, and the scattering angle θ is determined by measuring the energy deposited in one detector only. Either Equation 2-16 or Equation 5-20 describe the variation in θ with respect to the measured energies. Both of these partial derivatives vary as the inverse square of the scattered photon energy E_γ'. In Equation 2-16 the scattered photon energy is taken to be the difference between the known incident energy and the measured recoil electron energy.

$$\frac{\partial\theta}{\partial E_{re}} = \frac{m_o c^2}{\sin(\theta)}\left[\frac{1}{\left(E_\gamma - E_{re}\right)^2}\right] \qquad \text{(Equation 2-16)}$$

$$\frac{\partial\theta}{\partial E_\gamma'} = -\frac{1}{\sin(\theta)}\frac{m_0 c^2}{E_\gamma'^2} \qquad \text{(Equation 5-20)}$$

In case 3, the energy deposited in both detectors is used to determine θ, therefore the uncertainty in both measured energies will infuence the uncertainty in θ. For case 3, Equations 5-20 and 5-24 describe how θ varies with the recoil electron energy and scattered photon energy, respectively.

$$\frac{\partial\theta}{\partial E_{re\gamma}} = -\frac{m_0 c^2}{\sin(\theta)}\left(\frac{1}{\left(E_\gamma{}' + E_{re}\right)^2}\right) \qquad \text{(Equation 5-23)}$$

$$\frac{\partial\theta}{\partial E_\gamma'} = -\frac{m_0 c^2}{\sin(\theta)}\left(\frac{1}{\left(E_\gamma{}' + E_{re}\right)^2} - \frac{1}{\left(E_\gamma{}'\right)^2}\right) \qquad \text{(Equation 5-24)}$$

Equation 5-23 shows that the partial derivative of θ with respect to E_{re} varies as the inverse square of the incident energy E_γ. This is in contrast to case 1 where it varied as the inverse square of the scattered photon energy E_γ' (Equation 2-16). It follows that since E_γ' is always less than a given E_γ, for any E_γ the

uncertainty in E_{re} will have a greater influence on the uncertainty in θ in case 1 (where Equation 2-16 applies) than it will in case 3 (where Equation 5-23 applies). This greater uncertainty in θ translates into poorer angular resolution for case 1 compared to case 3 at some energies. Case 3 does not exhibit better angular resolution than case 1 over the entire energy range, however, since the uncertainty in measuring E_{γ}' also contributes to the uncertainty in θ. At energies above 1200 keV, this contribution is large enough to make the angular resolution for case 3 worse than the angular resolution for case 1. The interesting result is that even when imaging a radiation field of known energy, the best angular resolution is achieved at some energies by summing the energies deposited in both detectors event-by-event.

The characteristics of the NaI(Tl) position-sensitive scintillator were modeled by parameterizing the results of the NaI(Tl) DETECT simulation for a value of α and P_{pmt}. The same procedure was used to predict the response of the hypothetical CsI(Tl) position-sensitive scintillator based on more DETECT simulations.

Results With Hypothetical CsI(Tl) Position-Sensitive Scintillator

With the validity of the model for positional uncertainty and the relationship between the modeled and actual energy resolutions being thus established, the model can be applied to the case of the hypothetical cesium-iodide (CsI(Tl)) based position-sensitive scintillator. The objective is to predict the angular resolution which could be expected from a system with similar geometry and which uses a similar first detector element. Figure 5-23 shows the results of the DETECT simulation of a similarly-sized CsI(Tl) position-sensitive scintillator. The natural log of the ratio of the simulated photons collected at each end is plotted vs. the position at which they were generated.

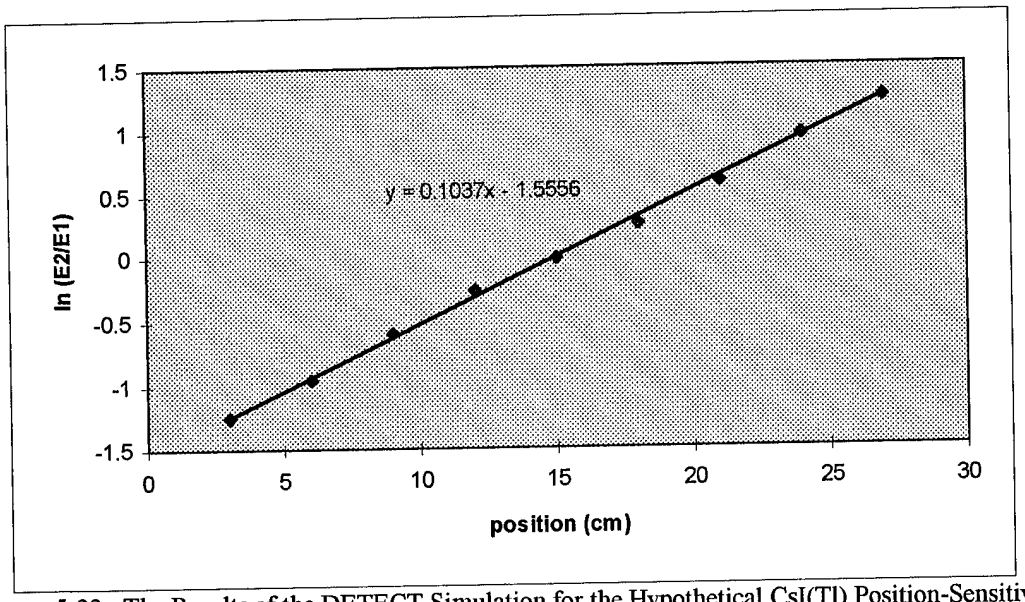

Figure 5-23. The Results of the DETECT Simulation for the Hypothetical CsI(Tl) Position-Sensitive Scintillator

The equation displayed in Figure 5-23 gives the least-squares fit to the data. Replacing y with $\ln(E_2/E_1)$ and solving for x gives

$$x = \frac{1}{0.1037}\ln\left(\frac{E_2}{E_1}\right) + 15.00$$

which, from Equation 2-5 reveals that the light attenuation coefficient α is (0.1037)/2 or 0.0518. Using the values of P and E_o which were given in Chapter IV, Carter's equations will give the position (Equation 2-7) and energy (Equation 2-8) resolution of the detector. For the purpose of comparison, Figure 5-24 shows the average position resolution as a function of energy for both the NaI(Tl) and CsI(Tl) detectors. Figure 5-25 shows the average energy resolution as a function of energy for both detectors. The energy resolutions have been corrected by the K_E factor developed to match DETECT modeled results to the measurements.

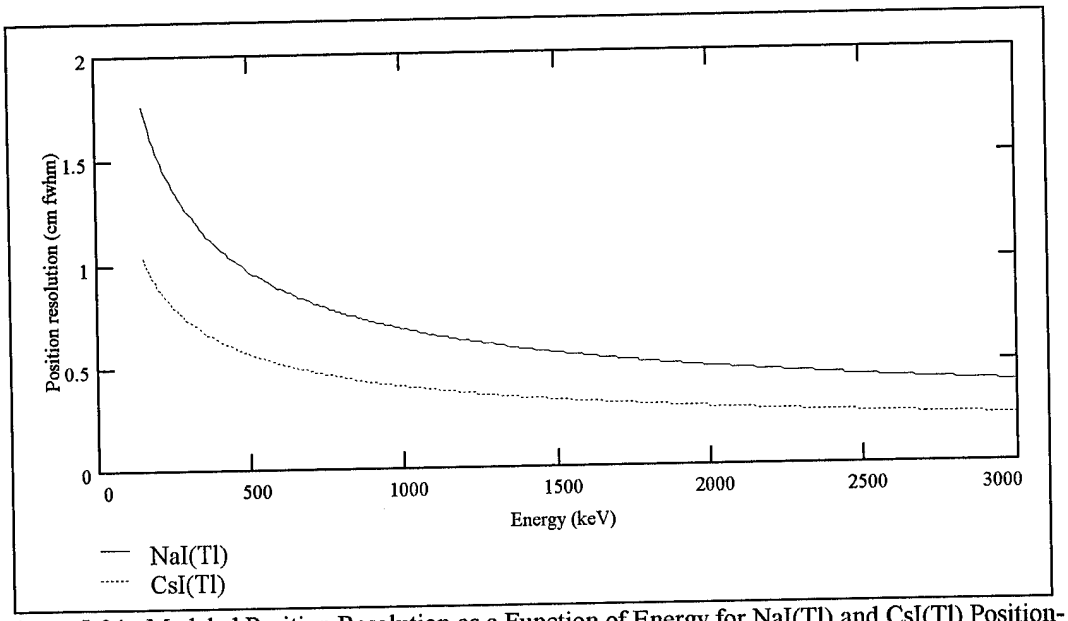

Figure 5-24. Modeled Position Resolution as a Function of Energy for NaI(Tl) and CsI(Tl) Position-Sensitive Scintillators.

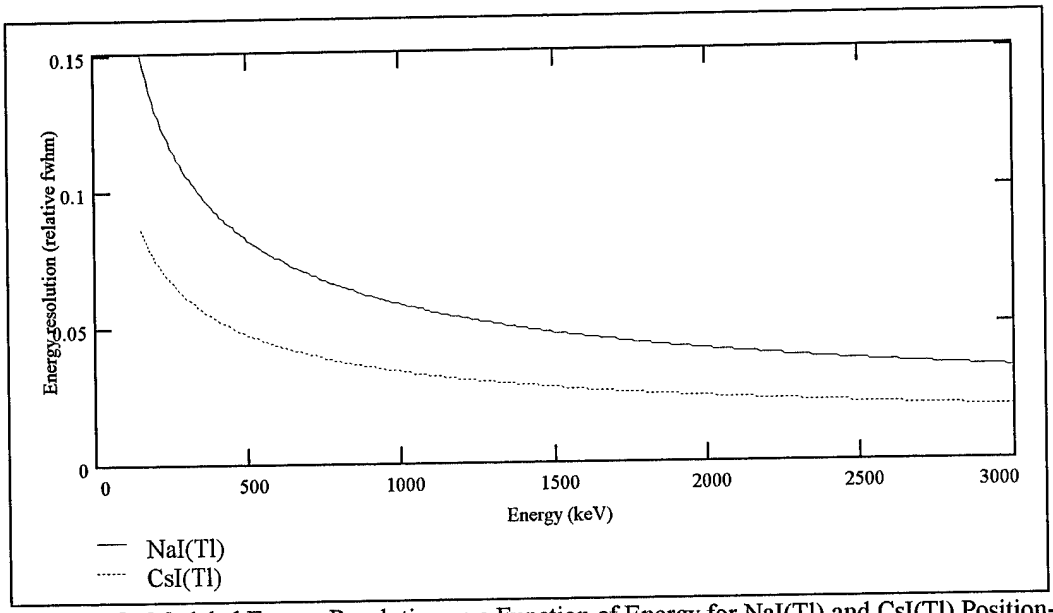

Figure 5-25. Modeled Energy Resolution as a Function of Energy for NaI(Tl) and CsI(Tl) Position-Sensitive Scintillators.

In the case of a known incident gamma-ray energy (case 1) in the CsI(Tl)-based Compton camera, measuring E_γ' always gives a smaller $\Delta\theta_e$ than measuring E_{re}, so $\Delta\theta_e$ is always given by

Equation 5-20. Figure 5-26 shows the values of $\Delta\theta_e$ which result from deriving θ from the energy deposited in the first or second detectors.

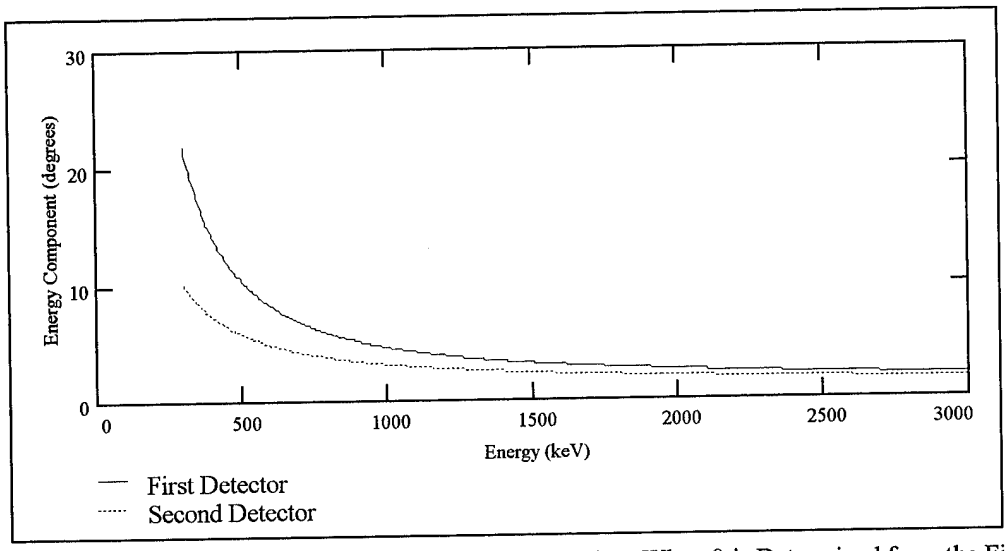

Figure 5-26. Energy Component $\Delta\theta_e$ of the Angular Uncertainty When θ is Determined from the First or Second (CsI(Tl)) Detector.

Figure 5-27 shows the angular resolution as a function of energy. Case 2 is not shown because $\Delta E\gamma$, which was measured for the NaI(Tl) detector, was not available for the hypothetical CsI(Tl) detector.

The system angular resolution is a measure of the "sharpness" of an image which can be constructed with the Compton camera. Better angular resolution results in improved certainty in the location and spatial distribution of the radioactive source. In the counterproliferation mission, it is important to determine not only the location and spatial distribution of the source, but also the nature of the source.

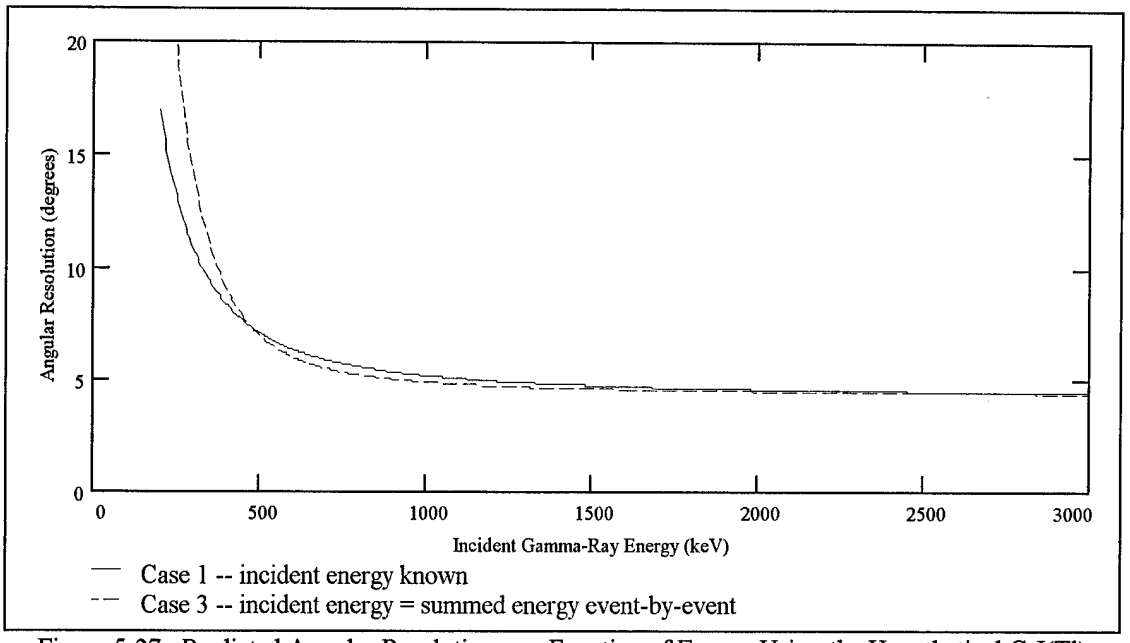

Figure 5-27. Predicted Angular Resolution as a Function of Energy Using the Hypothetical CsI(Tl) Position-Sensitive Detector.

System Spectroscopic Capabilities

The spectroscopic capability of the Compton Camera is important because accurately identifying the energies of incident gamma rays leads to the correct identification of the radioactive isotopes which are the source of the radiation. Corrrectly identifying the isotopes present at a sight is important in the counterproliferation mission because gives insight into the nature of the nuclear activity there.

The energy resolution of the system for a given E_γ can be calculated by quadratically summing the energy resolution of the first detector at the recoil electron energy E_{re} and the energy resolution of the second detector at the scattered photon energy E_γ'. For this calculation the source is assumed to be sufficiently far away that it can be approximated as a point source on the detector axis, thereby fixing the scattering angle θ, E_{re}, and E_γ' for a given E_γ. The system energy resolution of both the NaI(Tl)-based system and CsI(Tl)-based system are illustrated in Figure 5-28 as well as the energy resolution of the NaI(Tl) scintillator if it were used individually for spectroscopy.

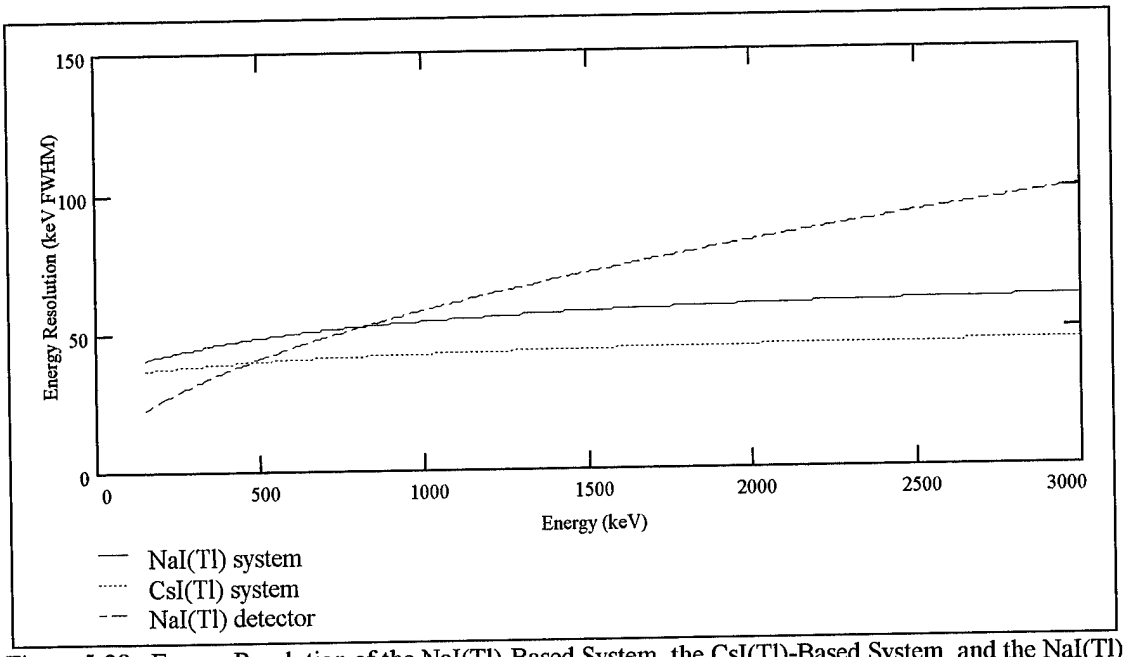

Figure 5-28. Energy Resolution of the NaI(Tl)-Based System, the CsI(Tl)-Based System, and the NaI(Tl) Detector Alone.

Figure 5-28 illustrates how the NaI(Tl) system energy resolution surpasses that of the scintillator alone at energies greater than 800 keV. In the Compton camera system, E_γ' is measured in the second detector rather than the full E_γ which would be measured if the scintillator alone were used for spectroscopy. Lowering the energy incident on the scintillator improves its absolute energy resolution so that at higher energies the second detector contribution to the total energy resolution is smaller than its resolution at E_γ. The system should be able to resolve two incident gamma-ray energies which are seperated by more than one FWHM [Knoll 1989:110]. The CsI(Tl)-based system is better at resolving closely-spaced energy peaks, and so is a better choice for spectroscopy than the NaI(Tl) system. To use the CsI(Tl) system for isotope identification in a multispectral field, energy peaks would have to be seperated by about 45 keV. The enrgy resolution of the NaI(Tl) system was demonstrated by collecting summed energy spectra.

Summed Energy Spectra

Summed energy spectra were collected from a ^{54}Mn source (835 keV) placed on the system central axis so that $\theta = 60$ degrees and from the same source displaced 44 degrees from the axis so that $\theta = 104$ degees. Collection involved positioning the detectors (the position-sensitive NaI(Tl) and the room-temperature Si(Li))relative to each other as in the proposed system and summing the coincident event energies recorded in both detectors. The on-axis spectra are shown in Figure 5-29.

Solving Equations 2-13 and 2-14 for a 60 degree scattering angle indicates that an energy peak at $E_\gamma' = 459.5$ keV should occur in the second detector an an energy peak at $E_{re} = 375.5$ keV should occur in the first detector. These peaks are seen in the first two spectra of Figure 5-29. Likewise for $\theta =$ 104 degrees, the exepcted energy peaks at $E_\gamma' = 276$ keV in the second detector and $E_{re} =$ 559 keV in the first detector are seen in Figure 5-30. These energy peaks don't exhibit the resolution of their respective detectors because the source was positioned so close to the second detector that a range of scattering angles near 60 degrees was available for photons to scatter from the first detector into the second. In other words, the ϕ of Figure 5-19 was not negligible. The third spectrum in Figure 5-29 shows the summed energy spectrum for $\theta = 60$ degrees with the expected full-energy peak at $E_\gamma = 835$ keV. The resolution of this full-energy peak is 65 keV FWHM, which is slightly worse than predicted by Figure 5-28. On the other hand, the summed energy peak for $\theta = 104$ degrees has a resolution of 56 keV FWHM which is in good agreement with Figure 5-28.

The abundance of counts below the full-energy peak can be attributed to one of two causes. The first mechanism which causes the low-energy events is recoil electron penetration of the first detector volume. If the incident photon Compton scatters near a surface of the first detector's active volume and the recoil electron escapes the active volume, then the full E_{re} is not recorded. The second mechanism which causes the low-energy events is an additional Compton scatter of the scattered photon in the second detector crystal. If the photon resulting from the additional scatter escapes the scintillator without

depositing its full energy, then the full E_γ' is not recorded in the second detector. Either of these mechanisms cause an erroneous energy recording and contaminate the image because they lead to erroneous information on θ and the direction of incident radiation. To construct a clear image, it is important to minimize these contaminating events as much as possible.

The spectra in Figures 5-29 and 5-30 point to the second mechanism, scattering in the second detector, as the predominant source of these contaminating events.

The intensity of full-energy events relative to contaminating events constitutes a signal-to-noise ratio. The peak-to-total ratio in the off-axis summed energy spectrum is lower than the peak-to-total ratio in the on-axis summed energy spectrum. Increasing the energy measured by either detector will decrease its peak-to-total ratio and increase its contribution to the contaminating events. In the off-axis spectrum θ was increased, thus increasing E_{re} and decreasing E_γ'. Since the signal-to-noise ratio improved, the detector which measures E_γ', the second detector, can be identified as the primary source of contaminating events.

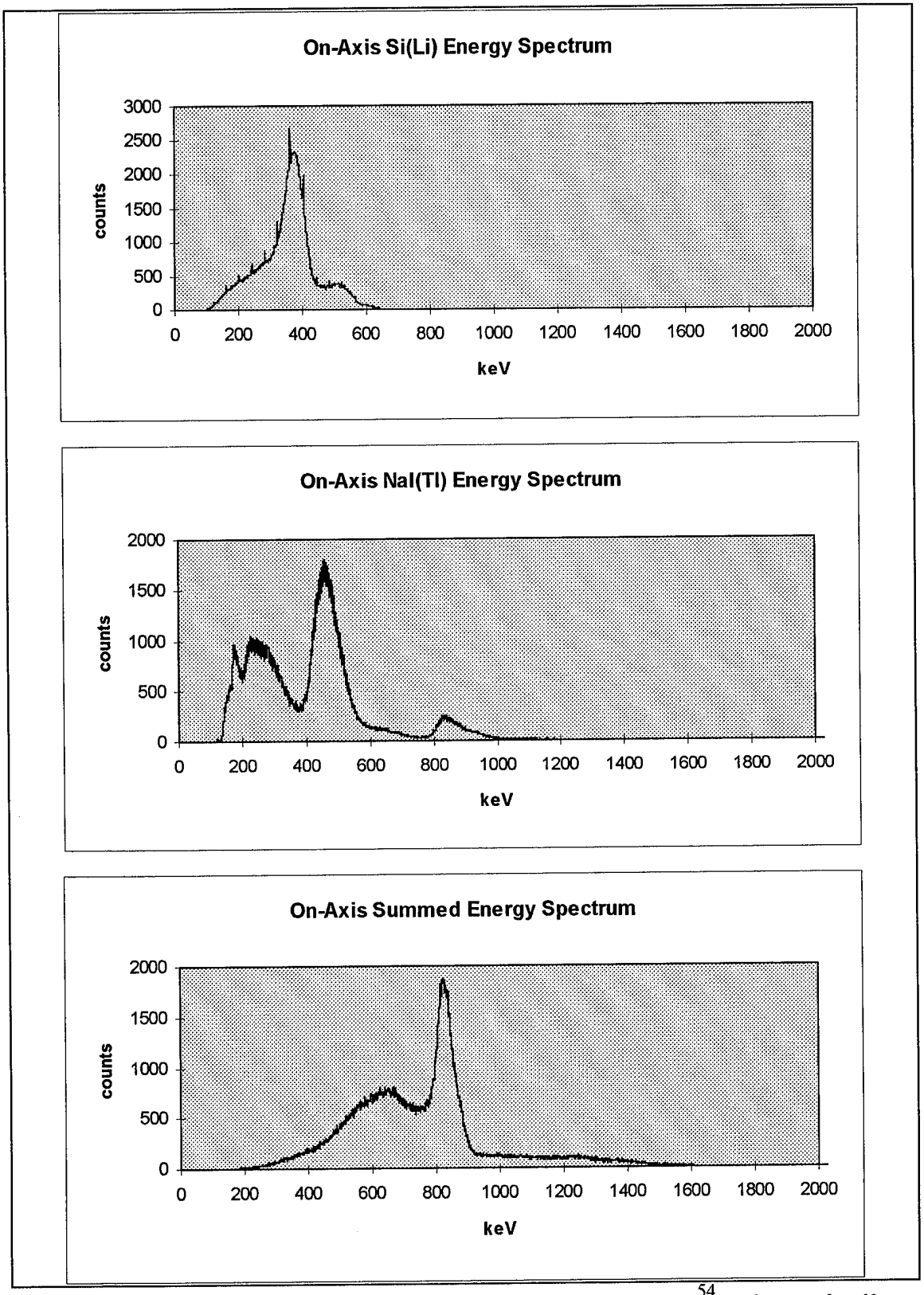

Figure 5-29. Coincident Energy Spectra Collected Collected From On-Axis ^{54}Mn Source. $\theta = 60$ degrees.

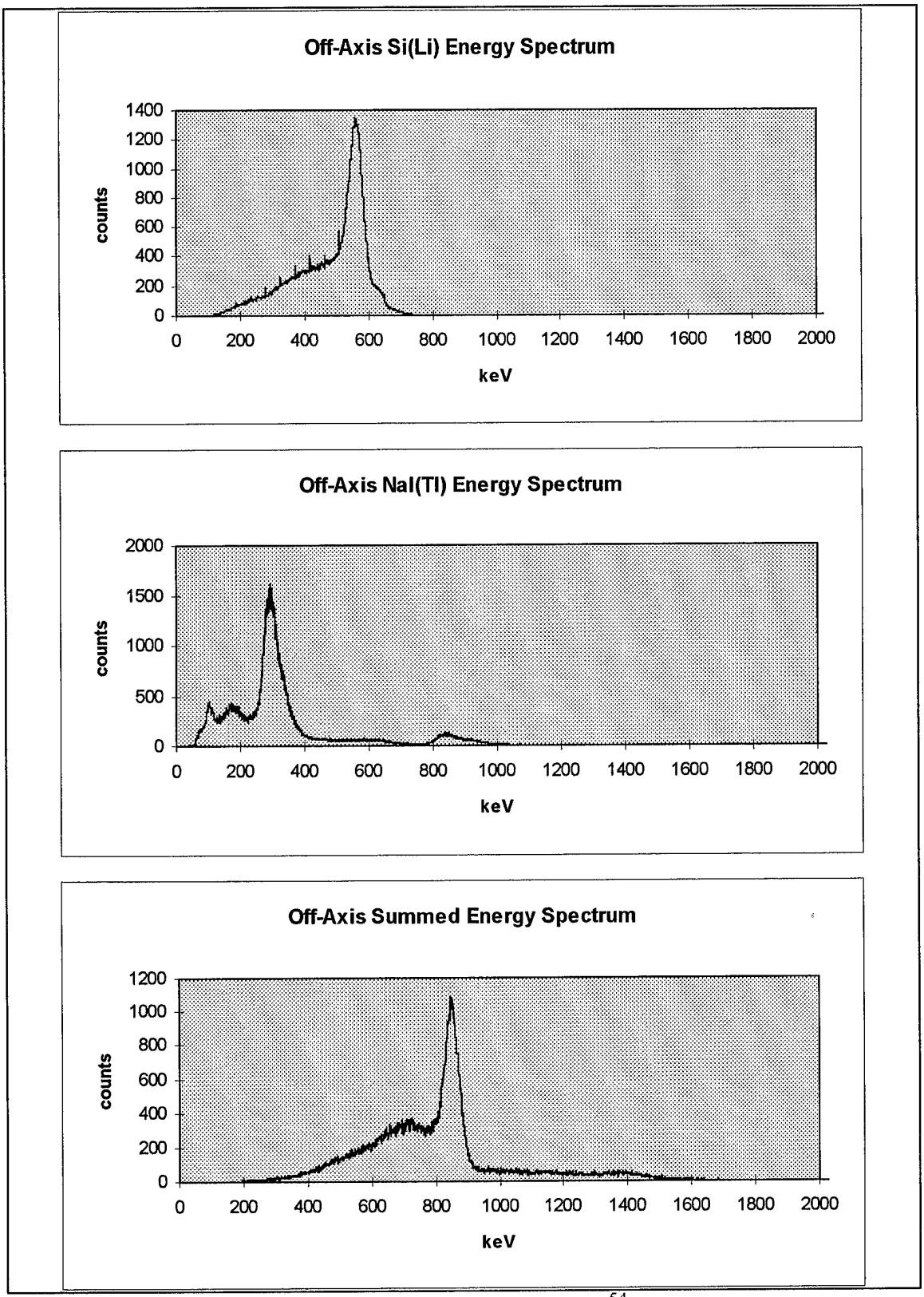

Figure 5-30. Coincident Energy Specta Collected From Off-Axis ^{54}Mn Source. θ = 104 degrees.

VI. DISCUSSION AND CONCLUSIONS

The primary objective of the project was to characterize the angular resolution, efficiency, and energy resolution of the proposed device. The models which were developed formed the basis of the results, so it is important to evaluate the performance of the models. It is informative to examine the factors which limit the angular resolution, and consider ways to improve upon it.

Model Performance

DETECT Simulations. The DETECT Monte-Carlo simulation of the scintillation photon behavior in the position-sensitive detector predicted the light attenuation through the detector element with fidelity adequate for the needs of this study. The results of the DETECT simulations were needed to obtain values of α and P_{pmt}, two parameters which were used to model the position and energy resolution of the NaI(Tl) and hypothetical CsI(Tl) position-sensitive scintillators. Although the Kubelka-Munk attenuation model best fits the output of the DETECT simulations, an exponential attenuation model best transfers the results of the simulations to the actual response of the detector, followed closely by a linear attenuation model. Position was best determined in the NaI(Tl) detector based on exponential attenuation, whereas energy was best determined based on linear attenuation.

Position and Energy Resolution Models. Carter's Equations were used to model the position and energy resolution in the second detector element. Carter's equation for position resolution correctly predicted the measured response of the detector as a function of energy and position of interaction. Carter's equation for energy resolution correctly predicted the variation with position and energy of the measured detector response, although the magnitude of the measured energy resolution was poorer than that predicted by the model. A correction factor was developed to account for the discrepancy.

Efficiency Model. Several of the factors which determine system efficiency do not lend themselves easily to analytical modeling and make accurate efficiency prediction difficult. These factors include the recoil electron penetration of the first detector, the intrinsic peak efficiency ε_{ip2} of the second

detector, and the variation of ε_{ip2} with scattering angle. The measured efficiencies of the two-detector system indicate that the efficiency model is at least accurate within an order of magnitude (see Figure 5-17).

Comparison of Results to Existing Systems

Angular Resolution. The angular resolution of the proposed CsI(Tl)-based system will be approximately four to six degrees for much of the energy range of interest as shown in Figure 5-29. Preliminary results from an all-HPGe Compton camera showed an angular resolutions between 0.3 and 1.1 degrees at 662 keV [McKisson 1994]. The better angular resolution available from the all-HPGe system is a results from the good energy resolution and small dimensions of HPGe detectors, but comes at the expense of efficiency. The efficiency suffers because each detector element is small, has 6 to 12 percent of the efficiency of a 3 inch x 3 inch NaI(Tl) detector and is arranged in a sparse array covering a small range of solid angle. The angular resolution of the proposed system is comparable to that of the HPGe-NaI(Tl) ring Compton camera which has a best resolution of 4.4 degrees at 2750 keV [Martin 1994:237]. In both of the existing systems, the need for liquid nitrogen cooling reduces their portability.

System Energy Resolution. By taking advantage of the outstanding energy resolution of cooled HPGe detectors, the all-HPGe Compton camera provides energy resolutions of 1.8 keV FWHM at 662 keV and 4.0 keV FWHM at 1333 keV, which is far better than the proposed device [McKisson 1994]. The proposed system is not appropriate for particularly demanding spectroscopy requirements where energy peaks may be separated by less than about 50 keV.

Efficiency. The efficiency model predicts an intrinsic efficiency for a full-ring second detector on the order of 10^{-4} at 1000 keV. If an array of ten first detector elements are used as the first position-sensitive detector, then an efficiency on the order of 10^{-3} should be attained. The intrinsic efficiency of the HPGe-NaI(Tl) ring Compton camera at 1000 keV was on the order of 10^{-4} [Martin 1994:135], so the proposed system enjoys roughly an order of magnitude improvement in efficiency.

Factors Which Limit Angular Resolution

The angular uncertainty in the direction of incident radiation is a function of three uncertainties: the uncertainty in the position of interaction which determines the geometric component $\Delta\theta_g$, the uncertainty in measuring the recoil electron energy ΔE_{re} in the first detector, and the uncertainty in measuring the scattered photon energy $\Delta E_{\gamma'}$ in the second detector. The latter two uncertainties contribute to $\Delta\theta_e$, the energy component. Investigating how each uncertainty contributes to the total angular uncertainty reveals important characteristics of the proposed system. Cases 1 and 3 in the CsI(Tl)-based system are considered below, but in general the same conclusions can be applied to the NaI(Tl)-based system.

In case 1 where the incident gamma-ray energy is known, the total angular uncertainty in the CsI(Tl)-based system is a function of the geometric component and the energy resolution in the first detector. Figure 6-1 illustrates how these two components contribute to the total angular uncertainty. At energies above 1 MeV the geometric component dominates the angular uncertainty. At energies below 1 MeV the energy resolution of the second detector becomes a significant factor, and the energy component dominates the total angular uncertainty. Since the gamma-ray energy is determined in the second detector in the CsI(Tl)-based system, the energy resolution of the first detector does not contribute to the total angular uncertainty in case 1.

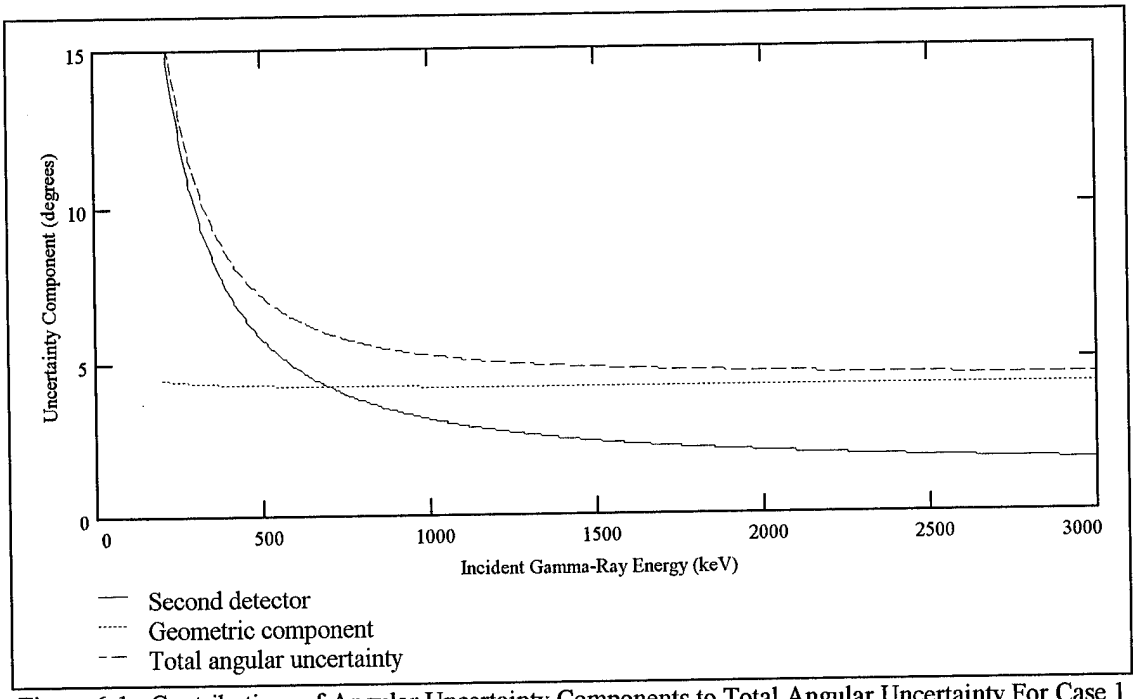

Figure 6-1. Contributions of Angular Uncertainty Components to Total Angular Uncertainty For Case 1 in CsI(Tl)-Based System.

For an unknown gamma-ray energy, case 3 involves summing the energy deposited in both detectors event-by-event so that the energy resolutions of both detectors as well as the geometric component contribute to the total angular uncertainty. Figure 6-2 illustrates how each component contributes to the total angular uncertainty. Again at energies above 1 MeV, the total angular uncertainty is dominated by the geometric component. At energies below 1 MeV, the uncertainty in measuring the recoil electron energy in the first detector becomes significant with respect to the incident gamma-ray energy and therefore introduces significant error in measuring the gamma-ray energy and determining θ. The first detector contribution dominates the total angular uncertainty at energies below 1 MeV and increases rapidly as the incident energy decreases.

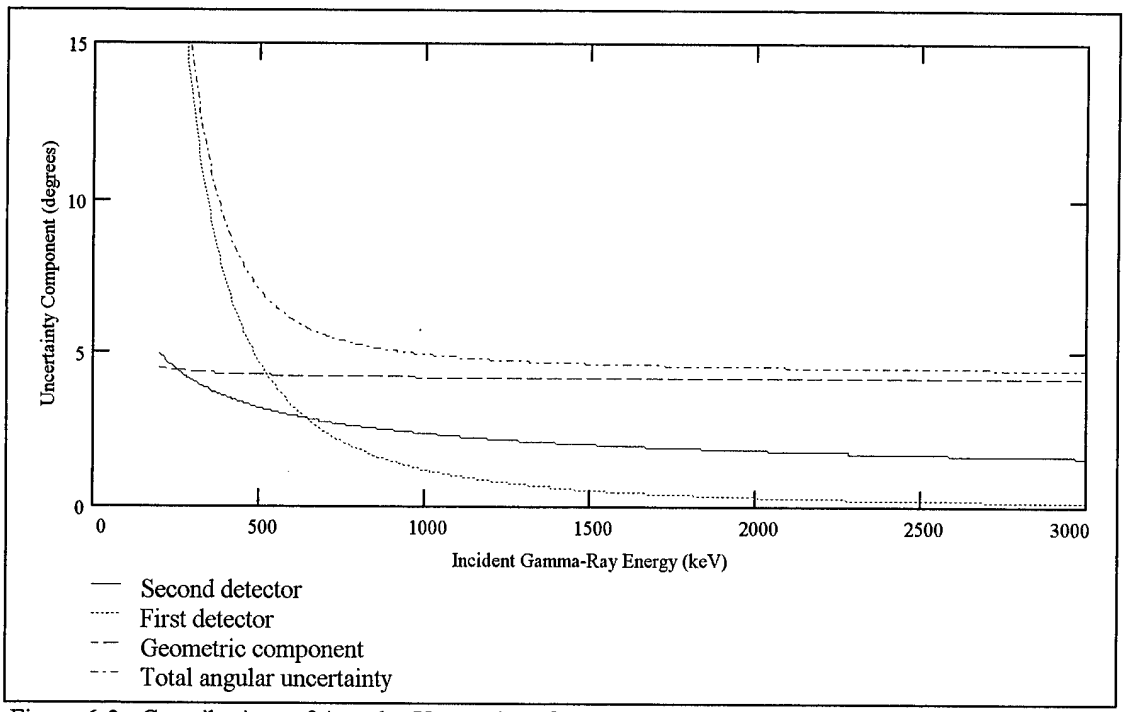

Figure 6-2. Contributions of Angular Uncertainty Components to Total Angular Uncertainty For Case 3 in CsI(Tl)-Based System.

To improve the angular resolution above 1 MeV, the geometric component must be reduced since it dominates at these energies. The magnitude of the geometric component reflects the uncertainty in the positions of interaction in the two detectors. In both the NaI(Tl) and CsI(Tl)-based systems, the positional uncertainty in the y-direction of the second detector dominated the positional uncertainty in the x-direction and the positional uncertainty in the first detector. Recall that the position of interaction in the second detector's y-direction cannot be determined with any more precision than the y-dimension (height) of the crystal and that the uncertainty in the x-direction is the position resolution of the detector. These uncertainties define a resolution element as illustrated in Figure 5-20. The position of interaction in the first detector can be localized to the first detector volume, which is comparatively small. When these uncertainties add in quadrature the y-uncertainty dominates $\Delta\theta_g$. At first glance, reducing the y-dimension of the crystal seems the logical solution to improve the angular resolution above 1 MeV, but the extent to which the height of the crystal should be reduced is limited by the reduction in efficiency and increase in the intensity of contaminating events which would result.

If the y-dimension of the second detector element were reduced, the efficiency of the system would decrease because a narrower range of angles would be available for the scattered photon to strike the second detector. Multiple detector rings could be arranged to counteract this problem. However, when the volume of a detector is reduced, the likelihood of a full-energy photopeak event is reduced. Incident photons are more likely to Compton scatter in the detector and escape without depositing their full energy, thus reducing the peak-to-total ratio in the detector and increasing the intensity of contaminating events. Because CsI(Tl) has a higher photoelectric cross-section than NaI(Tl), the y-dimension of a CsI(Tl) position-sensitive scintillator could be reduced slightly while maintaining efficiency and peak-to-total ratios similar to that of the NaI(Tl)-based Compton camera. However, as demonstrated by Figures 5-29 and 5-30, the number of contaminating events is already substantial for the NaI(Tl)-based system at the mid-range energy of 835 keV, and most contaminating events occur in the second detector. These factors discourage the reduction of the second detector's y-dimension and lead to the conclusion that an angular resolution of about 4 degrees is the best attainable in the proposed system.

Since the second detector's y-dimension dominates the geometric component, we are at liberty to substantially increase the dimensions of the first detector without significantly increasing the geometric component. Increasing the first detector volume by a factor of four (increasing its radius by a factor of 1.44 and its depth by a factor of 2) will have no measurable impact on the angular resolution, assuming that the energy resolution remains the same. This is an important conclusion because, as illustrated by Figure 2-4, the range of recoil electrons exceeds the depth of the detector used in this study at an incident gamma-ray energy of 2.2 MeV. A larger first detector element is therefore necessary to image energies above 2.2 MeV. An advantage would be gained at all energies in increased efficiency and decreased recoil electron penetrations of the first detector elements.

At energies below 1 MeV, the uncertainty in measuring the recoil electron energy, i.e. the first detector energy resolution, begins to dominate the total angular uncertainty for case 3. Recalling that the first detector element energy resolution was dominated by thermal noise from room-temperature operation, the most effective way to improve the angular resolution at these energies is to cryogenically cool the first detector elements. Although a cooling system reduces the portability of a Compton camera,

an optional means of cooling would be a welcome feature to the user who encounters a low-energy (< 1 MeV) field for which the angular resolution requirements are too demanding for room-temperature operation to satisfy. A system could be designed in which cooling can be used only when needed and which would retain maximum portability when operated at room temperature. Energy resolutions of 2 keV are typical for liquid-nitrogen-cooled semiconductor detectors at energies near 1000 keV [Knoll 1989:401]. Figure 6-3 shows what the resulting angular uncertainty components and total angular uncertainty would be if such a cooled first detector were used. The angular resolution at energies below 1 MeV has been significantly improved.

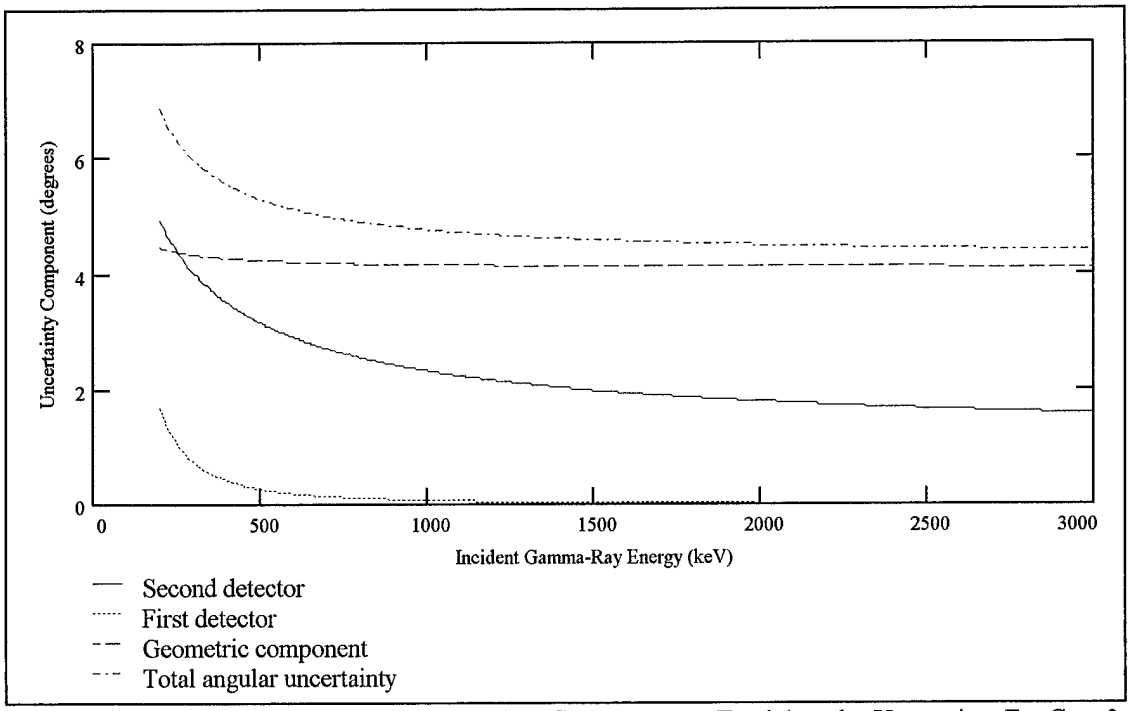

Figure 6-3. Contributions of Angular Uncertainty Components to Total Angular Uncertainty For Case 3 in CsI(Tl)-Based System With Cooled First Detector Elements.

The cooling of the first detector would also have important ramifications in the unknown energy case (case 1) since the angular uncertainty introduced by calculating θ from E_{re} as in Equation 5-18 would now be smaller than the uncertainty introduced by calculating θ from E_{γ}' as in Equation 5-19. Figure 6-4 shows the angular uncertainty components for case 1 with cooled first detector elements. Again the angular resolution has been significantly improved at energies below 1 MeV.

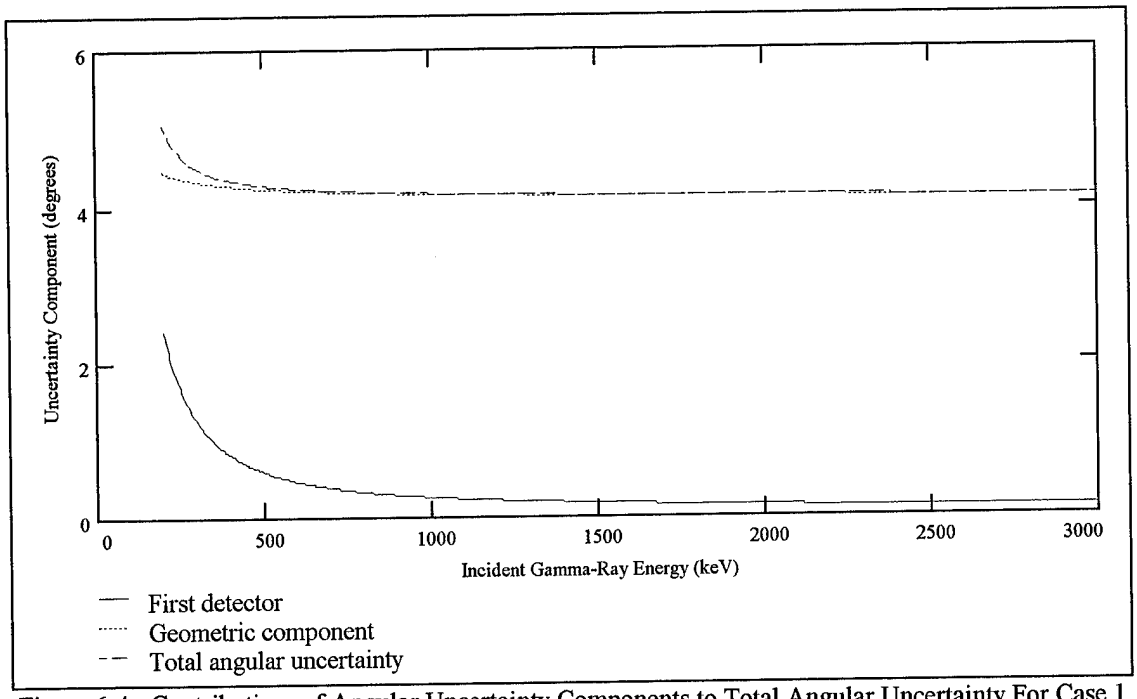

Figure 6-4. Contributions of Angular Uncertainty Components to Total Angular Uncertainty For Case 1 in CsI(Tl)-Based System With Cooled First Detector Elements.

Naturally the improved energy resolution in the first detector which results from cryogenic cooling will also improve the spectroscopic characteristics of the system. Figure 6-5 demonstrates that system energy resolution is improved by 15 to 30 keV FWHM when the cooled first detector elements are used. Closely-spaced Energy peaks which are not resolvable at room-temperature operation may be resolved when the first detector is cooled, aiding in isotope identification. If the system were designed for optional of cryogenic cooling, it would be incumbent upon the user to decide if the demands of the application justify the added burden of the cooling system.

Clearly CsI(Tl) is a superior choice for the scintillation material. It improves efficiency, angular resolution, energy resolution, and power consumption over a NaI(Tl)-based system. It is worthwhile to note that the superior position resolution of the hypothetical CsI(Tl) detector does not contribute significantly to the improvement in angular resolution because the resolution element is still dominated by the y-uncertainty. The CsI(Tl) superior energy resolution is the quality which gives it an advantage in angular resolution. In other words, if a tradeoff between energy resolution and position resolution is to be made in the design of a second detector element, it should be made in favor of superior energy resolution.

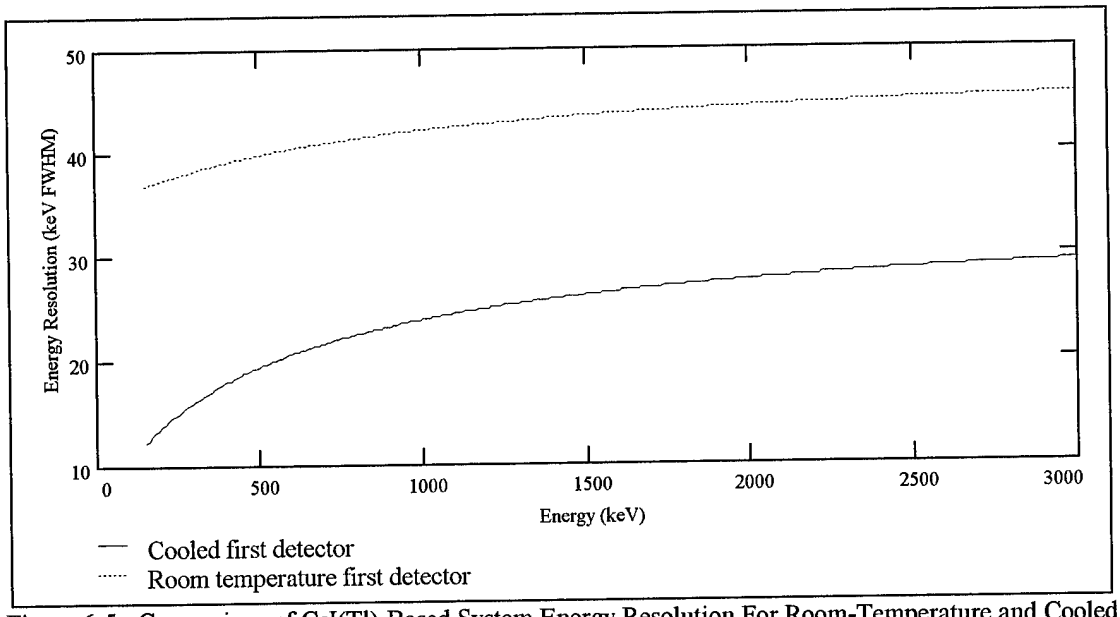

Figure 6-5. Comparison of CsI(Tl)-Based System Energy Resolution For Room-Temperature and Cooled First Detector Elements.

Recommendations For Future Work

The design of a Compton camera such as the one studied here is a complex optimization problem. Many parameters can be optimized to give the best combination of efficiency, angular resolution, and energy resolution. Some of these parameters are, for instance, the central scattering angle, the dimensions and optical properties (such as light attenuation) of the second detector, the incident energy, the type and dimension of first detector, etc. An integrated computer program in which the designer could vary system parameters and investigate the results within one program would be beneficial. The models developed here could form the basis of such a program, however a reliable method for predicting the intensity of contaminating events is needed.

A problem which was encountered in this project was the lack of well-defined specifications regarding the requirements for a field-deployable gamma-ray imaging system for the counterproliferation role. In order to determine if the proposed device is suitable for such a role, criteria are needed which specify the required angular resolution, energy resolution, and efficiency. A study is needed which will define these criteria. The suitability of the proposed device should be evaluated before a more full-scale device is built.

Bibliography

[CAEN 1993] C.A.E.N., S.p.A., Technical Information Manual - Mod. C 420 8 Channel Peak-Sensing 12 Bit ADC, October 1993.

[Carter 1982] J.N. Carter, P. Charalambous, A.J. Dean, J.B. Stephen, et al, "A Position Sensitive Detector For a Gamma-Ray Imaging Telescope., Nuclear Instruments and Methods, Vol 196, pp. 477-482, September 1982.

[Dean 1987] A.J. Dean, G. Graham, C.J. Hopkins, D. Ramsden, and Meng Lei, "A Position Sensitive Gamma-Ray Detector Which Employs Photodiode and CsI(Tl) Crystals," IEEE Trans. Nucl. Sci, NS-34, no. 4, August 1987.

[DETECT] "The DETECT Program for Modelling Optical Properties of Scintillators", (Program Manual)

[Hamamatsu 1990] Hamamatsu Photonics K.K., Photomultiplier Tubes, (catalog), October 1990

[Knoll 1989] G.F. Knoll, Radiation Detection and Measurement (Second Edition). New York: John Wiley & Sons, 1989.

[Kortum 1969] G. Kortum, Reflectance Spectroscopy Principles, Methods, and Applications. Berlin: Springer-Verlag, 1989.

[Lide 1992] David R. Lide, Editor-in-Chief, CRC Handbook of Chemistry and Physics. Boca Raton, FL: CRC Press, Inc., 1992.

[Markakis 1985] J. Markakis, C. Ortale, and W. Schnepple, "Mercuric Iodide Photodetectors For Scintillation Spectroscopy," IEEE Transactions on Nuclear Science, Vol NS-32, no. 1, pp 559-562 February 1985.

[Markakis 1988] J.M. Markakis, "Mercuric Iodide Photodetector - Cesium Iodide Scintillator Gamma-Ray Spectrometers," IEEE Trans. Nucl. Sci., NS-35, no. 1, pp. 356-359, February 1988.

[Martin 1994] J.B. Martin, A Compton Scatter Camera for Spectral Imaging of .5 to 3.0 MeV Gamma Rays. Ph.D. dissertation. The University of Michigan, Ann Arbor MI, 1994.

[McKisson 1994] J.E. McKisson and P.S. Haskins, "Demonstartion of Three-Dimensional Imaging with a Germanium Compton Camera," IEEE Trans. Nucl. Sci., NS-41, no. 4, pp. 1221-1224, August 1994.

[Pages 1972] L. Pages, E. Bertel, H. Joffre, L. Sklavenitis, Energy Loss, Range, and Brehmsstrahlung Yield For 10 KeV to 100 MeV Electrons in Various Elements and Chemical Compounds. New York: Academic Press, Inc., 1972.

[Plein 1993] Plein & Baus, GmbH, Multi - The Data Acquisition Program for IBM-PC/CAMAC Based Multi Parameter Experiments (software manual), April 1993.

[Plein 1994] Plein & Baus, GmbH, Camac Crate Controller CC16 User Manual, November 1994.

[Valentine 1993] Valentine, John D. Temperature Dependence of CsI(Tl) Gamma-Ray Excited Scintillation Characteristics. PhD dissertation. The University of Michigan, Ann Arbor, MI, 1993.

[Wang 1994] Y.J. Wang, J.S. Iwanczyk, and B.E. Pratt, "New Concepts for Scintillator/HgI_2 Gamma-Ray Spectroscopy," IEEE Trans Nucl Sci, NS-41, no. 4, pp 910-914, August 1994.

Appendix A: DETECT Input File

The following file is an example of an input file used in the DETECT simulation of the position-sensitive scintillator. The input file defines the geometry and optical properties of the components, and defines the number and initial position of scintillation photons to simulate.

```
INIT

DMAT1,1.85N
DMAT2,1.5N
DMAT3,1.0N

DFIN1,PAINT,.8245RC
DFIN2,POLISH
DFIN3,DETECT
DFIN4,POLISH
DFIN5,GROUND

DPLN1,1.9Z
DPLN21,1.91Z
DPLN2,0Y
DPLN22,-.01Y
DPLN3,0Z
DPLN23,-.01Z
DPLN4,5.08Y
DPLN24,5.09Y
DPLN5,30.0X
DPLN6,30.9525X
DPLN7,0X
DPLN8,-.9525X

COMP1,MAT1
SURF,PLN1,ZS,FIN5,CONN4
SURF,PLN2,YL,FIN5,CONN5
SURF,PLN3,ZL,FIN5,CONN6
SURF,PLN4,YS,FIN5,CONN7
SURF,PLN7,XL,FIN4,CONN3
SURF,PLN5,XS,FIN4,CONN2

COMP2,MAT2
SURF,PLN1,ZS,FIN2,CONN24
SURF,PLN2,YL,FIN2,CONN25
SURF,PLN3,ZL,FIN2,CONN26
SURF,PLN4,YS,FIN2,CONN27
SURF,PLN5,XL,FIN4,CONN1
SURF,PLN6,XS,FIN3

COMP3,MAT2
SURF,PLN1,ZS,FIN2,CONN34
SURF,PLN2,YL,FIN2,CONN35
SURF,PLN3,ZL,FIN2,CONN36
SURF,PLN4,YS,FIN2,CONN37
SURF,PLN8,XL,FIN4
```

SURF,PLN7,XS,FIN4,CONN1

COMP4,MAT3
SURF,PLN1,ZL,FIN5,CONN1
SURF,PLN21,ZS,FIN1
SURF,PLN7,XL,CONN34
SURF,PLN5,XS,CONN24
SURF,PLN2,YL,CONN45
SURF,PLN4,YS,CONN47

COMP24,MAT3
SURF,PLN21,ZS,FIN1
SURF,PLN1,ZL,FIN2,CONN2
SURF,PLN5,XL,CONN4
SURF,PLN6,XS,FIN3
SURF,PLN2,YL,CONN84
SURF,PLN4,YS,CONN87

COMP34,MAT3
SURF,PLN1,ZL,FIN2,CONN3
SURF,PLN21,ZS,FIN1
SURF,PLN7,XS,CONN4
SURF,PLN8,XL,FIN4
SURF,PLN4,YS,CONN77
SURF,PLN2,YL,CONN74

COMP5,MAT3
SURF,PLN1,ZS,CONN45
SURF,PLN3,ZL,CONN56
SURF,PLN7,XL,CONN35
SURF,PLN5,XS,CONN25
SURF,PLN22,YL,FIN1
SURF,PLN2,YS,FIN5,CONN1

COMP25,MAT3
SURF,PLN1,ZS,CONN84
SURF,PLN3,ZL,CONN85
SURF,PLN5,XL,CONN5
SURF,PLN6,XS,FIN3
SURF,PLN22,YL,FIN1
SURF,PLN2,YS,FIN2,CONN2

COMP35,MAT3
SURF,PLN1,ZS,CONN74
SURF,PLN3,ZL,CONN75
SURF,PLN8,XL,FIN4
SURF,PLN7,XS,CONN5
SURF,PLN22,YL,FIN1
SURF,PLN2,YS,FIN2,CONN3

COMP6,MAT3
SURF,PLN3,ZS,FIN5,CONN1
SURF,PLN23,ZL,FIN1
SURF,PLN7,XL,CONN36

SURF,PLN5,XS,CONN26
SURF,PLN2,YL,CONN56
SURF,PLN4,YS,CONN67

COMP26,MAT3
SURF,PLN3,ZS,FIN2,CONN2
SURF,PLN23,ZL,FIN1
SURF,PLN5,XL,CONN6
SURF,PLN6,XS,FIN3
SURF,PLN2,YL,CONN85
SURF,PLN4,YS,CONN86

COMP36,MAT3
SURF,PLN3,ZS,FIN2,CONN3
SURF,PLN23,ZL,FIN1
SURF,PLN7,XS,CONN6
SURF,PLN8,XL,FIN4
SURF,PLN2,YL,CONN75
SURF,PLN4,YS,CONN76

COMP7,MAT3
SURF,PLN1,ZS,CONN47
SURF,PLN3,ZL,CONN67
SURF,PLN4,YL,FIN5,CONN1
SURF,PLN24,YS,FIN1
SURF,PLN7,XL,CONN37
SURF,PLN5,XS,CONN27

COMP27,MAT3
SURF,PLN1,ZS,CONN87
SURF,PLN3,ZL,CONN86
SURF,PLN5,XL,CONN7
SURF,PLN6,XS,FIN3
SURF,PLN4,YL,FIN2,CONN2
SURF,PLN24,YS,FIN1

COMP37,MAT3
SURF,PLN1,ZS,CONN77
SURF,PLN3,ZL,CONN76
SURF,PLN8,XL,FIN4
SURF,PLN7,XS,CONN7
SURF,PLN4,YL,FIN2,CONN3
SURF,PLN24,YS,FIN1

COMP45,MAT3
SURF,PLN21,ZS,FIN1
SURF,PLN1,ZL,CONN5
SURF,PLN7,XL,CONN74
SURF,PLN5,XS,CONN84
SURF,PLN22,YL,FIN1
SURF,PLN2,YS,CONN4

COMP84,MAT3
SURF,PLN21,ZS,FIN1

SURF,PLN1,ZL,CONN25
SURF,PLN5,XL,CONN45
SURF,PLN6,XS,FIN3
SURF,PLN22,YL,FIN1
SURF,PLN2,YS,CONN24

COMP74,MAT3
SURF,PLN21,ZS,FIN1
SURF,PLN1,ZL,CONN35
SURF,PLN8,XL,FIN4
SURF,PLN7,XS,CONN45
SURF,PLN22,YL,FIN1
SURF,PLN2,YS,CONN34

COMP56,MAT3
SURF,PLN3,ZS,CONN5
SURF,PLN23,ZL,FIN1
SURF,PLN7,XL,CONN75
SURF,PLN5,XS,CONN85
SURF,PLN22,YL,FIN1
SURF,PLN2,YS,CONN6

COMP85,MAT3
SURF,PLN3,ZS,CONN25
SURF,PLN23,ZL,FIN1
SURF,PLN5,XL,CONN56
SURF,PLN6,XS,FIN3
SURF,PLN22,YL,FIN1
SURF,PLN2,YS,CONN26

COMP75,MAT3
SURF,PLN3,ZS,CONN35
SURF,PLN23,ZL,FIN1
SURF,PLN8,XL,FIN4
SURF,PLN7,XS,CONN56
SURF,PLN22,YL,FIN1
SURF,PLN2,YS,CONN36

COMP67,MAT3
SURF,PLN3,ZS,CONN7
SURF,PLN23,ZL,FIN1
SURF,PLN7,XL,CONN76
SURF,PLN5,XS,CONN86
SURF,PLN4,YL,CONN6
SURF,PLN24,YS,FIN1

COMP86,MAT3
SURF,PLN3,ZS,CONN27
SURF,PLN23,ZL,FIN1
SURF,PLN5,XL,CONN67
SURF,PLN6,XS,FIN3
SURF,PLN4,YL,CONN26
SURF,PLN24,YS,FIN1

```
COMP76,MAT3
SURF,PLN3,ZS,CONN37
SURF,PLN23,ZL,FIN1
SURF,PLN8,XL,FIN4
SURF,PLN7,XS,CONN67
SURF,PLN4,YL,CONN36
SURF,PLN24,YS,FIN1

COMP47,MAT3
SURF,PLN21,ZS,FIN1
SURF,PLN1,ZL,CONN7
SURF,PLN7,XL,CONN77
SURF,PLN5,XS,CONN87
SURF,PLN4,YL,CONN4
SURF,PLN24,YS,FIN1

COMP87,MAT3
SURF,PLN21,ZS,FIN1
SURF,PLN1,ZL,CONN27
SURF,PLN5,XL,CONN47
SURF,PLN6,XS,FIN3
SURF,PLN4,YL,CONN24
SURF,PLN24,YS,FIN1

COMP77,MAT3
SURF,PLN21,ZS,FIN1
SURF,PLN1,ZL,CONN37
SURF,PLN8,XL,FIN4
SURF,PLN7,XS,CONN47
SURF,PLN4,YL,CONN34
SURF,PLN24,YS,FIN1

GEN,MAT1,19.843992XS,20.156008XL,.794ZS,1.106ZL,2.384YS,2.696YL
LIFE4000
HIST,STEP1000,4STEPS
SEED6780
TRACE0
FATES2
RUN31472
END
```

Appendix B: Mathematica Code

The following Mathematica code was used to characterize the width of the collimated radiation beam for the efficiency calculation and the correction to the modeled position resolution.

```
(* COLLIMATION CALCULATION *)

R1=.65;  (* Larger radius (cm) *)
D1=10.16; (* Depth of smaller radius (cm) *)
R2=.3;   (* Smaller radius (cm) *)
D2=5.08;   (* Depth of larger radius (cm) *)
deep=5.08; (* Depth of Detector*)
height=1.90;(* Height of detector *)
dens=11.34; (* density of lead *)

(* energies to be studied and the total attenuation
  coefficients in lead *)

kevlist={511,662,835,898,1275,1836,2500,3000};
mulist={.156,.110,.0848,.0787,.0579,.0475,
      .0435,.0423};

(* define the total pathlength through lead
  as a function of angle theta*)
theta1=ArcTan[R2/D1];
theta2=ArcTan[R2/(D1+D2)];
theta3=ArcTan[R1/D1];
thetamin=theta2;

p2[theta_]:=((D1+D2)/Cos[theta])-(D1/Cos[theta]);
p4[theta_]:=((D1+D2)/Cos[theta])-(R2/Sin[theta]);
p5[theta_]:=((D1+D2)/Cos[theta])-(R1/Sin[theta]);

pathlength[theta_]:=
Which[theta<=thetamin,0.,
    theta>thetamin&&theta<=theta1,p4[theta],
    theta>theta1&&theta<=theta3,p2[theta],
    theta>theta3,p5[theta]];

(* distance from center of beam and angle in terms
  of x and y (halfway through detector) *)
r[x_,y_]:=Sqrt[x^2+y^2];
angle[x_,y_]:=ArcTan[r[x,y]/(D1+D2+(deep/2))];
radmin=Tan[thetamin] (D1+D2+(deep/2));

(* define the brightness in terms of x and y *)
brightness[x_,y_]:=intensity[angle[x,y]];

Do[
kev=Part[kevlist,i];
mu=Part[mulist,i];
Print["Energy = ",kev," keV"];
```

```
(* define I/Io as a function of path length *)
intensity[theta_]:=Exp[-mu dens pathlength[theta]];

(* Plot the beam profile *)
Plot3D[brightness[x,y],{x,-1.5,1.5},
{y,-1.5,1.5},
PlotPoints->75,
PlotLabel->{"Collimation Profile -- ",kev},
AxesLabel->{"x (cm)","y (cm)","I/Io"},
PlotRange->All];

(* Integrate over y at values of x and interpolate
  to get total intensity as a function of x *)
h=.005; (*step size for trapezoid rule *)
trapezoid[x_]:=2 Sum[
   (h/2) (brightness[x,y]+brightness[x,y+h]),
   {y,0,(height/2),h}];
normalize=trapezoid[0.];
inttable=Table[{x,trapezoid[x]/normalize},
          {x,0,10,.02}];
totalint=Interpolation[inttable];

(* plot the total intensity profile *)
Show[
Plot[totalint[x],{x,0.,9.5}],
ListPlot[inttable],PlotRange->All,
AxesLabel->{"cm","I/Io"},
PlotLabel->{"Total Intensity vs. x  ",kev},
GridLines->Automatic];

(* find the fwhm of total intensity function
  for position resolution *)
hwhm=x/.FindRoot[totalint[x]==.5,{x,.1,2.}];
Print["at ",kev," keV, fwhm = ",2 hwhm," cm"];

(* find the mean radius for efficiency calculation *)
h=.005;
meanrad=
  Sum[(h/2) x (brightness[x,0]+brightness[x+h,0]),
  {x,radmin,5,h}]/
  Sum[(h/2) (brightness[x,0]+brightness[x+h,0]),
  {x,radmin,5,h}];
Print ["at ",kev," kev, mean radius = ",meanrad];

,{i,1,Length[kevlist]}]
```

Samples of output are shown if Figures 4-3, 4-4, and 4-5.

Vita

Captain Brian L. Evans was born on 12 May 1969 at Roosevelt Roads Naval Air Station in Puerto Rico. In 1987 he graduated from James W. Robinson High School in Fairfax, Virginia. He entered undergraduate studies at Miami University in Oxford, Ohio, and graduated in May 1991 with a Bachelor of Science degree in Engineering Physics. He received his Air Force commission on 12 May 1991. His first assignment was to the 91st Maintenance Group at Minot Air Force Base, North Dakota where he worked as a Missile Maintenance Officer on the Minuteman III weapon system. In May 1994, he entered the School of Engineering, Air Force Institute of Technology.

REPORT DOCUMENTATION PAGE

Form Approved
OMB No. 0704-0188

1. AGENCY USE ONLY *(Leave blank)*	2. REPORT DATE	3. REPORT TYPE AND DATES COVERED
	Dec 95	Master's Thesis

4. TITLE AND SUBTITLE

A PORTABLE COMPTON GAMMA-RAY CAMERA DESIGN

5. FUNDING NUMBERS

6. AUTHOR(S)

Capt Brian L. Evans, USAF

7. PERFORMING ORGANIZATION NAME(S) AND ADDRESS(ES)

Air Force Institute of Technology
2750 P Street
Wright-Patterson AFB, OH 45433-6583

8. PERFORMING ORGANIZATION REPORT NUMBER

AFIT/GAP/ENP/95D-05

9. SPONSORING / MONITORING AGENCY NAME(S) AND ADDRESS(ES)

N/A

10. SPONSORING / MONITORING AGENCY REPORT NUMBER

N/A

11. SUPPLEMENTARY NOTES

12a. DISTRIBUTION / AVAILABILITY STATEMENT

Approved for public release; distribution unlimited

12b. DISTRIBUTION CODE

13. ABSTRACT *(Maximum 200 words)*

The purpose of this research is to investigate the angular resolution, efficiency, and energy resolution possible from a portable Compton camera gamma-ray imaging system for possible use in the field of nuclear nonproliferation. The proposed device uses room-temperature semiconductor and position-sensitive scintillation detectors. The position and energy resolution (and their energy dependence) of a room-temperature lithium-drifted silicon (Si(Li)) detector and a position-sensitive thallium-doped sodium iodide (NaI(Tl)) scintillation detector are investigated. The position and energy resolution of the position-sensitive scintillation detector is also modeled computationally, and the results compared to measured data. An efficiency model is also presented. The angular resolution, efficiency, and energy resolution of the proposed system are calculated. The same computational methods are then applied to a hypothetical position-sensitive thallium-doped cesium iodide (CsI(Tl)) scintillator. Based on the results, the angular resolution and energy resolution of a system employing this type of position-sensitive detector coupled to the same room-temperature Si(Li) detector is predicted.

14. SUBJECT TERMS

Compton camera, gamma-ray camera, gamma-ray imaging, radiation imaging, counterproliferation, radiation detection, radiation detectors, radiation spectroscopy, gamma-ray spectroscopy, position-sensitive detectors, scintillators

15. NUMBER OF PAGES

115

16. PRICE CODE

17. SECURITY CLASSIFICATION OF REPORT	18. SECURITY CLASSIFICATION OF THIS PAGE	19. SECURITY CLASSIFICATION OF ABSTRACT	20. LIMITATION OF ABSTRACT
Unclassified	Unclassified	Unclassified	UL

GENERAL INSTRUCTIONS FOR COMPLETING SF 298

The Report Documentation Page (RDP) is used in announcing and cataloging reports. It is important that this information be consistent with the rest of the report, particularly the cover and title page. Instructions for filling in each block of the form follow. It is important to ***stay within the lines*** to meet ***optical scanning requirements***.

Block 1. Agency Use Only *(Leave blank)*.

Block 2. Report Date. Full publication date including day, month, and year, if available (e.g. 1 Jan 88). Must cite at least the year.

Block 3. Type of Report and Dates Covered. State whether report is interim, final, etc. If applicable, enter inclusive report dates (e.g. 10 Jun 87 - 30 Jun 88).

Block 4. Title and Subtitle. A title is taken from the part of the report that provides the most meaningful and complete information. When a report is prepared in more than one volume, repeat the primary title, add volume number, and include subtitle for the specific volume. On classified documents enter the title classification in parentheses.

Block 5. Funding Numbers. To include contract and grant numbers; may include program element number(s), project number(s), task number(s), and work unit number(s). Use the following labels:

C	- Contract	**PR**	- Project
G	- Grant	**TA**	- Task
PE	- Program Element	**WU**	- Work Unit Accession No.

Block 6. Author(s). Name(s) of person(s) responsible for writing the report, performing the research, or credited with the content of the report. If editor or compiler, this should follow the name(s).

Block 7. Performing Organization Name(s) and Address(es). Self-explanatory.

Block 8. Performing Organization Report Number. Enter the unique alphanumeric report number(s) assigned by the organization performing the report.

Block 9. Sponsoring/Monitoring Agency Name(s) and Address(es). Self-explanatory.

Block 10. Sponsoring/Monitoring Agency Report Number. *(If known)*

Block 11. Supplementary Notes. Enter information not included elsewhere such as: Prepared in cooperation with...; Trans. of...; To be published in.... When a report is revised, include a statement whether the new report supersedes or supplements the older report.

Block 12a. Distribution/Availability Statement. Denotes public availability or limitations. Cite any availability to the public. Enter additional limitations or special markings in all capitals (e.g. NOFORN, REL, ITAR).

- **DOD** - See DoDD 5230.24, "Distribution Statements on Technical Documents."
- **DOE** - See authorities.
- **NASA** - See Handbook NHB 2200.2.
- **NTIS** - Leave blank.

Block 12b. Distribution Code.

- **DOD** - Leave blank.
- **DOE** - Enter DOE distribution categories from the Standard Distribution for Unclassified Scientific and Technical Reports.
- **NASA** - Leave blank.
- **NTIS** - Leave blank.

Block 13. Abstract. Include a brief *(Maximum 200 words)* factual summary of the most significant information contained in the report.

Block 14. Subject Terms. Keywords or phrases identifying major subjects in the report.

Block 15. Number of Pages. Enter the total number of pages.

Block 16. Price Code. Enter appropriate price code *(NTIS only)*.

Blocks 17. - 19. Security Classifications. Self-explanatory. Enter U.S. Security Classification in accordance with U.S. Security Regulations (i.e., UNCLASSIFIED). If form contains classified information, stamp classification on the top and bottom of the page.

Block 20. Limitation of Abstract. This block must be completed to assign a limitation to the abstract. Enter either UL (unlimited) or SAR (same as report). An entry in this block is necessary if the abstract is to be limited. If blank, the abstract is assumed to be unlimited.